

2-22-2010

Synthesis and Analysis of the Quantum Dot Core and Surface Structures Probed By Solid State Nuclear Magnetic Resonance

Derek Dean Lovingood
Florida State University

Follow this and additional works at: <http://diginole.lib.fsu.edu/etd>

Recommended Citation

Lovingood, Derek Dean, "Synthesis and Analysis of the Quantum Dot Core and Surface Structures Probed By Solid State Nuclear Magnetic Resonance" (2010). *Electronic Theses, Treatises and Dissertations*. Paper 1031.

This Dissertation - Open Access is brought to you for free and open access by the The Graduate School at DigiNole Commons. It has been accepted for inclusion in Electronic Theses, Treatises and Dissertations by an authorized administrator of DigiNole Commons. For more information, please contact lib-ir@fsu.edu.

THE FLORIDA STATE UNIVERSITY
COLLEGE OF ARTS AND SCIENCE

SYNTHESIS AND ANALYSIS OF THE QUANTUM DOT CORE AND
SURFACE STRUCTURES PROBED BY SOLID STATE NUCLEAR
MAGNETIC RESONANCE

By

DEREK DEAN LOVINGOOD

A Dissertation submitted to the
Department of Chemistry and Biochemistry
in partial fulfillment of the
requirements for the degree of
Doctor of Philosophy

Degree Awarded:
Spring Semester, 2010

Copyright © 2009
Derek Dean Lovingood
All Rights Reserve

The members of the committee approve the dissertation of Derek Dean Lovingood defended on February 22, 2010.

Geoffrey F. Strouse
Professor Directing Dissertation

Peng Xiong
University Representative

Albert E. Stiegman
Committee Member

Gregory B. Dudley
Committee Member

Approved:

Joseph B. Schlenoff, Chair, Department of Chemistry and Biochemistry

Joseph Travis, Dean, College of Arts and Sciences

The Graduate School has verified and approved the above-named committee members.

*I wish to give my love and thanks to my loving, wonderful, caring wife,
parents, grandparents, family and friends for all the support and love I
received throughout the years.*

TABLE OF CONTENTS

List of Tables	iv
List of Figures	v
Abstract	x
1. Introduction	1
1.1 Background Information	1
1.2 Improving synthetic methods	5
1.3 Understanding growth of cluster grown nanomaterials	7
1.4 Solid State NMR – A tool for analysis	8
1.5 Size dependent reconstruction affects on QDs	9
1.6 Summary of chapters	11
2. Microwave induced in-situ active etching of growing InP nanocrystals	12
2.1 Introduction	12
2.2 Experimental	14
2.3 Results / Discussion	16
2.4 Conclusions	21
3. Composition control and localization of S ²⁻ in CdSSe quantum dots grown from Li ₄ [Cd ₁₀ Se ₄ (SPh) ₁₆]	22
3.1 Introduction	22
3.2 Experimental	24
3.2.1 Chemicals	24
3.2.2 Instrumentation	24
3.2.3 Synthesis of CdSSe QDs from Li ₄ [Cd ₁₀ Se ₄ (SPh) ₁₆]	26
3.2.4 Synthesis of CdSe QDs from Li ₄ [Cd ₁₀ Se ₄ (SePh) ₁₆]	26
3.2.5 Microwave synthesis of CdSe from Cd stearate (CdSA)	26
3.2.6 Homogeneous acid etching of CdSSe QDs	27
3.3 Results / Discussion	27
3.3.1 Elemental distribution in the as prepared CdSSe	29
3.3.2 Nature of the CdSSe alloy	36
3.3.3 Qualitative model of the QD	38

3.4 Conclusions	43
4. Size and site dependent reconstruction in CdSe QDs Evidenced by $^{77}\text{Se}\{^1\text{H}\}$ CP-MAS NMR Spectroscopy	46
4.1 Introduction	46
4.2 Experimental	49
4.2.1 Chemicals	49
4.2.2 Synthesis of Cd ^{77}Se QDs from cadmium stearate (CdSA)	49
4.2.3 Synthesis of Cd ^{77}Se QDs from Li $_4$ [Cd $_{10}^{77}\text{Se}_4(\text{SePh})_{16}$].....	49
4.2.4 Solid State Nuclear Magnetic Resonance.....	50
4.2.5 Instrumentation	52
4.3 Results / Discussion.....	53
4.3.1 Analysis of passivating layer, surface and core	54
4.3.2 Site dependent CP buildup curves.....	62
4.3.3 Spin Diffusion and anticipated size effects from spin diffusion	67
4.3.4 T $_2$ spin – relaxation dynamics	70
4.3.5 Changes in bonding.....	71
4.4 Conclusions	77
References	78
Biographical sketch.....	89

LIST OF TABLES

2.1 List of Ionic fluorinated and non-fluorinated additives used for in-situ growth of InP Quantum Dots.	15
3.1 Experimental results for S ²⁻ /Se ²⁻ composition, QD diameter by Scherrer broadening of <110> pXRD reflection, and exciton absorption (1s _e -1s _h). * is the %[Se]/([Se]+[S]) measured by XRF while ** is the %[Se] calculated by the effective mass approximation. Bracketed numbers are diameters verified by HRTEM. Highlighted samples are depicted in Figure 3.2. Reactions marked by † are synthesized via cadmium stearate microwave synthesis.	31
4.1 Summary of Data.	56
4.2 Time Constants for Cd ⁷⁷ Se QDs (<i>The --- indicate the T*_{1pH} for the core signals are too long to be measured in the experimental time frame</i>).	63

LIST OF FIGURES

- 1.1 Representation of a binary QD. Yellow spheres would represent the positive charged species (Cd or In) and purple spheres would represent the negative charged species (Se or P). 2
- 1.2 A) Absorbance spectra of three different sized CdSe QDs showing size confinement. As the diameter of the QDs is changed from small to large (left to right) the color of light the QD emits changes. B) The color change is illustrated in the picture where solutions of three different sized QDs are illuminated by UV radiation. The smallest QD (~2 nm) emits blue, where the midsized (~3.5 nm) emits green and the largest (5.5 nm) emits red. 3
- 1.3 Transmission electron microscopy of Cadmium selenide quantum dots. The measured dots are approximately 8 nm in diameter. 5
- 1.4 CEM Discover microwave reactor used to synthesize quantum dots. Unlike residential microwaves, these microwaves are especially built for the rigors of laboratory use. 6
- 1.5 Illustration of the single source precursor, $\text{Li}_4[\text{Cd}_{10}\text{Se}_4(\text{SPh})_{16}]$ showing the debated products that could be synthesized. QD 1 illustrates a core – shell QD where the core is CdSe and the shell is CdS. QD 2 illustrates an alloy where the QD is CdSse throughout. 7
- 1.6 Illustration of the different layers (passivation, surface, and core) within in a quantum dot that can be measured by Solid State NMR. 9
- 1.7 Solid state NMR pulse sequences A) spin echo B) cross polarization magic angle spinning (CP-MAS) used to measure QD. Spin echo used to measure the whole QD while CP-MAS can be used to measure specific sites within the QD. 10
- 2.1 A) TEM of InP grown with *hmim* BF_4 B) Optical image comparing the solution of InP nanocrystals (hexane) for materials grown with and without *hmim* BF_4 (1:10 mole ratio). The lower half of the image is under UV irradiation C) Comparison of Abs and PL of InP grown with *hmim* BF_4 . Concentrations of the In^{3+} precursor to the IL used are 1:0.1 (black), 1:1 (red), and 1:10 (blue). 16
- 2.2 A) pXRD InP grown with *bmpy* BF_4 B) InP grown with *hmim* BF_4 17

2.3	¹⁹ F MAS of InP grown with <i>bmpy</i> BF ₄ . 2.5 mm rotor and a spinning speed of 22 kHz.	17
2.4	Concentration dependent PL comparison of InP grown from <i>bmpy</i> BF ₄ . 1:0.1 (red), 1:1 (black), 1:10 (blue).	18
2.5	PL QY for a series of In ³⁺ IL mole ratios of InP grown with <i>hmim</i> BF ₄ (solid) and InP grown with <i>bmpy</i> BF ₄ (dash).	19
2.6	Comparison of PL properties for InP grown with a 1:1 mole ratio of <i>hmim</i> PF ₆ (blue), <i>hmim</i> BF ₄ (red), and <i>hmim</i> Cl (black).	20
3.1	Possible composition scenarios for a CdSSeQD grown the cluster, Li ₄ [Cd ₁₀ Se ₄ (SPh) ₁₆].	23
3.2	A) TEM image of 5.7 nm CdSSe QDs with a S ²⁻ :Se ²⁻ ratio of 66:34 by XRF. B) HRTEM images of the same sample with visible lattice fringes. C) Absorption spectra of ~2.4 nm CdSe, CdSSe, and CdS QDs. CdSSe QD S ²⁻ :Se ²⁻ is 36:64 by XRF. D) pXRD spectra of ~2.4 QD samples.	29
3.3	Sample XRF spectra for CdSSe nanocrystals.	30
3.4	Solid state ¹³ C CP-MAS of A) Li ₄ [Cd ₁₀ Se ₄ (SPh) ₁₆] B) 2.1 nm CdSSe C) 2.8 nm CdSSe D) 3.2 nm CdSSe E) 3.6 nm CdSSe F) 4.1 nm CdSSe G) 5.5 CdSSe H) 3.1 nm CdSe grown from CdSA synthesis I) 3.1 nm Cd nm CdSe (CdSA grown) capped with thiophenol J) Tri-octylphosphine oxide K) Stearic Acid.	32
3.5	Number of ligands bound to CdSse QDs plotted vs. QD diameter. Percent of ligands were determined semi-quantitatively by ¹³ C CP-MAS NMR.	34
3.6	¹³ C CP-MAS build up curve on 3.6nm CdSSe. Individual peaks were fit to 4 aromatic and 3 aliphatic signatures. Each individual build up curve was normalized for ease of viewing. All profiles have similar build up except peak 1 (methyl carbon on TOPO) and peak 4 (para carbon on SPh ⁻). Contact times used were 0.5, 1.0, 1.6, 2.0, 2.5, 5.0 ms.	35
3.7	Five separate CdSSe QD reactions grown from Li ₄ [Cd ₁₀ Se ₄ (SPh) ₁₆]. Sizes measured by pXRD Scherrer-Debye analysis and calibrated by HRTEM. Dashed lines are theoretical effective mass approximation of the indicated concentrations of S:Se. Squares are pure CdSe QD samples. Circles are pure CdS QD samples from Ref. 43.	37

3.8 A) CdSSe concentrations calculated by the effective mass approximation plotted against QD size B) CdSSe concentrations calculated by XRF plotted against QD size.	40
3.9 Absorbance profile of growing CdSSe from $\text{Li}_4[\text{Cd}_{10}\text{Se}_4(\text{SPh})_{16}]$. Above ~550nm further growth is possible by growth by decomposition of SPh^- surface ligands leading to lose of first exciton and size distribution.	41
3.10 The %Se (and %S) from XRF analysis from a 3.26 nm CdSSe QD taking during growth (circles) and then subsequent acid etching (squares) by $\text{H}_3\text{PO}_4/\text{HCl}$ (50% v:v). The shaded area represents removal of ~0.4 nm, approximately one lattice plane.	42
3.11 A) Sulfur incorporation vs. QD size. Line 1 depicts growth of a uniform 60S/40Se alloy. Line 2 depicts growth of a 2 nm pure CdSe core with 70S/30Se (solid) 60S/40Se (dashed). Line 3 depicts growth of a 2.25 nm pure CdSe core with 70S/30Se (solid) 60S/40Se (dashed). Other points are experimental growth reactions determined by XRF. B) Model of CdSSe QD, showing crystal structure of a CdSSe QD with organic ligands passivating the surface. CdSSe QD cross-section is cut on the <110>. Model depicts pure CdSe nucleus with CdSSe alloy.	43
4.1 Pulse sequence used for saturation recovery – CPMG experiments. .	51
4.2 Overlay of ^{77}Se CPMG (black) and spin echo (red) showing consistency between two experiments. A) 3.1 nm CdSe, B) 6.9 nm CdSe.	52
4.3 A) Drawing of a 4 nm, truncated wurtzite CdSe QD highlighting the distinctive regions within the QD representing the surface ligation layer (dark blue), near surface layers (light blue) and core layers (white). B) Ligand passivation layer on the <101> plane of a CdSe QD. C and D) Possible reconstruction models where lattice reconstruction induced by surface ligation is C) weakly or D) strongly damped by the within the lattice planes.	54
4.4 Characterization data for CdSe QDs I) 2.95 nm, II) 3.1 nm, III) 4.5 nm, IV) 6.1 nm, and V) 6.9 nm. A) UV-Vis, B) pXRD, and C) TEM.	55

- 4.5 $^{77}\text{Se}\{^1\text{H}\}$ CP-MAS NMR at 4 ms, 12 ms, and 40 ms contact times for Cd^{77}Se QDs. A) 2.9nm (black), B) 3.1nm (light blue), C) 4.3nm (red), D) 6.1nm (green), and E) 6.9nm (dark blue). Fits are assigned as following: Peak 1 (slashed) core ^{77}Se sites; Peak 2 (dotted) near-surface and surface ^{77}Se sites; and Peak 3 (solid) surface ^{77}Se site bound to a TOP ligand. The peak labeled with * identifies the NMR resonance associated with a surface bound TOP through a ^{77}Se on the QD surface. The overall fit of the deconvoluted spectra has been added to each spectrum. 57
- 4.6 A) Spin echo (i-v) and direct pulse (vi) NMR of i) 2.9nm (black), ii) 3.1nm (light blue), iii) 4.3nm (red), iv) 6.1nm (green), v) 6.9nm (dark blue), and vi) Bulk CdSe (orange) B) Size dependent changes in the composition of surface and core assuming T_1 and T_2 are similar for the regions. Circles represent core signal and squares represent surface signals. The hour glass represents the smallest QD grown from cluster. 58
- 4.7 $^{77}\text{Se}\{^1\text{H}\}$ CP-MAS build up curves for A) 3.1nm, B) 4.3nm, C) 6.1nm, E) 6.9nm Cd^{77}Se QDs. The dark blue line represents the intensity of the core (peak 1) ^{77}Se sites, the light blue line represents surface (peak 2) ^{77}Se sites, and the green line represents the ligation layer (peak 3) for ^{77}Se bound to TOP. Contact times used to generate build up curve are: 1, 2, 4, 8, 10, 12, 15, 22, and 40 ms. 61
- 4.8 ^{31}P Direct pulse MAS NMR on A) 2.9 nm, B) 3.1 nm, C) 4.3 nm D) 6.1 nm, E) 6.9 nm, F) TOP-Se. 64
- 4.9 ^1H Spin Lock Experiment at a spinning speed of 24kHz. The higher spinning speeds allows for the multiple ^1H features to be observed. . 65
- 4.10 T_{HSe}^* for surface (red), core (blue), and total (black) ^{77}Se vs. QD diameter. Solid curves are best fit lines. 66
- 4.11 Size dependent A) T_1 and B) T_2 data for Cd^{77}Se : 3.1nm = light blue, 4.3nm = red, 6.1nm = green, 6.9nm = dark blue. The data is fit to a single exponential function for T_1 and bi-exponential function for T_2 . 70
- 4.12 Ramsey plot of chemical shift (ppm) and absorbance with respect to inverse band gap energy (1/eV) for Cd^{77}Se QD samples (2.9nm (black), 3.1nm (light blue), 4.3nm (red), 6.1nm (green), 6.9nm (dark blue)). Pink hour glass represents bulk CdSe within all three plots. A) Represents core ^{77}Se sites B) Represents near-surface and surface ^{77}Se sites C) Represent surface ^{77}Se sites bound to TOP. Open circles correlate to CP-MAS assignments and open squares correlate to spin echo assignments. 71

4.13 Spin Echo and CP-MAS (contact time = 12 ms) ^{77}Se NMR data illustrating the change in chemical shift vs. QD size. A) Spin Echo core, B) Spin Echo surface, C) CP-MAS core, and D) CP-MAS surface sites. Cd^{77}Se QD samples: (2.9nm (black), 3.1nm (light blue), 4.3nm (red), 6.1nm (green), 6.9nm (dark blue)).

..... 73

ABSTRACT

This dissertation outlines how the optical properties of InP quantum dots were improved by microwave synthetic techniques, how CdSSe alloy quantum dots were determined from a single source precursor, and how specific regions of CdSe quantum dots were identified by solid state nuclear magnetic resonance determining size dependent reconstruction.

High quantum yield (47%) InP nanocrystals can be prepared without the need for post HF treatment by combining microwave methodologies with the presence of a fluorinated ionic liquid. Growing the InP nanocrystals in the presence of the ionic liquid 1-hexyl-3-methyl-imidazolium tetrafluoroborate (hmim BF₄) allows in-situ etching to be achieved. The optimization of the PL QY is achieved by balancing growth and etching rates in the reaction.

The development of ternary nanoscale materials with controlled cross-sectional doping is an important step for the use of chemically prepared quantum dots for nanoscale engineering applications. We report cross-sectional, elemental doping with the formation of an alloyed CdSSe nanocrystal from the thermal decomposition of Li₄[Cd₁₀Se₄(SPh)₁₆]. The sulfur incorporation arises from surface mediated phenylthiolate degradation on the growing quantum dot surface. In the alloy, we identify a pure CdSe nucleus of ~ 1.5 nm consistent with the predictions of nucleation theory. As the particle grows, S²⁻ incorporation increases until the CdSSe reaches ~4 nm where a marked reduction in phenylthiolate content on the nanocrystal is observed in CP-MAS NMR spectroscopy implying rapid decomposition of the phenylthiolate arises with subsequent enhanced S²⁻ incorporation at the level of the stoichiometry of the reaction (namely ~60%). The use of molecular clusters to allow controlled defect ion incorporation can open new pathways to more complex nanomaterials.

Evidence of size dependent reconstruction in quantum dots leading to changes in bonding is observed through analysis of the ⁷⁷Se{¹H} cross polarization magic angle spinning and ⁷⁷Se spin-echo solid state NMR for Cd⁷⁷Se quantum dots. Insight into structural and electronic perturbations experienced within Cd⁷⁷Se is achieved by contact

time dependent $^{77}\text{Se}\{^1\text{H}\}$ CP-MAS measurements providing NMR features assignable to the surface, comprised of multiple layers, coupled to spin diffusion into the core. Due to the nearly 100% enrichment level for ^{77}Se , efficient coupling arises between the surface ^{77}Se and sub-layer ^{77}Se sites due to spin diffusion resulting in long T_2 relaxation times in the Cd^{77}Se quantum dots. The observed chemical shift for the discrete ^{77}Se sites can be correlated to the effective mass approximation via the Ramsey expression indicating a $1/r^2$ size dependence for the change in chemical shift with size, while a plot of chemical shift versus the inverse band gap is linear. The correlation of NMR shift for the discrete sites allows a valence bond theory interpretation of the size dependent changes in bonding character within the reconstructed QD. Based on the NMR results, discrete surface and core ^{77}Se sites exist within Cd^{77}Se QDs where global reconstruction occurs below 4 nm in diameter, while an apparent self-limiting reconstruction process occurs above 4 nm.

CHAPTER ONE

INTRODUCTION

**** The scientific terms and jargon used in chemistry, specifically nanotechnology, can be difficult for the average reader to understand. The introduction of this dissertation is written in such a way that all readers can comprehend the information. The chapters following the introduction, however, are written in more scientific detail. ****

1.1 Background Information

Nanotechnology is a division within science which bridges multiple fields including biology, physics, chemistry and engineering and is the study of the properties and synthesis of semiconductor nanomaterials.¹⁻³ Semiconductor nanomaterials, commonly referred to as quantum dots (QDs), are a unique type of material ranging in size from 2 - 10 nanometers (nm), where a nanometer is 1,000,000,000 times smaller than the length of one meter and can consist of a few hundred atoms to few thousand atoms. In Figure 1.1, a representation of a binary quantum dot can be illustrated and is composed of two parts: positively charged atoms (yellow) and negatively charged atoms (purple).

QDs are unique due to their size dependent properties based on the “particle in a box” model for confinement of the Exciton Bohr radius.⁴ In bulk semiconductors, the distance between the valence (location of ground state electrons) and conduction band (location of excited electrons) is known as the band gap energy. Since the dimensions of bulk semiconductors are much larger than the Exciton Bohr radius, bulk semiconductor energy levels are averaged or continuous. As the semiconductor becomes smaller, it begins to approach the size of the Bohr Radius. Once the size of the semiconductor becomes smaller than the Exciton Bohr radius, the band gap energy levels are no longer continuous and become discrete. This is when the semiconductor no longer has bulk semiconductor properties and is referred to as QDs. At this point the relationship between the size of the QD and the bandgap energy are inversely

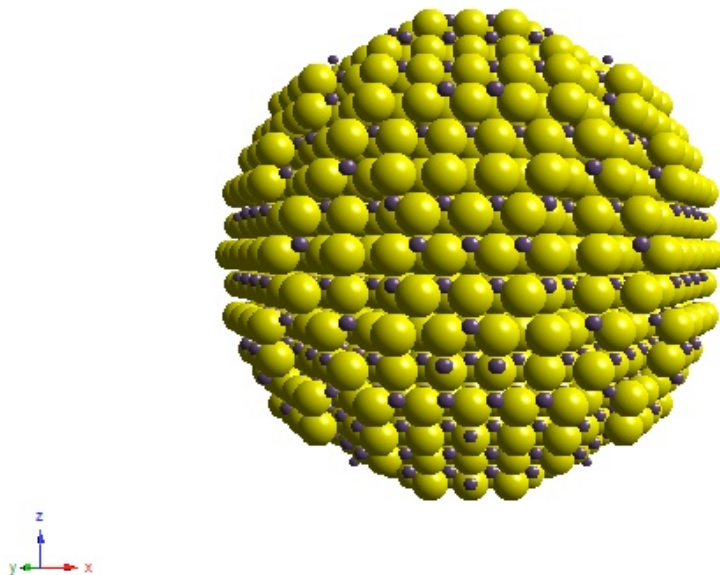


Figure 1.1: Representation of a QD. Yellow spheres would represent the positive charged species (Cadmium or Indium) and purple spheres would represent the negative charged species (Selenium or Phosphorus).

proportional ($E_g \sim 1/R^2$). This relationship between size and bandgap energy is the basis for the “particle in a box” model for quantum confinement and determines the optical properties common in QDs: absorption of light energy and emission of light energy. The “particle in a box” model simply shows that changing the QD size (diameter) results in changes in the overall QD properties. The size dependent confinement properties provide an advantage for QDs over bulk semiconductors. Where bulk semiconductors require more complicated reactions to change their properties, QD properties can be easily changed by only altering the size. QDs have been proposed for many applications due to their size dependent properties including photovoltaics^{5,6} and solar cells⁷⁻¹¹ for energy conversion, bio-markers¹²⁻¹⁴ and sensors^{15,16} for drug detection in medicine and solid state lighting.^{6,17-19}

QDs can be commonly studied by UV-Vis (absorbance) which characterizes the amount of light that a QD can absorb within a specific range. In Figure 1.2A, an

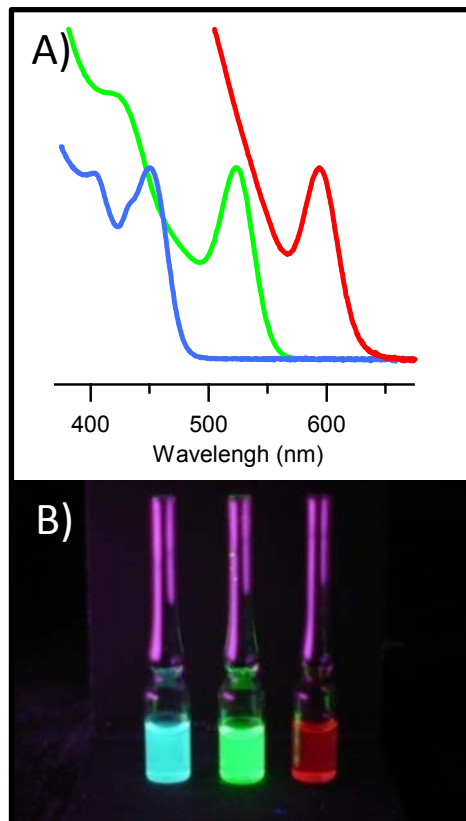


Figure 1.2: A) Absorbance spectra of three different sized CdSe QDs showing size confinement. As the diameter of the QDs is changed from small to large (left to right) the amount of light a QD absorbs changes. B) Three different sized CdSe QDs in solution showing the emission of light by UV radiation. The smallest QD (~2 nm) emits blue, where the mid-sized (~4.0 nm) emits green and the largest (~6.0 nm) emits red.

absorbance spectrum shows the change in the size of cadmium selenide (CdSe) quantum dots based on absorbance, illustrating the “particle in a box” model for confinement. The figure shows that as the diameter of the QD changes the specific quantity of light that is absorbed also changes. The blue line is the smallest QD (2 nm) and has peak absorption of approximately 450 nm while the green line (4 nm) absorbs at 520 nm and is larger than the blue and the red line (6 nm) absorbs at 600 nm and is the largest overall. A better illustration for the “particle in a box” model can be seen in Figure 1.2B (emission) where the same CdSe quantum dots from Figure 1.2A are now dissolved in solution and excited by ultraviolet (UV) radiation. Under these excited conditions, the QDs emit different colors of light based on their size. As the figure shows, the smallest QD emits blue light (450 nm absorption), the middle QD emits green light (520 nm absorption) and the largest QD emits red light (600 nm absorption). As Figure 1.2 shows, the physical properties of a QD can be easily changed by only changing its size.

The size and structure of a CdSe QD can be better illustrated by analyzing it through transmission electron microscopy (TEM). TEM is a high powered microscope that allows for imaging on the nanoscale. In Figure 1.3, a TEM image of CdSe QDs under high magnification shows the individual dots that measure approximately 8 nm in diameter. To put this into perspective, if approximately 12,500 of the QDs in Figure 1.3 were aligned, the total length of the QDs together would equal the thickness (diameter) of a single human hair. Under this magnification, the uniform hexagonal shape as well as the high degree of crystallinity due to the visible lattice fringes (lines pattern within the QD) of the individual QDs can easily be distinguished. Another important structural feature of QDs are the molecules that are bound to the surface, these are called ligands. Ligands are structurally important because they bind to the surface of the QD providing solubility in solution, enhancing confinement properties, preventing aggregation (clumping together) and preventing oxidation. The binding of ligands to the surface of a QD is beneficial as they are responsible for the optical properties of QDs. As a general rule, the better the surface is bound with ligands the better your QDs properties.

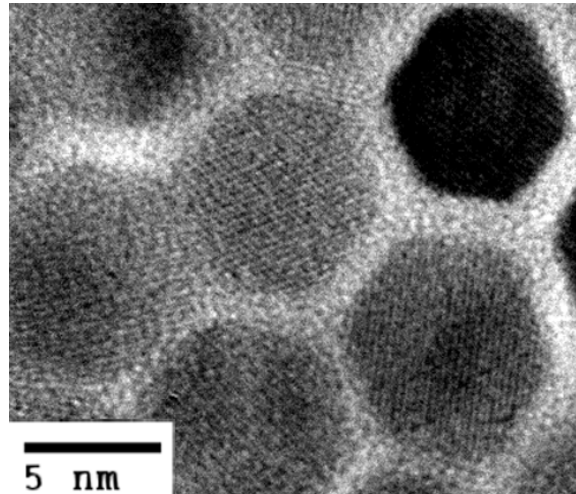


Figure 1.3: Transmission electron microscopy image of Cadmium selenide quantum dots. The dots measure approximately 8 nm in diameter.

1.2 Improving synthetic methods.

Typically QDs have been prepared by lyothermal methods which involve growing QDs in round bottom flasks and heating them by means of an oil bath or heating mantle. Although these techniques are useful, they are not as effective and have only two reaction parameters that can be controlled—time and temperature. Microwave synthesis offers new pathways for growing materials by allowing quicker reactions and more control over lyothermal techniques.²⁰⁻²⁵ Microwave synthesis allows for quicker reactions by heating the reaction precursors (ingredients) on the molecular level through absorption of microwave energy. This technique can be compared to heating food in a microwave oven versus heating on a stove top. Microwave synthesis also offers better control due to the additional reaction parameters—power and pressure.²⁴ Figure 1.4 shows a CEM scientific microwave that was used to synthesize quantum dots.

The III – V quantum dots (Indium Phosphide) are typically more challenging to synthesize than II – VI quantum dots (Cadmium Selenide).^{20,26-29} The III – V materials tend to be more challenging due to the limited choices of reaction precursors, difficulties in controlling size and poor optical properties. The use of microwave synthetic techniques has been shown to grow III – V quantum dots that outperform the lyothermal

counterparts; therefore advances in furthering microwave synthetic strategies for III – V materials must be developed.



Figure 1.4: CEM Discover microwave reactor used to synthesize quantum dots. Unlike residential microwaves, these microwaves are especially built for the rigors of laboratory use.

The synthesis of Indium Phosphide (InP) has been improved by utilizing microwave techniques with fluorinated ionic liquids.²⁰ Ionic liquids are liquid salts that are ideal for microwave synthesis due to their ability to readily absorb microwave energy.³⁰ The InP QDs grown by these methods outperform lyothermal QDs because the ionic liquids in conjunction with microwave reactors provide two advantages that cannot be achieved by lyothermal techniques. The first advantage is the ability to quickly absorb microwave energy, transfer that energy into heat and quickly bring the temperature to reaction temperatures (250 – 280°C). The second advantage is the ability to produce a fluoride ion during the reaction. This allows for a faster overall reaction by activating the reaction precursors. Also, an indium rich surface is produced allowing for more ligands to attach to the surface of the QDs which results in more stable QDs. The use of fluorinated ionic liquids and microwave reactors allows for InP QDs to be grown that have optical properties that surpass the lyothermal grown counterparts.

1.3 Understanding growth of cluster grown QDs

The ability to grow highly emissive quantum dots has many challenges including limited selection of precursors, a need for high temperatures, and the control of shape by reaction kinetics.³¹⁻³⁴ The ability to have a single precursor³⁵⁻³⁷ that synthesizes quantum dots and contains both the positive and negative components would be ideal. The single source precursor, $\text{Li}_4[\text{M}_{10}\text{X}_4(\text{SPh})_{16}]$ (where M is cadmium or zinc and X is Selenium or Sulfur) was developed to provide a convenient experimental way to grow cadmium selenide (CdSe), zinc selenide (ZnSe), cadmium sulfide (CdS) or zinc sulfide (ZnS) quantum dots.³⁷ These single source precursors were shown to grow stable, convenient, and optically competitive QDs. Unfortunately, it was discovered that these QDs, grown with the single source precursor, did not grow binary core quantum dots^{38,39} but instead grew either a core-shell material (where selenium is only in the core and sulfur is only in the shell) or a CdSSe alloy (where the sulfur and selenium atoms are throughout the entire dot). (Figure 1.5)

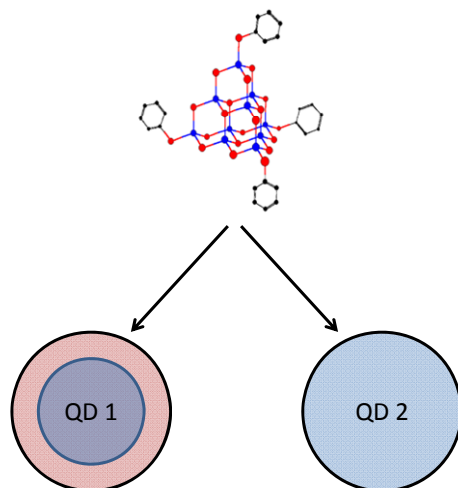


Figure 1.5: Illustration of the single source precursor, $\text{Li}_4[\text{Cd}_{10}\text{Se}_4(\text{SPh})_{16}]$ showing the possible products. QD 1 illustrates a core – shell QD where the core is CdSe and the shell is CdS. QD 2 illustrates an alloy where the QD is CdSSe throughout.

Experimentally it was shown that the thiophenol (SPh) portion of the cluster decomposes and generates sulfur atoms needed to incorporate into the growing quantum dot. The challenge was to identify and determine the location of sulfur atoms (core-shell vs. alloy) as it was incorporated into the growing lattice of the quantum dots. Through multiple analytical techniques, we determined QDs that were synthesized from the single source precursor route resulted in alloy materials as opposed to the before mentioned core-shell materials. The alloyed material varied in sulfur concentration depending on the reaction temperature, time and size of the quantum dot.

1.4 Solid State NMR – a tool for QD analysis

Optical and x-ray analytical techniques, typically used to measure and analyze quantum dots, provide a sample averaged global perspective. To fully understand the changes measured by optical and x-ray analysis, a technique that is element sensitive and sensitive to specific environments within the material to measure the structural changes would be ideal. Analysis by nuclear magnetic resonance (NMR) spectroscopy offers a characterization technique that is element specific technique that is highly sensitive to local chemical and electronic environments.

More specifically, solid state nuclear magnetic resonance (ssNMR) provides a convenient handle to probe specific nuclear sites and analyze site specific regions of solid materials to gain information about the chemical bonding within those sites.⁴⁰⁻⁴³ In a typical ssNMR experiment, samples are usually crystalline powders which are placed in special containers called rotors made out of zirconia. The sample filled rotors are then placed into a magnet which is capable of generating strong magnetic fields and spun at extremely high speeds. Once inside the magnetic field, the nuclear spins of the atoms within the sample of interest interact with the magnetic field. By utilizing the appropriate pulse sequences, different regions or layers (core, surface, passivant) within the quantum dot can be analyzed and studied. (Figure 1.6) ssNMR is not limited to analyzing the atoms of the QD lattice (core, surface and passivation layer), but the ligands attached to the QD can also be detected and studied. This allows ssNMR to be a powerful technique for studying QD structurally.

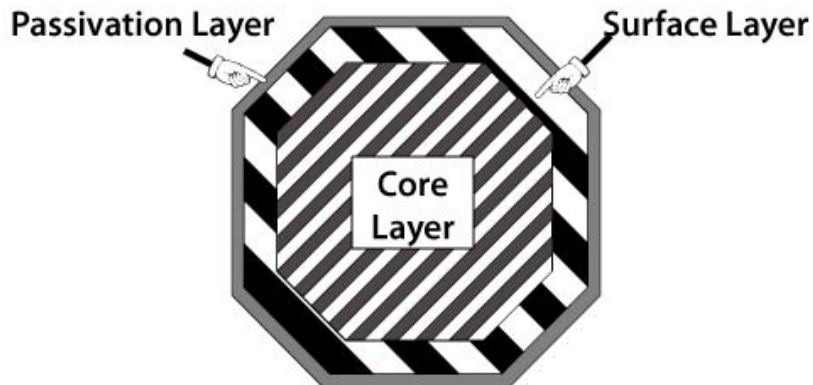


Figure 1.6: Illustration of the different possible layers (passivation, surface, and core) within a quantum dot that can be measured by Solid State NMR.

1.5 Size dependent reconstruction effects measured by ssNMR on Quantum dots.

As previously stated, most analytical techniques cannot analyze specific regions within the quantum dot. Solid state NMR can be used to measure the degree of crystallinity, level of reconstruction and the surface ligands bound to the QD. Solid state NMR is an analytical technique that allows for specific regions to the QDs to be distinguished by the use of specific pulse techniques.

Spin echo (Figure 1.7 A) is a specific pulse technique that allows for more global analysis of the lattice properties of the entire QD. Using these spin echo techniques, quantitative amounts of the different nuclei spin populations can be determined. The different nuclei populations or contributions from the spin echo technique allow for a size dependent trend for the surface to core to be determined.

Cross polarization magic angle spinning (CP-MAS) is a technique that allows the surface of the QD to be selectively studied (Figure 1.7 B). CP-MAS techniques polarize abundant nuclei then transfer that magnetization to nuclei which are less abundant. The polarization transfer is from the abundant ^1H spins on the passivating surface ligands to the nuclei within the QD lattice. Therefore only nuclei at or near the surface ligands of the particle can be measured.

Through the use of isotopically abundant prepared QDs (QDs where nuclei of interest are all NMR detectable), CP-MAS techniques were used to not only enhance surface nuclei but the ability to also detect sub-layer nuclei were possible by spin diffusion events. Spin diffusion is the ability to transfer nuclear magnetization from nuclei to nuclei of the same nuclei. Spin diffusion was enhanced by varying the contact time within the CP-MAS experiment. The combination of enriched QD samples and spin diffusion through CP-MAS allows the ability to depth profile the surface sub-layers providing evidence of size dependent surface reconstruction.

Surface reconstruction is a phenomenon where stress or compression arises due to the changes in bond lengths and angles due to the small sizes of QDs. Solid state NMR provides a technique to measure and understand the impact size dependent surface reconstruction QDs experience. The degree and depth of reconstruction leads to differences in broadening of the NMR signal based on size. Also different chemical shifts are observed for different regions within the quantum dot as well as changing in size.

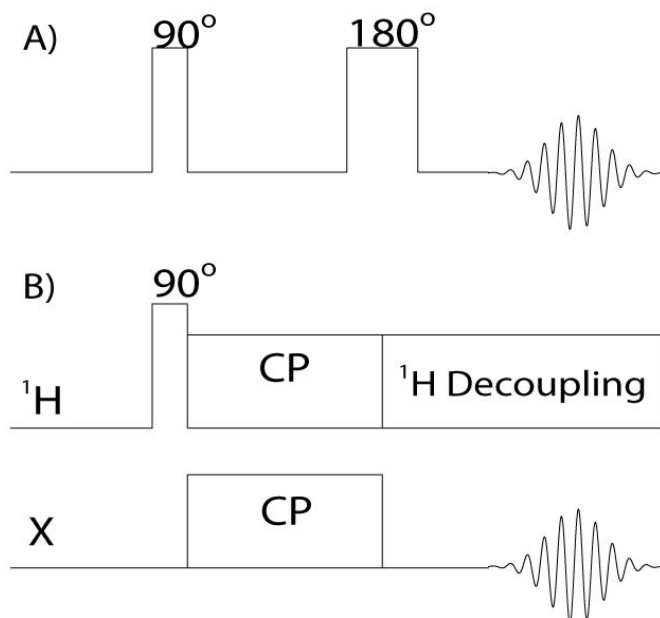


Figure 1.7: Solid state NMR pulse sequences A) spin echo B) cross polarization magic angle spinning (CP-MAS) used to measure QD. Spin echo used to measure the whole QD while CP-MAS can be used to measure specific sites within the QD.

1.6 Summary of chapters

This dissertation on nanotechnology describes novel approaches using microwave synthesis to grow nanocrystalline semiconductor QDs; explains growth mechanics and properties of nanomaterials from single source precursors; and characterizes QDs by solid stated nuclear magnetic resonance techniques. More specifically, chapter two describes a novel method of growing Indium Phosphide (InP) quantum dots using Ionic Liquids (IL) and microwave synthetic techniques. The use of an IL and microwave synthesis resulted in the highest quantum efficient InP that has been synthesized without post reaction treatment. Chapter three delves into understanding the growth dynamics and identification of the resultant QDs grown from a single source precursor. A combination of multiple analytical techniques was used to determine QDs grown with the single source precursor were alloy materials. Finally, chapter four describes the use of solid state nuclear magnetic resonance as a tool for nanomaterial characterization. The use of solid state NMR is advantageous because it allows for specific areas of the QD to be probed giving insight into the degree of surface reconstruction that may exists in these QDs at specific sizes.

CHAPTER TWO

MICROWAVE INDUCED IN-SITU ACTIVE ION ETCHING OF GROWING INP NANOCRYSTALS

*Reproduced with permission from Nano Letters.
Copyright 2008 American Chemical Society.*

2.1 Introduction

The size dependent optical properties of colloidal semiconductor nanocrystals are ideal for applications in fields ranging from biological imaging⁴⁴⁻⁴⁷ to photovoltaics.⁴⁸⁻⁵⁰ Due to the ease of synthesis, a significant fraction of the research to date has centered on the II-VI family of semiconductors utilizing the type I core-shell structures, namely CdSe/ZnS.^{51,52} Recent interest has focused on developing routes to the III-V family, namely InP,^{24,28,29,53} due to the perceived lower toxicity for InP based nanocrystals.^{46,53-57} The downside to InP is the poor photoluminescence (PL) quantum yield (QY), which is typically < 4% once isolated from the reaction mixture, although core-shelling yields a value of ~ 20% depending on size.^{27,28} The poor PL QY performance for these materials can be traced to the presence of phosphorus vacancies²⁹ (V_P) in the material. Removal of the surface V_P sites by active ion etching with hydrofluoric acid (HF) improves the PL performance of these materials to ~40%.^{24,26,29,58} Active ion etching of InP nanocrystals with HF is believed to improve the QY via removal of P dangling bonds that arise from the P rich faces of the growing nanocrystal. By etching away the P faces in the form of PF_3 , an In rich face is exposed that provides for more efficient passivation.^{24,29} The process is believed to be enhanced by photoactivation via an electron transfer step, although HF etching without light also produces PL enhancement.⁵⁸ Although the use of active ion etching with HF enhances the InP nanocrystal PL, it represents an inconvenient extra synthetic step that lowers solubility, broadens the excitonic absorption line width, and increases the difficulty for ZnS shelling. The development of an in-situ active ion etchant can simplify the preparation of this family of material, improve the PL QY, and maintain the optical properties of the nanocrystal.

A microwave induced in-situ active ion etching process is demonstrated that improves the out-of batch optical performance of InP nanocrystals, although the methodology is likely to be applicable to a wider range of nanocrystals. In-situ active ion etching is achieved by adapting our previously developed microwave (MW) based synthetic protocol²⁴ by the addition of the ionic liquid 1-hexyl-3-methyl-imidazolium tetrafluoroborate (*hmim* BF₄). In-situ generation of F⁻ (active ion) is achieved through direct MW absorption by the IL, thermal relaxation to the fluoride containing counter-ion, and subsequent production of F⁻ resulting in V_p removal during the growth of the InP nanocrystal. The photoluminescence quantum yield (PL QY) for InP grown under in-situ etching conditions is 47% for the additive *hmim* BF₄ at a mole ratio of 1:10 (In³⁺ to IL). Time dependent degradation studies of the InP grown with the IL indicates the PL properties are maintained in solution for an extended time frame with no detectable change in PL QY after 24h. The in-situ, microwave assisted active ion etching method represents the first technique to produce high PL QY InP nanocrystals out of batch without using post HF treatment or core-shelling. More importantly, it points to a methodology that allows in-situ vacancy or defect removal during the chemical preparation of nanocrystals.

The use of ionic liquids in synthesis have attracted attention due to the high thermal stability of the solvent, non-reactivity of the materials, and the added benefit of the solvent being recyclable.⁵⁹ In an earlier report, our group demonstrated the advantages of using non-fluorinated ionic liquids in MW chemistry to accelerate growth of InP and CdSe nanocrystals.²⁴ The isolated InP showed typical PL QYs for this family with values on the order of 4%. Following HF treatment the PL QY increases to 38%.²⁴ The most notable effect of using an ionic liquid in MW chemistry is the efficient conversion of MW energy into thermal energy due to the high MW cross-section that ionic liquids possess. In MW chemistry, the molecule with the highest cross-section selectively absorbs the MW energy and through relaxation heats the solvent or the molecular precursors. The selective absorption leads to the “specific” microwave effects often quoted in the synthetic literature.⁶⁰ Ionic liquids typically are not directly involved in the reaction mechanism and can be considered a spectator solvent, allowing non-absorbing materials to be rapidly heated in the MW by convective loss; although ILs

are believed to enhance reactions due to the highly ordered solvent framework.^{59,61} Choosing an ionic liquid containing a fluorinated anion that thermally degrades would circumvent the HF step by directly producing an in-situ F^- source. The concentration of F^- would be controlled by the MW absorption cross-section of the IL and subsequent thermal degradation of the fluoride source.

It is well known from the literature that PF_6^- and BF_4^- anions are prone to thermal decomposition producing controlled quantities of F^- ions. The thermal production of fluoride ions arises from a Balz-Schiemann type reaction.⁶²⁻⁶⁴ In fact, it has been shown that tetrafluoroborate based ionic liquids thermally decompose at 240 °C at a rate of 0.017 %/min.⁶⁵ In order to assess the effect on the PL QY of InP by the addition of fluorinated ILs during nanocrystal growth, we have investigated a series of ILs based on 1-hexyl-3-methyl-imidazolium (*hmim*), 1-butyl-4-methyl-pyridinium (*bmpy*), and tetrabutylammonium (*TBA*) with the counter-ions $[BF_4]^-$, $[PF_6]^-$, F^- , and Cl^- (Table 2.1).

2.2 Experimental

The InP nanocrystals are prepared by injecting separate stock solutions of indium palmitate and tris-trimethylsilylphosphine $[(TMS)_3P]$ dissolved in decane into a microwave reactor vessel containing fixed concentrations of the additive in Table 1. The synthetic method is an extrapolation of literature procedures^{24,53} using separate stock solutions of the precursors that are mixed prior to MW irradiation. MW growth is accomplished by ramping the reaction at 300 W (single mode, focused, 2.45 GHz) using a CEM Discover Microwave reactor. The general parameters used in this work are as follows: 1) reaction power of 300 W (ramping time from 1 – 25 minutes depending on additives), 2) reaction temperature at 280 °C, and 3) reaction time of 15 minutes with “active cooling” of the microwave cavity to remove latent heat. It should be noted that the ramping conditions may vary depending on the choice of additives or MW system used. Once the MW reaction is complete, the temperature is rapidly reduced to room temperature (~2 min) using forced air cooling. For the optical studies, the InP nanocrystals are isolated from the reaction mixture by initial addition of toluene and precipitation by addition of acetone, followed by treatment with toluene/MeOH (2x). The quantum yields were determined by comparing the emission of InP with that from rhodamine 6G in ethanol (QY = 95%), as described previously.²⁴

Table 2.1: List of Ionic fluorinated and non-fluorinated additives used for in-situ growth of InP Quantum Dots.

Anion	Additive	Abbrevia- tion	Ratio	PL QY	Ramp Time (sec)	
[BF ₄] ⁻	1-hexyl-3-methyl-imidazolium BF ₄	hmim BF ₄	1:20	35.3	55	
		hmim BF ₄	1:10	47.1	70	
		hmim BF ₄	1:5	41.6	225	
		hmim BF ₄	1:3	34.6	410	
		hmim BF ₄	1:2	8.8	340	
		hmim BF ₄	1:1	1.7	760	
		hmim BF ₄	1:0.1	1.2	810	
	1-butyl-4-methyl-pyridinium BF ₄	bmpy BF ₄	1:20	29.5	180	
		bmpy BF ₄	1:10	43.2	220	
		bmpy BF ₄	1:5	9.9	250	
		bmpy BF ₄	1:3	2.7	325	
		bmpy BF ₄	1:2	3.8	435	
		bmpy BF ₄	1:1	1.6	590	
		bmpy BF ₄	1:0.1	1.3	1320	
	tetrabutylammonium BF ₄	TBA BF ₄	1:10	11.2	170	
TBA BF ₄		1:1	4.2	370		
TBA BF ₄		1:0.1	1	1735		
[PF ₆] ⁻	1-hexyl-3-methyl-imidazolium PF ₆	hmim PF ₆	1:10	24.5	150	
		hmim PF ₆	1:1	5.7	310	
		hmim PF ₆	1:0.1	1.8	485	
	1-butyl-4-methyl-pyridinium PF ₆	bmpy PF ₆	1:10	N/A	220	
		bmpy PF ₆	1:1	1.8	302	
		bmpy PF ₆	1:0.1	1	485	
	tetrabutylammonium PF ₆	TBA PF ₆	1:10	N/A	305	
		TBA PF ₆	1:1	1	432	
		TBA PF ₆	1:0.1	1	1065	
	F ⁻	tetrabutylammonium fluoride	TBA F	1:10	N/A	190
			TBA F	1:1	N/A	295
			TBA F	1:0.1	1	720
Cl ⁻	1-hexyl-3-methyl-imidazolium Cl	hmim Cl	1:10	N/A	135	
		hmim Cl	1:1	N/A	430	
		hmim Cl	1:0.1	2.3	670	
	1-butyl-4-methyl-pyridinium Cl	bmpy Cl	1:10	N/A	140	
		bmpy Cl	1:1	N/A	494	
		bmpy Cl	1:0.1	1.5	1332	

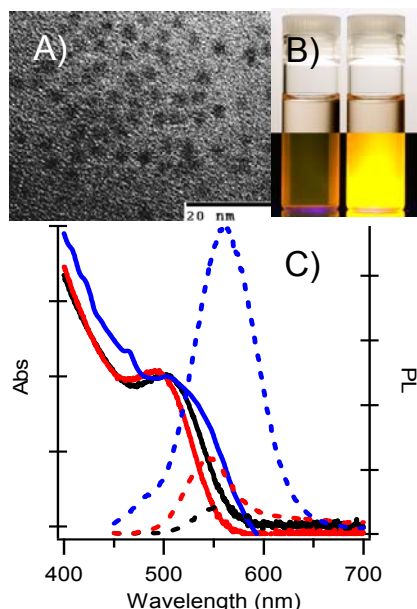


Figure 2.1: A) TEM of grown InP with *hmim* BF₄ B) Optical image comparing the solution of InP nanocrystals (hexane) for materials grown with and without *hmim* BF₄ (1:10 mole ratio). The lower half of the image is under UV irradiation C) Comparison of Abs and PL of InP grown with *hmim* BF₄. Concentrations of the In³⁺ precursor to the IL used are 1:0.1 (black), 1:1 (red), and 1:10 (blue).

2.3 Results / Discussion

Using TEM, the MW grown InP are 2.7 ± 0.3 nm spherical, Zn-blende (cubic) morphology nanocrystals (Figure 2.1A). The large disparity represents an upper limit due to imaging imitations for these materials at this size regime. pXRD analysis (Figure 2.2) of the sample indicates a Zn-blende structure (F-43m) is formed. Scherrer analysis of the pXRD confirms the TEM size measurement. Solid state nuclear magnetic resonance spectroscopy (Figure 2.3) shows that fluorine is still present after material isolation on the InP samples grown by these methods. This is in agreement with InP that has been HF etched.²⁹

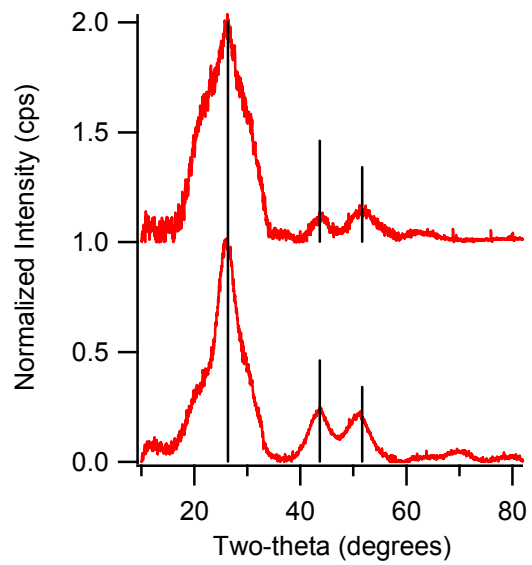


Figure 2.2: A) pXRD InP grown with bmpy BF₄ B) InP grown with hmim BF₄

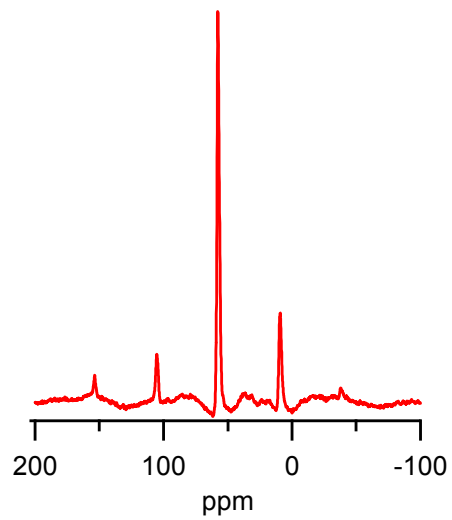


Figure 2.3: ¹⁹F MAS of InP grown with bmpy BF₄. 2.5 mm rotor and a spinning speed of 22 kHz

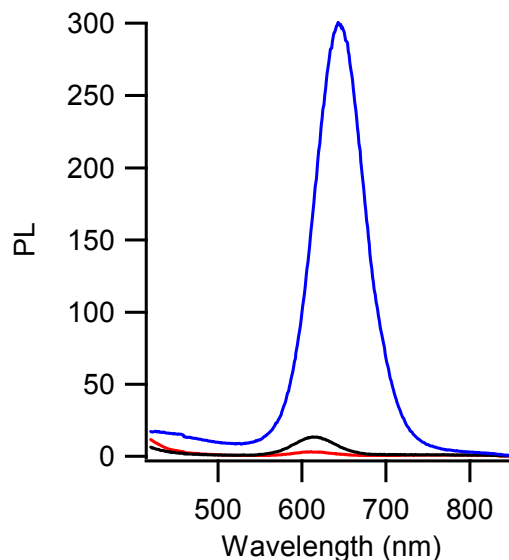


Figure 2.4: Concentration dependent PL comparison of InP grown from *bmpy* BF₄. 1:0.1 (red), 1:1 (black), 1:10 (blue)

The magnitude of enhancement resulting from adding *hmim* BF₄ to the MW reactor is clearly evidenced in the dramatic PL improvement observed for the InP nanocrystal grown in the presence and absence of the IL (Figure 2.1B). The changes in the absorption and PL spectra for InP grown with the additive added in a 1:0.1, 1:1, and 1:10 mole ratio of *In*³⁺ to *hmim* BF₄ are shown in Figure 2.1C. The PL QYs for each additive condition is compiled in Table 1. The [BF₄]⁻ salts showed the highest overall PL QY improvement, the [PF₆]⁻ based ILs produced lower QYs, while the *F*⁻ and *Cl*⁻ salts did not produce highly emissive materials or led to loss of the nanocrystal. An important set of controls were also run on the IL's (*hmim*, *bmpy*, and TBA) with a chloride counterion. In all reactions, the chloride salt resulted in precipitation of the *In* precursor, presumably due to facile formation of InCl₃. The highest PL QY arises for the ionic liquid *hmim* BF₄ at a concentration of 1:10. At this concentration it was possible to reproducibly grow InP with a PL QY of 47%. No spectral shift for the PL profile is observed for the various concentrations of *hmim* BF₄ (Figure 2.1 C) or *bmpy* BF₄ (Figure 2.4); however as the concentration of IL is increased the InP PL QY asymptotes for the *hmim* BF₄ at a concentration above 1:5, while *bmpy* BF₄ asymptotes at 1:10 (Figure 2.5). The difference in *hmim* and *bmpy* can be explained due to the higher polarity of

hmim, and therefore higher MW absorption and subsequent thermal transfer from the IL to the counterion.⁶⁶ The higher thermal transfer leads to higher fluoride ion release in the reaction.

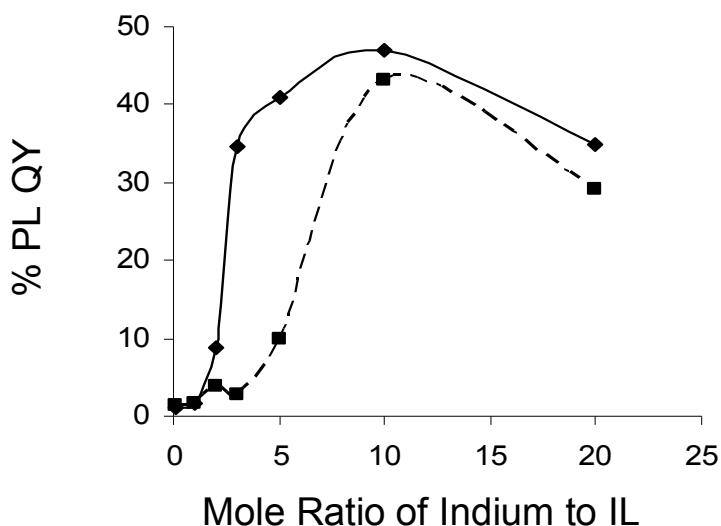


Figure 2.5: PL QY for a series of In^{3+} : IL mole ratios of InP grown with *hmim* BF_4 (solid) and InP grown with *bmpy* BF_4 (dash).

The observed InP PL QY depends on both the IL and the concentration of IL. For samples grown with a 1:10 mole ratio of the IL the trend observed is $\text{BF}_4^- > \text{PF}_6^- \gg \text{Cl}^-$, while at a 1:1 ratio the PL QY follows the trend $\text{PF}_6^- > \text{BF}_4^- \gg \text{Cl}^-$ (Figure 2.6). The observed anion dependence on IL mole ratio reflects the magnitude of F^- production, with PF_6^- having the highest fluoride ion production in time compared to BF_4^- . The level of fluoride ion production mirrors the bond energies for the B-F bond (174 kcal/mol) compared to the P-F bond (96 kcal/mol).⁶⁷ The weaker bond strength in P-F will result in more facile thermal degradation and therefore higher fluoride ion concentrations. At high IL mole ratios the increased fluoride ion concentration leads to aggressive etching and subsequent loss of the materials.

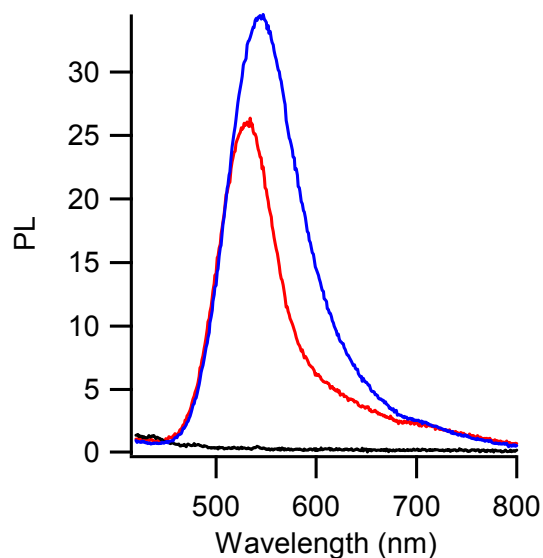


Figure 2.6: Comparison of PL properties for InP grown with a 1:1 mole ratio of *hmim* PF₆ (blue), *hmim* BF₄ (red), and *hmim* Cl (black).

To assess whether the PL improvement requires an IL with a high MW cross section or just an anion capable of producing fluoride ion, TBA salts of BF₄⁻, PF₆⁻, and F⁻ were tested at reaction temperatures of 280°C, which is high enough to initiate anion degradation. Inspection of Table 2.1 illustrates that the combination of IL and counterion is necessary to achieve high PL QY in these materials. Although PL QY improvement is observed for TBA BF₄, the PL QY for TBA BF₄ was far lower (11%) than observed for either *hmim* BF₄ (47%) or *bmpy* BF₄ (43%). For the TBA salts, the magnitude of PL QY followed the trend BF₄⁻ >>> PF₆⁻ ~ F⁻. At high concentrations of the PF₆⁻ or F⁻ salts the InP nanocrystals are not formed. As noted earlier, it is believed that for the PF₆⁻ and F⁻ salts, more rapid fluoride generation exists in the reaction and the resultant F⁻ ions inhibit InP growth due to formation of InF₃ and reaction with the *P* source with subsequent formation of PF₃. The difference in PL QY between TBA and *hmim* can be explained due to the lower microwave absorption by TBA during the reaction resulting in lower F⁻ production for the ILs during the InP growth. The lower MW cross section for TBA is clearly evidenced by the longer MW ramp times observed for the TBA salts (Table 2.1).

2.4 Conclusion

The experimental results suggest that a slow, controlled production of fluoride ions during nanocrystal growth is crucial to produce the highest PL QY in InP. The slow production of fluoride ions apparently allows controlled removal of defects to compete with nanocrystal growth. The actual mechanism of etching is presumed to follow a similar pathway as observed in Si nanocrystals⁶⁸ and InP nanocrystals^{29,58} where the presence of HF leads to removal of oxidized *P* or enhances the cleavage of the Si-P bond, which arises from the P^{3-} precursor (TMS_3P). The oxidized *P* sites likely are generated by thermal decomposition of In-palmitate or the In-acetate precursor. Alternatively excess F^- ions may also interact with dangling *P* ions at the nanocrystal surface, consistent with the NMR results and our previous observations²⁴ (Figure 2.3). At high fluoride ion concentrations (PF_6^- vs. BF_4^-), the rate of etching is faster than the rate of the growth resulting in poor material performance. At low fluoride ion content (*hmim* BF_4 vs. *bmpy* BF_4) the reaction results in faster growth than etching, which yields poor PL QYs. The balance of etching and growth imply that during synthesis of InP nanocrystals an ionic liquid with a fluoride counter ion serves two functions: 1) to super-heat the reaction due to the high absorption cross section for microwave energy of the IL converting that energy to convective energy, and 2) production of a transient in-situ source for fluoride ions by thermal degradation of the counter-ion. MW chemistry allows the careful control of etching relative to growth by balancing the MW cross section of the reactants with the thermal degradation rate for the fluoride containing IL. The careful control provided by the MW leads to a rapid, convenient synthetic methodology allowing isolation of InP nanocrystals with nearly 50% PL QYs that is adaptable to a flow through technology.²³ Such a technology may open the use of these materials in bio-imaging applications where toxicity issues are a concern for bio-nanotechnology.

CHAPTER THREE

COMPOSITION CONTROL AND LOCALIZATION OF S^{2-} IN CDSSE QUANTUM DOTS GROWN FROM $Li_4[Cd_{10}Se_4(SPh)_{16}]$

*Reproduced with permission from Journal of the American Chemical Society.
Copyright 2008 American Chemical Society.*

3.1 Introduction

Preparation of emissive quantum dots (QDs) have evolved to the point where very narrow size dispersions of the desired binary or ternary semiconductor can be prepared routinely, whether through the use of molecular reactants,^{32,69,70} single source dual component precursors,⁷¹ or single source inorganic clusters.^{35-37,72} The growth of the II-VI QDs from inorganic clusters, while well documented,^{24,40,73-86} is mechanistically poorly understood. Depending on the reaction temperature and conditions, we⁷² and others³⁸ have observed variable concentration of S^{2-} incorporation into CdSe QDs grown from $[Cd_{10}Se_4(SPh)_{16}]^{4-}$, the parentage of which can be traced to phenylthiolate decomposition at the QD surface. Incorporation of S^{2-} is not surprising based on earlier studies by Wang and Herron for CdS formation from the cluster $[Cd_{10}S_4(SPh)_{16}]^{4-}$, where 60% of the S^{2-} incorporation came from phenylthiolate ligand decomposition.⁸⁷ They observed a surface mediated cleavage reaction between two bridging SPh^- groups with ensuing production of S^{2-} and loss of diphenyl sulfide. Extrapolation of these results to the growth of QDs from $[Cd_{10}Se_4(SPh)_{16}]^{4-}$ would suggest a CdSSe alloy with a composition approaching 60% S^{2-} might be expected based on stoichiometry. However, the rate of incorporation would be influenced by the rate of decomposition of the phenylthiolate which is both temperature dependent and surface area dependent on the growing QD.

In this solid solution the anion distribution throughout the QD may exist as a homogeneous, heterogeneous, gradient, or perhaps a core-shell^{52,70} depending on the competition between phenylthiolate decomposition, phenylthiolate concentration, and rate of S^{2-} versus Se^{2-} addition to a growing QD surface. (Figure 3.11)

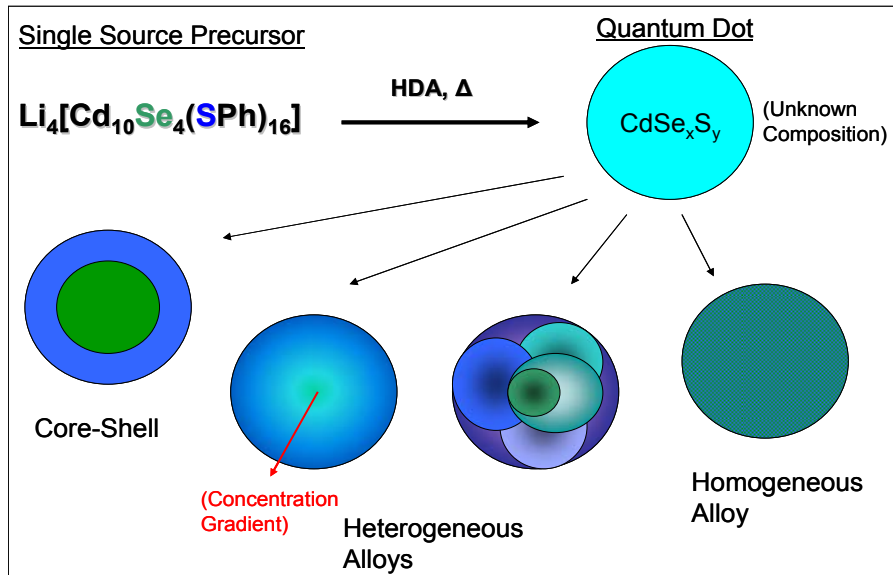


Figure 3.1: Possible composition scenarios for a CdSSe QD grown from the cluster, $\text{Li}_4[\text{Cd}_{10}\text{Se}_4(\text{SPh})_{16}]$.

The possibility of a core-shell motif was first suggested by Gamelin, et al³⁸ due to the observation of enriched S^{2-} content at the QD surface. A core-shell motif is not necessary to observe enrichment of S^{2-} at the surface based on our NMR observation⁴⁰ of strongly bound SPh^- at the QD surface, which would result in the identical conclusion of S^{2-} enrichment but not imply a core-shell motif. The remarkable stability of the phenylthiolate at the surface (impervious to ligand exchange in pyridine) and the lack of detrimental effects on the quantum yield implies that the phenylthiolate anion exists either bound to the face or on unique vertex and edge sites, as suggested in our earlier study.⁴⁰ These results have prompted a more in-depth study into understanding the quality of the resultant QD grown from the inorganic cluster source, the nature of the anion distribution in the solid solution, and the complexity associated with the incorporation of defect ions into a growing QD.

A CdSSe alloy is observed in the size regime greater than 1.5 nm, with a S^{2-} incorporation value of ~60% for sizes in excess of 3.5 nm. The correlation of stoichiometry and microanalysis of the CdSSe alloy is remarkable, but does not imply that the alloy is uniform overall size regimes. By correlating X-ray fluorescence (XRF),

thermogravimetric analysis (TGA), solid state NMR, UV-Vis absorption, and powder XRD (size analysis), we demonstrate the formation of a CdSSe gradient as the QD grows. The size of the QDs in this study was calculated based on Debye-Scherrer analysis of the pXRD <110> face which has been demonstrated to be valid for QD size estimation. The largest sizes were validated also by TEM. The optical absorption of the CdSSe materials shows a blue shift in the energy due to the increasing S²⁻ content, as predicted by the effective mass approximation for a ternary semiconductor. Solid State NMR analysis provides evidence of a combination of TOPO and the phenylthiolate species passivating the CdSSe nanocrystals below 5 nm. Above 5 nm no phenylthiolate contributions are observed and the S²⁻ content in the nanocrystals asymptote in the XRF analysis. SSNMR correlated to XRF and effective mass approximation studies lead us to conclude that an⁻ ion distribution approaches the stoichiometric value of 60% for sulfur and 40% for selenium.

3.2 Experimental

3.2.1 Chemicals. The molecular clusters Li₄[Cd₁₀Se₄(SPh)₁₆] and Li₄[Cd₁₀Se₄(SePh)₁₆] were prepared as previously described.^{39,88,89} Hexadecylamine (HDA, 90%), 85% H₃PO₄, 12 M HCl, were used without further purification.

3.2.2 Instrumentation. Elemental composition for Cd²⁺, S²⁻, and Se²⁻ was carried out in an Oxford Instruments ED2000 X-ray fluorescence (XRF) spectrometer with a Cu-K_α source. The mole ratio for Cd²⁺ to Se²⁻ to S²⁻ for each sample was analyzed using XRF with four repeat analyses for statistical validation. For a standard XRF measurement, the powdered samples were completely dissolved in 90% HNO₃ to allow total elemental composition to be analyzed. In order to allow compatibility with the XRF sample holder, the samples were heated to remove excess NO_x and then diluted to ~5 mL with a 2% HNO₃ solution. All measurements were carried out at the K_β line for the element, Cd²⁺ (23.1 keV), Se²⁻ (11.2 keV), and S²⁻ (2.3 keV). Total counts need to be above 10 cps to reduce error in the analysis. Calibration curves were generated using commercially prepared 1000 ppm elemental standards in 2% HNO₃, which results in accuracies of ±3 ppm for Cd²⁺, ±4 ppm for Se²⁻, and ±16 ppm for S²⁻. Composition analysis of bulk samples were used to further validate the method.

Optical absorption was analyzed in a 1-cm cell in toluene ($\sim 1 \times 10^6$ mol) using a Cary 50 UV-Vis spectrophotometer. Powder X-ray diffraction (pXRD) was carried out on a Rigaku DMAX 300 Ultima 3 diffractometer using Cu-K α ($\lambda = 1.5418$ Å) with the d-spacing calibrated to a Si 0 standard to verify crystal motif. Using the Debye-Scherrer formula (Eq. 1) the QD diameter was calculated,

$$\tau = \frac{K\lambda}{\beta \cos\theta} \quad (1)$$

where τ is the QD diameter, λ is the X-ray wavelength, β is the full width at half maximum of the peak, θ is the angle at the peak, and K is the shape factor. The <110> peak was used to calculate the QD diameter to eliminate complications from overlapping reflections. QD sizes and morphology were verified and the shape factor calibrated by transmission electron microscope (TEM) for select samples using a JEOL-2010 operated at 200 kV. The QDs were dispersed on holey carbon (400 mesh) from a toluene solution.

Thermogravimetric Analysis (TGA) samples were placed into alumina crucibles for analysis on an SDT 2960 (Simultaneous DSC TGA) and were heated to 300 °C or 600 °C at a rate of 2 °C/min under a flow of N $_2$ gas at 60 mL/min. Percent weight loss was determined for each sample using the accompanying TA Universal Analysis 2000 software package. A 3.5 and 5.7 nm CdSSe alloy grown from the cluster was measured by TGA at 300 °C and at 600 °C and the resultant powder analyzed by XRF for S $^{2-}$, Se $^{2-}$, and Cd $^{2+}$ content.

Solid State ^{13}C CP-MAS NMR experiments were performed at room temperature on a Varian Unity/Inova 500 MHz spectrometer with a 2.5-mm broadband MAS probe double tuned to ^1H (500.3 MHz) and the X channel to ^{13}C (125.8) MHz. A spinning speed of 12 kHz was used on all experiments. ^{13}C CP-MAS experiments were performed on Li $_4$ [Cd $_{10}$ Se $_4$ (SPh) $_{16}$], TOPO capped CdSSe grown from Li $_4$ [Cd $_{10}$ Se $_4$ (SPh) $_{16}$], CdSe and CdSe recapped with thiophenol by ligand exchange procedures was prepared by Cd stearate microwave synthesis. Optimum ^{13}C CP-MAS experiments were acquired using an acquisition time of 50 ms, a recycling delay of 3 sec, a contact time of 1.6 ms and a ^1H 90° pulse length of 5 μs . ^{13}C CP-MAS build up

curves were created by varying the contact time between each experiment (0.5, 1, 1.6, 2, 2.5, 5 ms). The chemical shifts were referenced to TMS (0 ppm).

3.2.3 Synthesis of CdSSe QDs from $\text{Li}_4[\text{Cd}_{10}\text{Se}_4(\text{SPh})_{16}]$. A series of CdSSe QDs (2 – 5.7 nm) were prepared from the single source inorganic cluster $\text{Li}_4[\text{Cd}_{10}\text{Se}_4(\text{SPh})_{16}]$ in HDA at 230 °C. QDs below 2.0 nm were also prepared and isolated by carrying out the identical reaction at lower temperature (120 °C). The generic reaction was carried out in a flame dried round bottom flask in which 200 g of hexadecylamine (HDA) was added, degassed, and placed under Ar at 70 °C for ~1.5 h; and then raised to 120 °C. To the HDA was added 2.0 g of $\text{Li}_4[\text{Cd}_{10}\text{Se}_4(\text{SPh})_{16}]$ (as a powder) and the reaction temperature was increased to 230 °C at an approximate rate of 1-2 °C /min. Aliquots (15 mL) were isolated every 10-20 nm. These samples were isolated from the reaction mixture and purified using standard dissolution - precipitation protocols, in which the aliquots were solvated in toluene, methanol was added to induce precipitation, and centrifugation to collect the precipitate (3x). A final purification step was applied by dissolving the precipitate (20 mg) into liquid TOPO (1 g, 80 °C) for 5 min and precipitation of the QD from the TOPO using the above dissolution-precipitation procedure above. TOPO exchange was utilized based upon the literature precedence implying the surface of CdSe nanocrystals may be etched by treatment with TOPO, although no significant impact on the cation to anion ratio was observed.³⁹ The samples were stored under vacuum following isolation of the solid.

3.2.4 Synthesis of CdSe QDs from $\text{Li}_4[\text{Cd}_{10}\text{Se}_4(\text{SePh})_{16}]$. A pure CdSe QD was grown from the molecular precursor $\text{Li}_4[\text{Cd}_{10}\text{Se}_4(\text{SePh})_{16}]$ in an analogous fashion to the alloyed materials. Briefly, to a flame dried round bottom flask 40 g of HDA was added, degassed, and placed under Ar at 70 °C for ~1.5 h. To the HDA was added 400 mg of $\text{Li}_4[\text{Cd}_{10}\text{Se}_4(\text{SePh})_{16}]$ prepared by previously published methods.³⁹ The reaction was heated to 230 °C and monitored by absorption spectra until the desired sizes were reached. These samples were cleaned by selective precipitation with toluene/methanol, followed by TOPO exchange.

3.2.5 Microwave Synthesis of CdSe QDs from Cd stearate (CdSA). A pure CdSe QD was grown from the reaction of cadmium stearate (CdSA) and TOPSe as described previously.²³ The reaction was carried out in decane in a CEM microwave (300W) at

230 °C for 30 sec. This sample was cleaned by selective precipitation with toluene/methanol. Size was confirmed by optical absorption and pXRD. Thiophenol was ligand exchanged onto the CdSe surface by dissolving the CdSe sample into thiophenol and sonication at ~45 °C for 1hr.

3.2.6 Homogeneous Acid Etching of CdSSe QDs. Uniform etching of the crystallite faces can be accomplished with a II-VI specific etchant using a 1:1 (V:V) 12 M HCl:85% H₃PO₄.⁹⁰ To etch the QD samples, the acid etchant (50-200 μL depending on degree of etching desired) was added to 50 mg of the CdSSe QD in excess TOPO with 1 mL of toluene and allowed to stir for ~1 min. The solution was quenched and the etched QDs precipitated by addition of methanol. The size of the QD was verified by TEM and absorption analysis.

3.3 Results / Discussion

QD growth, whether from elemental or single source precursors, is controlled by the nucleation and growth steps of the reaction. Growth begins with a pure nucleus (nucleation step) and can incorporate defects as the crystallite grows depending on the concentrations and the kinetics for the specific ion addition to the growing nanocrystal surface.² When the single source cluster reaction is carried out in a strongly coordinating solvent, it is presumed that QDs are generated from a similar mechanism as proposed by Wang and Herron for formation of CdS bulk materials from [Cd₁₀S₄(SPh)₁₆].^{35-37,71} na^{24,38-40,72-87,91,92} The mechanism is believed to involve cluster coupling induced by loss of the terminal phenylthiolate, with subsequent growth occurring by a combination of cluster rearrangement into the bulk structure and S²⁻ incorporation arising from decomposition of the [Cd(SPh)₄]²⁻ or SPh⁻ with the formation of CdS and (Ph)₂S at the nanocrystal surface. In effect, the cluster has a core Cd₆S₄, and the stoichiometry is balanced in the reaction by the decomposition of the four Cd(SPh)₄ caps to produce



six additional S²⁻ ions, six diphenyl sulfides, and four Li-SPh. The decomposition of the tetrahedral capping moieties balance the Cd : S ratio in this material.

The decomposition of phenylthiolate to produce diphenyl sulfide and S^{2-} can be mechanistically described as a simple Lewis acid catalyzed nucleophilic aromatic substitution.^{93,94} The ratio of S^{2-} incorporation from the capping moieties is controlled by the reaction temperature and conditions. In a strongly passivating solvent, QDs can be formed instead of bulk materials due to kinetic trapping by ligand passivation.³⁷

For nanocrystals grown from $[Cd_{10}Se_4(SPh)_{16}]^{4-}$, the probability of S^{2-} incorporating into the growing nanocrystal with subsequent alloy formation therefore would not be surprising. The temperature of the reaction will dictate the percentage of phenylthiolate decomposition and subsequent S^{2-} content in the growing QD, while the depletion of available phenylthiolate will affect the continued incorporation into the growing quantum dot. The nature of the resultant alloy may be a homogeneous solid-solution (uniform or a gradient from core to surface),⁷⁰ a heterogeneous solid-solution,^{70,95} or a core-shell^{38,96} material (Figure 3.1).

Highly faceted, narrow size disparity CdSSe ($\pm < 7\%$ for 5.7 nm sample) were isolated from the single source cluster route in the size range from 1.5 – 5.7 nm, as measured by TEM, absorption, and pXRD (Figure 3.2). pXRD (Figure 3.2D) analysis indicate the CdSe and CdSSe QDs have wurtzite symmetry, while the CdS QDs are cubic. Control samples of pure CdSe and CdS were also isolated from single source clusters using the respective pure chalcogenide.

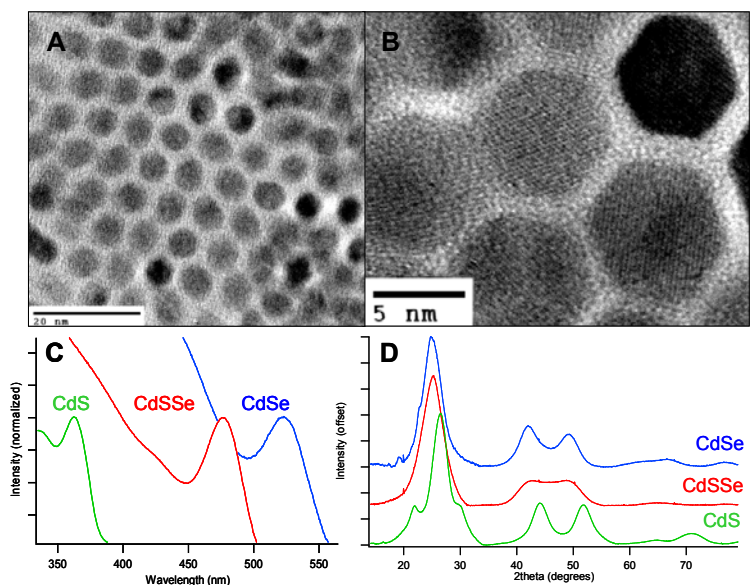


Figure 3.2: A) TEM image of 5.7 nm CdSSe QDs with a $S^{2-}:Se^{2-}$ ratio of 66:34 by XRF. B) HRTEM images of the same sample with visible lattice fringes. C) Absorption spectra of ~2.4 nm CdSe, CdSSe, and CdS QDs. CdSSe QD $S^{2-}:Se^{2-}$ is 36:64 by XRF. D) pXRD spectra of ~2.4 nm QD samples.

3.3.1 Elemental Distribution in the as-prepared CdSSe. In Table 1, the Se^{2-} concentration are shown for the series of isolated CdS_xSe_{1-x} QDs grown from the single source cluster $Li_4[Cd_{10}Se_4(SPh)_{16}]$, $Li_4[Cd_{10}S_4(SPh)_{16}]$, $Li_4[Cd_{10}Se_4(SePh)_{16}]$, CdSe passivated by TOP (CdSe-TOP) and CdSe ligand exchanged by thiophenol (CdSe-SPh). The CdSe-TOP and CdSe-SPh QDs were grown by a microwave synthesis using cadmium stearate. It is worth noting that the XRF cannot distinguish between S^{2-} incorporated into the lattice and SPh^- on the QD surface within the S^{2-} / Se^{2-} ratio and therefore cannot distinguish between CdSSe alloy and a CdSe/CdS core-shell motif. Although many micro-analytical techniques can be used to evaluate S^{2-} content, XRF is the most accurate for analyzing the S^{2-} to Se^{2-} ratios, as there are no complications from overlapping peaks as observed in XPS.^{97,98} (Figure 3.3)

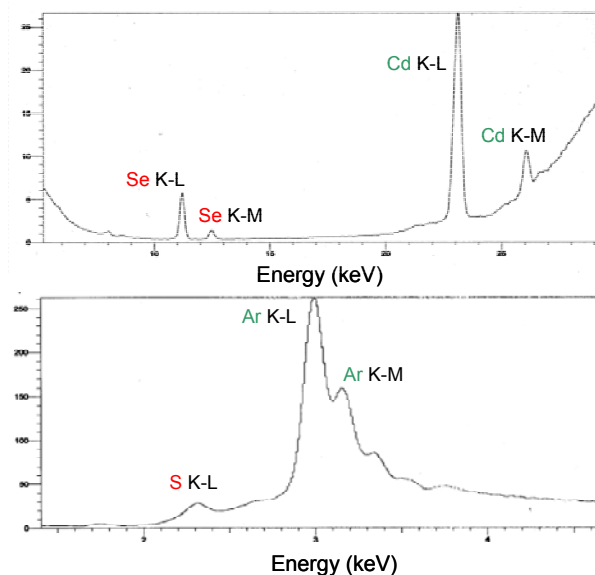


Figure 3.3: Sample XRF Spectra for CdSSe nanocrystals.

Inspection of Table 1 indicates that for the five individual reactions for formation of the CdSSe QDs (four at 230 °C and one at 120 °C), an increase in S^{2-} content is observed as the QDs increase in size up to ~ 3.5 nm, where the S^{2-}/Se^{2-} ratio asymptotes at $\sim 60\%$ sulfur. The S^{2-} content in CdSe-TOP (3.1 nm) is 0%. Upon ligand exchanging with thiophenol, the S^{2-} content for the 3.1 nm CdSe-SPh is 51%. The marked increase in S^{2-} implies a significant fraction may arise from contributions of phenylthiolate bound to the surface and S^{2-} incorporated into the QD. In all CdSSe samples in Table 1, a high concentration of S^{2-} is observed, although for reaction temperatures of 120 °C, the S^{2-} content is suppressed presumably due to the reduced thiophenolate decomposition at lowered reaction temperatures resulting in less S^{2-} available for incorporation.

Table 3.1: Experimental results for S²⁻/Se²⁻ composition, QD diameter by Scherrer broadening of <110> pXRD reflection, and exciton absorption (1s_e -1s_h). * is the % [Se]/([Se]+[S]) measured by XRF while ** is the % [Se] calculated by the effective mass approximation. Bracketed numbers are diameters verified by HRTEM. Highlighted samples are depicted in Figure 3.2. Reactions marked by † are synthesized via cadmium stearate microwave synthesis.

	XRF % [Se]*	Eff. Mass Approx. % [Se]**	Abs. λ (nm)	XRD (Scherrer) diameter (nm)
CdSSe	64	78	477	2.44
(230 °C)	69	76	502	2.93
	77	81	511	3.03
Growth 1	67	77	517	3.16
	58	77	522	3.26
	58	89	457	1.96
	75	90	489	2.32
Growth 2	85	87	498	2.56
	66	76	507	2.97
	60	74	516	3.26
	37	78	560	4.42
	36	78	567	4.71
	52	70	473	2.57
	60	77	488	2.64
	61	71	497	2.96
Growth 3	58	78	509	2.97
	55	77	514	3.10
	36	78	539	3.65
	35	81	548	3.81
	36	82	564	4.30
	39	73	567	5.13 [5.09]
	34	69	570	5.74 [5.78]
SSNMR	-	85	463	2.08
Growth 4	-	76	499	2.80
	-	68	505	3.23
	-	73	529	3.64
	-	74	546	4.06
	-	67	567	5.68
CdSSe	88	99	430	1.56
(120 °C)	77	81	450	2.05
	76	79	466	2.25
	74	84	486	2.40
CdSe	100	100	498	2.22
	100	100	519	2.46
	100	100	526	2.65
	100	100	532	2.77
CdSe-TOP[†]	100	100	544	3.10
CdSe-SPh[†]	49	100	544	3.10
CdS	0	0	352	2.41

To rationalize the S^{2-} content observed in the CdSSe alloys and CdSe-SPh sample, the presence or absence of phenylthiolates at the QD surface must be established. The presence of phenylthiolate bound to a QD surface will substantially modify the actual S^{2-} content measured in a QD sample resulting in a significant skewing of the XRF results, and thus an incorrect conclusion of the material motif.

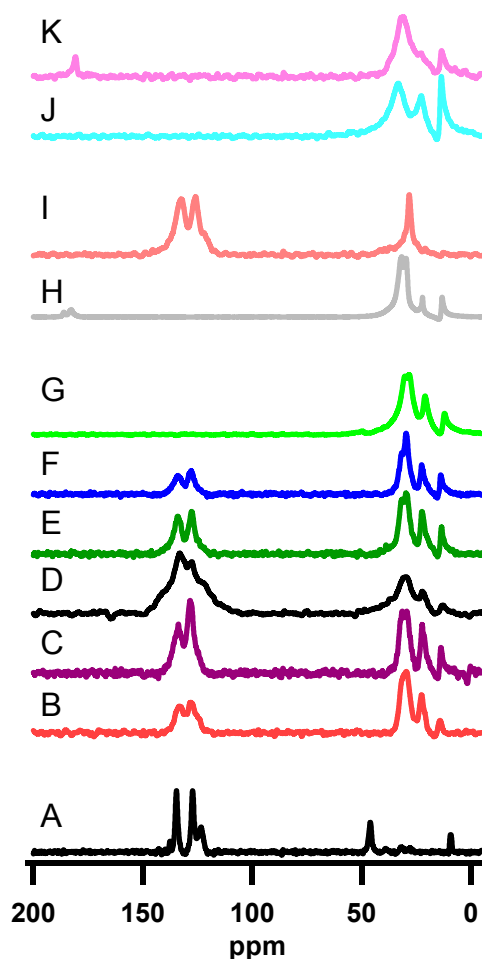


Figure 3.4: Solid State ^{13}C CP-MAS NMR of A) $\text{Li}_4[\text{Cd}_{10}\text{Se}_4(\text{SPh})_{16}]$ B) 2.1nm CdSSe C) 2.8nm CdSSe D) 3.2nm CdSSe E) 3.6nm CdSSe F) 4.1nm CdSSe G) 5.5nm CdSSe H) 3.1 nm CdSe grown from CdSA synthesis I) 3.1nm CdSe (CdSA grown) capped with thiophenol J) Tri-octylphosphine oxide K) Stearic Acid.

To analyze the surface of the prepared CdSSe and CdSe QDs, cross polarization magic angle spinning (CP-MAS) solid state NMR experiments were performed on one of the CdSSe growth reactions to help determine the nature of the ligands bound to the surface of the QDs. The CP-MAS data in Figure 3.4 shows the carbon signatures of the organic surface ligands for the aromatic resonances arising from SPh⁻, aliphatic signatures arising from TOPO, TOPSe, and stearic acid, and the –COOH signature from stearic acid. The aromatic resonances of Li₄[Cd₁₀Se₄(SPh)₁₆] (Figure 3.4A) can be assigned as 137.49 ppm (alpha), 134.57 ppm (ortho), 127.17 ppm (meta), and 123.32 ppm (para) and the signatures at 9 and 46 ppm can be assigned to impurities from triethylamine. The CdSSe grown from Li₄[Cd₁₀Se₄(SPh)₁₆] (Figure 3.4B-G) are consistent with the assignments for thiophenol bound to the QD surface. The aliphatic signatures for the CdSSe cluster are observed between 10-40 ppm, and can be assigned as contributions arising from TOPO, consistent with the observed resonances for TOPO in Figure 3.4J. For the 3.2 nm CdSSe QD (Figure 3.4D), the linewidth appears to increase dramatically which may arise from chemical shift anisotropy between different sites on the CdSSe QD surface. This conclusion is reasonable as the highest phenylthiolate concentration relative to TOPO is observed at this size.

NMR assignments for the CdSe-TOP QD (3.1 nm) grown from CdSA (Figure 3.4H) show contributions from the –COOH feature (180 ppm), assignable to stearic acid (Figure 3.4K). In addition, the aliphatic region consists of contributions from stearic acid and TOP in the 10-40 ppm range. CdSe-TOP QD was ligand exchanged with thiophenol which results in complete loss of the stearic acid signature (180 ppm) and the predominant aliphatic contributions (10-40 ppm). In the aromatic region the signature for thiophenol is clearly present (Figure 3.4I) for CdSe-SPh.

Integrations of the aromatic and aliphatic regions of Figure 3.4B-G reveal the relative ratio of ligands bound to the surface of the QD as it grows from 2.1 – 5.7 nm. Using these ratios the number of SPh⁻ and TOPO ligands were determined and plotted in Figure 3.5. The loss of the resonance for thiophenol (Figure 3.4G) for the 5.7 nm QD was confirmed on replicate measurements on QD samples between 5 and 5.7 nm in size. The concentration of thiophenol to aliphatic can be evaluated semi-quantitatively using ¹³C CP-MAS NMR signals.

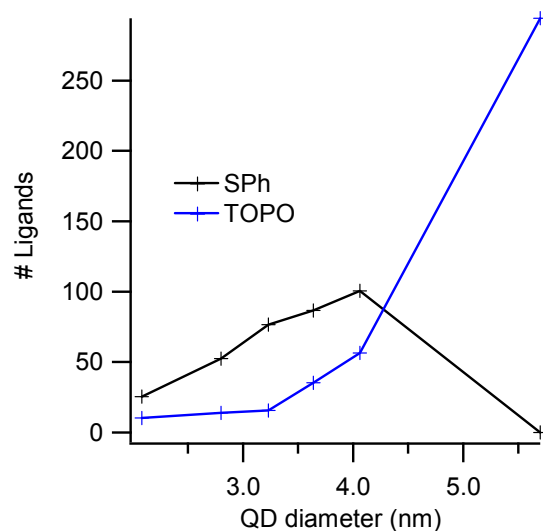


Figure 3.5: Number of ligands bound to CdSSe QDs plotted vs. QD diameter. Percent of ligands were determined semi-quantitatively by ^{13}C CP-MAS NMR.

^{13}C CP-MAS experiments were chosen over ^{13}C MAS to determine the relative ratio of SPh : TOPO due to the improvement in signal to noise, faster experiment collection times, and ^{13}C and ^1H are only present as surface ligands therefore the cross polarization should have a minimal effect on signal intensity. To ensure that signal intensities were not affected and T_1 relaxation was allowed to fully recover, a series of MAS experiments were performed where the recycle delay was varied (3, 6, 10, 20 sec) and the optimum recycle delay was determined to be 10 sec. A comparison was made between the intensity ratios for the CP-MAS and MAS experiments to validate that the CP-MAS experiment did not skew the reported ratios. Assuming the alkane passivant is predominately TOPO, the relative ratio from the MAS experiment was 1 TOPO : 6 SPh, while the CP-MAS had a ratio of 1 : 5.8. Although the T_1 for the ^{13}C signal was not measured, the agreement in CP-MAS and MAS measurements at 10 and 20 sec delay suggest the analysis is fairly accurate. Build up curves were also performed to ensure $T_{1-\text{Rho}}$ was not compromised and the ^{13}C signal was allowed to fully recover (Figure 3.6).

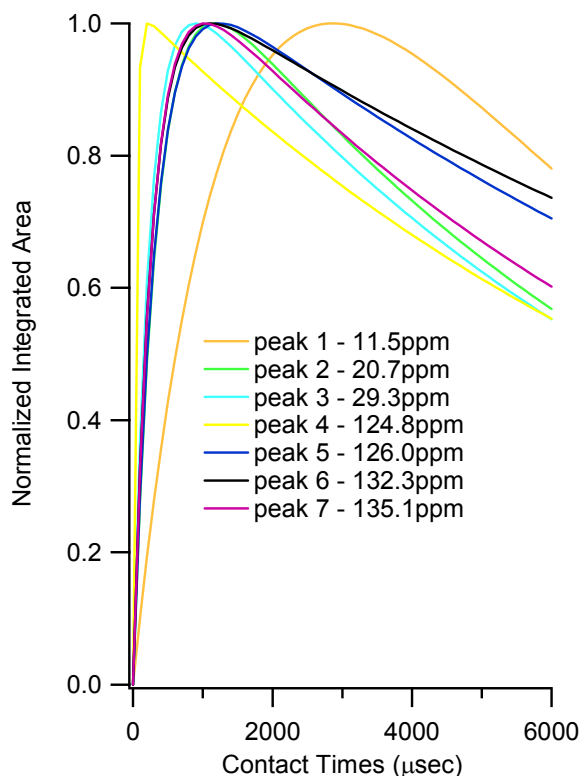


Figure 3.6: ^{13}C CP-MAS build up curve on 3.6nm CdSSe. Individual peaks were fit to 4 aromatic and 3 aliphatic signatures. Each individual build up curve was normalized for ease of viewing. All profiles have similar build up except peak 1 (methyl carbon on TOPO) and peak 4 (para carbon on SPh^-). Contact times used were 0.5, 1.0, 1.6, 2.0, 2.5, 5.0 ms.

The plot of the number of ligands versus size is intriguing, as it suggests the phenylthiolate content increases with increasing size up to at 4 nm, and then decreases as the QD continues to grow. Ligand exchange by TOPO, pyridine or HDA does not modify the observed phenylthiolate concentration ratio in these materials. This observation is consistent with our earlier publication⁴⁰ where the phenylthiolate was observed to be remarkable robust on the QD surface, exhibiting a lack of exchange by pyridine at 70 °C or TOPO at 80 °C.

The difference in the phenylthiolate concentration between small (3.5 nm) and large (5.7 nm) CdSSe samples is further evidenced by analyzing TGA data for these materials. TGA on a 3.5 nm CdSSe and 5.7 nm CdSSe exhibit marked differences for

ligand loss at 600 °C. The mass loss at 600 °C is assignable to thermal degradation of two SPh⁻ ligands with production of a free S²⁻ and diphenylsulfide, as observed in the earlier TGA studies by Wang and Herron.⁸⁷ The smaller QD shows significant loss of S²⁻ associated with ligand loss at 600 °C (42% → 21%), while the 5.7 nm QD shows insignificant changes in S²⁻ (66% → 63%) when heated to 600°C. The lower loss for S²⁻ corroborates the lack of SPh⁻ on the QD surfaces as observed in the NMR data.

The NMR data and TGA analysis conclusively show that SPh⁻ is present in these materials for sizes below 5 nm and is a contributor to the observed S²⁻ in XRF. It is important therefore to note that the total S²⁻ content reported in Table 1 will be artificially high, however the observation of ~60% S²⁻ content above 3.5 nm where SPh⁻ coverage is dropping cannot be attributed solely to SPh⁻, particularly for the 5.5 nm QD where no SPh⁻ is experimentally observed. Although a core-shell motif could explain this observation, our ⁷⁷Se NMR CP-MAS data at short contact times from earlier studies clearly demonstrate Se²⁻ at the surface by ¹H-⁷⁷Se CP-MAS experiments.⁴⁰ This result has been confirmed for all sizes in this study (unpublished result), and is currently being analyzed. To properly project the CdSSe composition and thus the elemental distribution, the quantity and characteristics of SPh⁻ at the QD surface must be better understood and analyzed.

3.3.2 Nature of the CdSSe alloy. While the presence of SPh⁻ on the QD surface could rule out a simple core-shell motif to explain the S²⁻ enrichment, it does not rule out S²⁻ ion incorporation into the growing QD. The actual nature of the alloy formed during the reaction, whether a homogeneous or inhomogeneous alloy is still unknown (Figure 3.1). Insight into the nature of the alloy may be gained by considering the impact of formation of a solid solution on the electronic properties of the semiconductor QD using an effective mass approximation (EMA) to account for the tuning of the semiconductor band gap by the alloying of the ternary ion. The change in the exciton absorption as a function of size and composition can be generated by use of the theoretical model described by Rosenthal, et al⁷⁰ for CdSSe QD homogeneous alloys. By applying the size dependent confinement formula of the EMA (Eq. 2) and utilizing known energy shifts for pure cluster grown samples,⁹⁹ an expression can be generated for the shift in the exciton as a function of elemental composition,

$$E_g(x,d) = x \left[E_g(\text{CdS}, \infty) + \frac{a_1}{d} + \frac{c_1}{d^2} \right] + (1-x) \left[E_g(\text{CdSe}, \infty) + \frac{a_2}{d} + \frac{c_2}{d^2} \right] - b(d)x(1-x) \quad (2)$$

where a and c represent the reduced mass of the e^- and h^+ , (fit as empirical parameters), d is the QD diameter, and b is the bowing constant describing the nonlinear effects of ion doping.

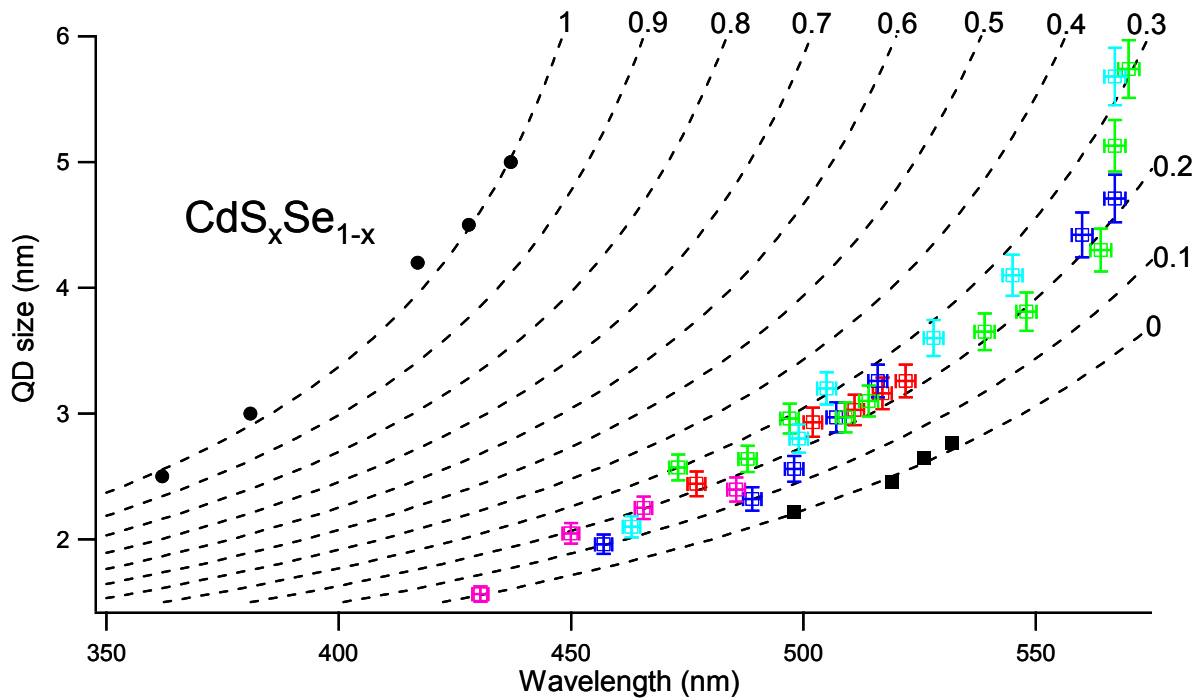


Figure 3.7: Five separate CdS_xSe_{1-x} QD reactions grown from Li₄[Cd₁₀Se₄(SPh)₁₆]. Sizes measured by pXRD Scherrer-Debye analysis and calibrated by HRTEM. Dashed lines are theoretical effective mass approximation of the indicated concentrations of S:Se. Squares are pure CdSe QD samples. Circles are pure CdS QD samples from Ref. 43

Figure 3.7 shows the change in the energy for the first exciton absorption for the five individual reactions for CdS_xSe_{1-x} QDs. The experimental data is overlaid with theoretical plots calculated by the EMA. Inspection of the absorption value for the

exciton versus the measured size shows there is a shift in the energy gap when compared to pure CdSe or CdS QDs of the same size. The first excitonic transition exhibits a blue-shift of 41 nm for a QD of the same size (Figure 3.2C). The core-shell motif, where CdSe and CdS phases are completely segregated, does induce a shift in the absorption edge, but has a much weaker (~8 times less) effect at low dopant concentrations.^{70,96} The observed shift in the first exciton transition of CdSSe relative to CdS and CdSe QDs provides direct and conclusive evidence of S²⁻ incorporation into the lattice. Although the effective mass equation is an approximation for describing the QD absorption properties, the experimental plots support a homogeneous alloy formation. The details of the alloy whether uniform or a gradient from core to surface is not defined by the absorption data alone, and only the correlation of all the experiments can provide a map of the formed alloy.

3.3.3 Qualitative model of the QD. Using a model for the alloy growth based upon the initial observations of Wang and Herron⁸⁷ for growth of CdS from Li₄[Cd₁₀S₄(SPh)₁₆], one might suspect the final composition of a QD grown from Li₄[Cd₁₀Se₄(SPh)₁₆] to exhibit a ratio containing 60% S²⁻ and 40% Se²⁻. This can be deduced based on stoichiometry, where the composition is 10 Cd : 4 Se²⁻ : 6 S²⁻ (from SPh⁻) and the remaining products consist of 6 (Ph)₂S, and 4 Li-SPh. The actual stoichiometry will be further enriched in S²⁻ arising if the remnant four Li-SPh further decompose at the QD surface. The additional S²⁻ generated by this decomposition would result in a 66% ratio of S²⁻ arising from the phenylthiolate decomposition, and a ratio of ~ 1: 1.2 Cd:chalcogenide. While decomposition of phenylthiolate is critical, this is a temperature dependent reaction and at the initial reaction temperatures, crystallization theory² should dominate, with a pure nuclei forming first. As the temperature of the reaction increase, phenylthiolate decomposition will increase roughly proportional to the available surface area above a critical temperature leading to what one might suspect will be an enrichment of S²⁻ approaching the 60% reaction stoichiometry of the cluster. In the growth of CdSSe QDs from [Cd₁₀Se₄(SPh)₁₆]⁴⁻, the reaction will be complex dominated by the decomposition mechanism, which is temperature dependent; the concentration of surface bound phenylthiolate, and the rate of S²⁻ incorporation versus

Se²⁻ incorporation since the rate of atom addition is dictated by the reactivity of the QD surface.

Evidence of the model can be generated by inspection of the Cd:chalcogenide ratio for the QDs from XRF compared to the change in the S²⁻ content estimated by EMA. Measuring the S²⁻ content by EMA and XRF provide insight into the average composition relative to the total S²⁻ composition as a function of the QD size. The Cd:chalcogenide ratio is approximately 1:1.1 (Cd:S+Se) across all samples indicative of an anion rich surface. A plot of the percentage [Se] and [S] extracted by the EMA and by XRF versus size for the growth reactions are combined and shown in Figure 3.8A and B. The S²⁻ content calculated from the EMA, which correlates with band gap tuning arising from alloying; exhibits a slow increase (22 - 31%) with increasing QD size (3.65 - 5.9 nm). The exception is the 1.5 nm QD where only 1% S²⁻ incorporation is observed. An intriguing observation worth noting in Figure 3.8A is the observation in the effective mass approximation that the 1.5 nm CdSSe QD is only 1% sulfur, which is accounted for by incorporating the thiophenol content observed in Figure 3.5. The observation of insignificant S²⁻ incorporation in this size regime is indicative of a pure nucleus as predicted by nucleation theory. Efforts by Gamelin, et al have pointed towards the critical nuclei for CdSe to be roughly 1-2 nm in size, in agreement with our observation.²

The change in S²⁻ content for the XRF data is more dramatic. At sizes below 3.2 nm, the S²⁻ content is varied with a composition of 15- 40%. Above 3.2 nm, the S²⁻ content exhibits a discontinuity with values of ~60% S²⁻. The XRF data is influenced significantly at small sizes by surface contributions from bound phenylthiolate based purely upon surface to core ratios for the QDs. As the QD grows the surface contribution to total S²⁻ content will become less significant. The marked increase for S²⁻ in the XRF above 3.2 nm, but no significant jump in the EMA data implies increased phenylthiolate decomposition is occurring at the QD surface, resulting in increased S²⁻ content. Coupling this result with the stoichiometric expectations for the QD growth from a cluster, the ratio of 60% incorporation is consistent.

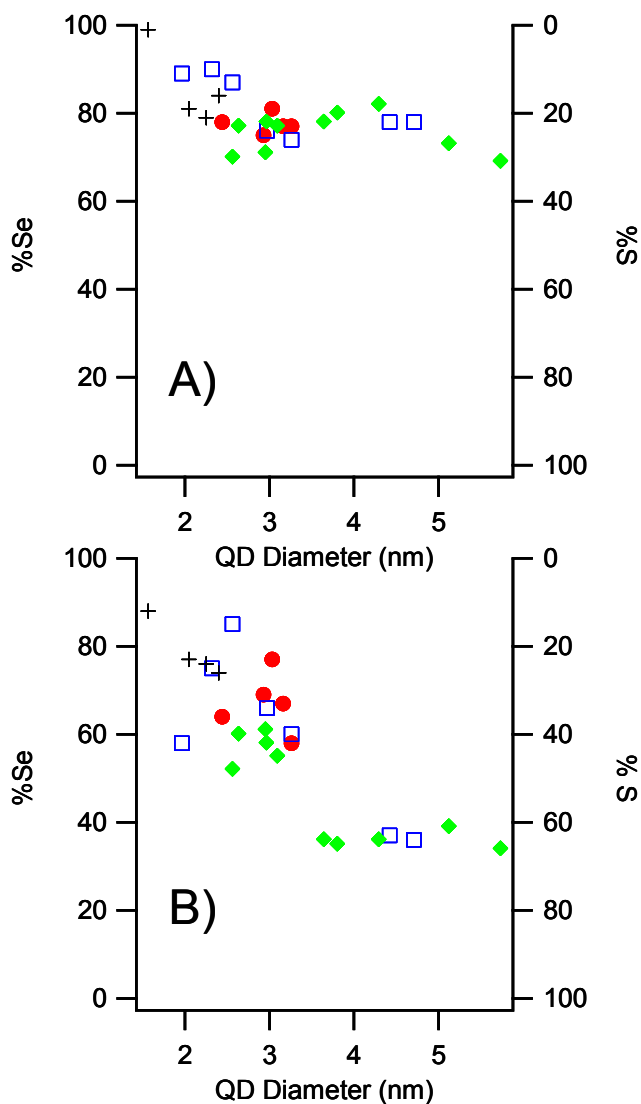


Figure 3.8: A) CdSSe concentrations calculated by the effective mass approximation plotted against QD size B) CdSSe concentrations calculated by XRF plotted against QD size.

To evaluate the jump in S^{2-} arising from increased phenylthiolate decomposition, Figure 3.5 and 3.8 are compared. In Figure 3.5, the NMR data, which tracks phenylthiolate and alkane ligands at the surface of the QD, shows a maximum phenylthiolate content at ~ 4 nm and drops to non-measurable levels above 5 nm for CdSSe QDs. If we consider the fact that the sulfur incorporation is a complex issue of temperature, and the available surface area of the QD for phenylthiolate decomposition,

the decrease in phenylthiolate in the NMR below 4 nm can be accounted for by enhanced phenylthiolate decomposition resulting in S^{2-} incorporation. The assumption that S^{2-} incorporation is influenced by reaction temperature is clearly seen in Table 1, where lower sulfur content is observed for reactions carried out at lowered reaction temperatures (120 °C). The nearly invariant composition in the EMA coupled to the stepped increase in XRF reflects the gradient nature of the alloy due to the complex reaction pathway for QD growth from clusters coupled to contributions from enhanced decomposition rates and potentially changes in surface energy of the growing QD. The loss of phenylthiolate from the QD surface and increased S^{2-} content at the largest sizes, can be supported by the broadening of the absorption feature for the first exciton (Figure 3.9). The broadening of the absorption feature is partially due to a loss of distribution as shown in TEM image (~7%), but is also likely due to the apparent discontinuity in the S incorporation in these sizes.

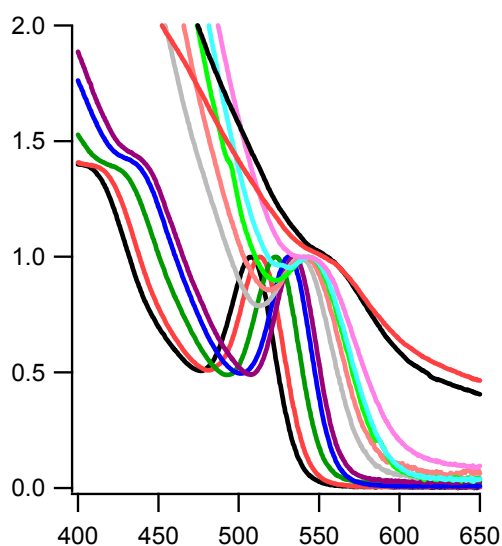


Figure 3.9: Absorbance profile of growing CdSSe from $Li_4[Cd_{10}Se_4(SPh)_{16}]$. Above ~550nm further growth is possible by growth by decomposition of SPh^- surface ligands leading to lose of first exciton and size distribution.

The conclusion that S^{2-} is incorporated into the growing alloy for QDs below 5 nm, a 3.26 nm CdSSe QD was analyzed for S^{2-} content during growth and subsequent etching with a II-VI acid etchant ($H_3PO_4:HCl$). A similar approach to etching has been carried out by Peng, et al.¹⁰⁰ In Figure 3.10 the experimental data shows that the S^{2-} content in both the growing and etched QD nearly track perfectly for removal of a single shell from the QD, and is observed to reproduce the ion content at the smallest size. The lack of agreement is consistent with the probability that etching is not uniform for all faces. The remarkable observation is the rapid decrease in S^{2-} content for the first shell removal.

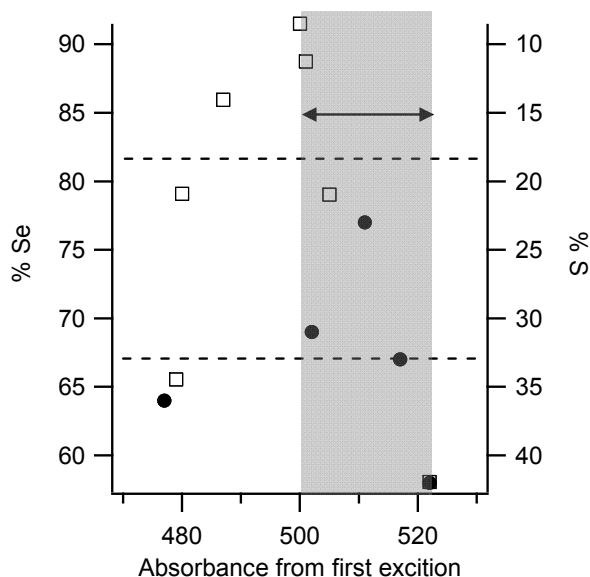


Figure 3.10: The %Se (and %S) from XRF analysis from a 3.26 nm CdSSe QD taking during growth (circles) and then subsequent acid etching (squares) by H_3PO_4/HCl (50% v:v). The shaded area represents removal of ~ 0.4 nm, approximately one lattice plane.

Comparing this observation to the NMR data, which indicates the presence of phenylthiolate, allows the conclusion that the high S^{2-} content is due primarily to the presence of phenylthiolate and not core shelling. Removal of approximately two shells

from the QD yield a value for S^{2-} consistent between the grown and etched sample by XRF. The remarkable correlation between the etching experiment (Figure 3.10), the Se^{2-} concentration as a function of size measured by the EMA (Figure 3.8A), the increased S^{2-} incorporation reflected in NMR and XRF (Figure 3.5 and 3.8B) supports the conclusion that an alloy is formed in the reaction and phenylthiolate is the major contributor of the apparently high S^{2-} concentration.

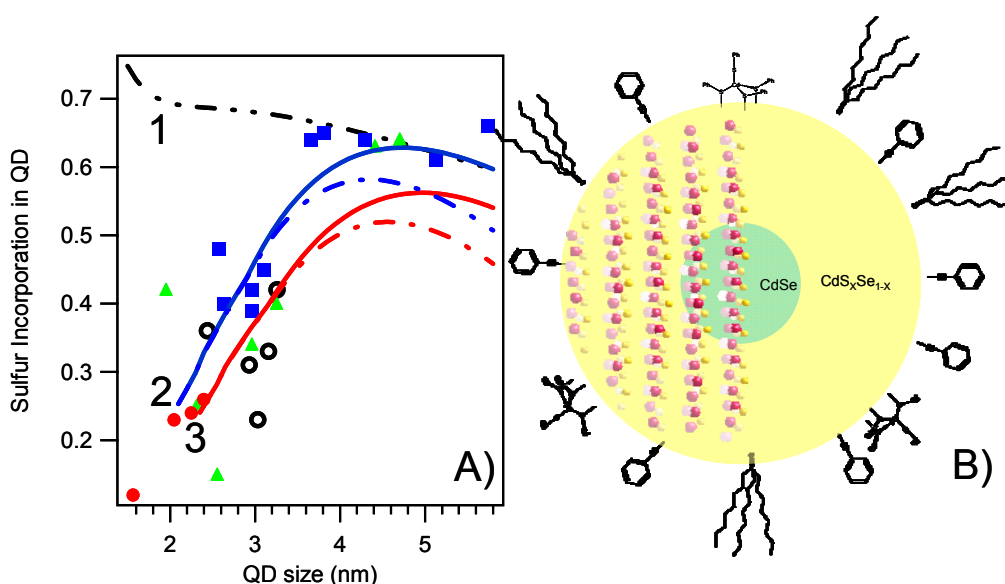


Figure 3.11: A) Sulfur incorporation vs. QD size. Line 1 depicts growth of a uniform 60S/40Se alloy. Line 2 depicts growth of a 2 nm pure CdSe core with 70S/30Se (solid) 60S/40Se (dashed). Line 3 depicts growth of a 2.25 nm pure CdSe core with 70S/30Se (solid) 60S/40Se (dashed). Other points are experimental growth reactions determined by XRF. B) Model of CdSSe QD, showing crystal structure of a CdSSe QD with organic ligands passivating the surface. CdSSe QD cross-section is cut on the $\langle 110 \rangle$. Model depicts pure CdSe nucleus with CdSSe alloy.

3.4 Conclusion

The nature and ion distribution within the CdSSe QD alloy requires a model that can account for the experimentally derived S^{2-} composition by XRF (Figure 3.8), the

postulation of a pure core (~1.5 – 2nm), and the S²⁻ contributions arising from surface bound phenylthiolate contributions, as observed in Figure 3.5. In Figure 3.11, a plot of the fractional S²⁻ composition as a function of QD size is shown. The experimental XRF data from four separate reactions is plotted. Assuming the cluster stoichiometry of 60% S²⁻ arising from phenylthiolate decomposition and contributions from bound phenylthiolate based on the NMR results yields the black line (Line 1). Although the agreement is reasonable for QD > 4 nm, the lack of agreement with experimental data below 4 nm in size suggests the QD is not a uniform alloy. Incorporating a pure CdSe nuclei as suggested by nucleation theory, yields Line 2 and 3 (blue and red), where a 2 nm (blue) and 2.25 nm (red) pure CdSe core is assumed and subsequent 60:40 (dashed) and 70:30 (solid) S²⁻ to Se²⁻ incorporation arises as the QD grows. Inclusion of a pure core gives surprisingly good agreement with the experimental data for a 2 nm core with an alloy at 70:30 S²⁻: Se²⁻. The theoretical plots were generated by predicting the number of atoms based on sizes and number of SPh⁻ based on ¹³C CP-MAS NMR. A number of assumptions are made in the generation of these plots such as uniform growth, no defect sites, and 100% surface passivation by ligands based on available binding sites.

Although the data below 4 nm is scattered, suggesting a rather complex reaction, the agreement suggests a model where a pure nuclei is generated and S²⁻ addition reaches equilibrium above 4 nm (Figure 3.11B). The complexity of the reaction arises from the different rates of S²⁻ production from SPh⁻ decomposition, increase in reaction temperature and rate of S²⁻ incorporation in the growing QD. It is believed the S²⁻ incorporation rate becomes more uniform as the observed phenylthiolate concentration bound to the QD drops, presumably reflecting near-instantaneous degradation upon phenylthiolate adsorption on the QD surface.

Taking the complete data set, a model (Figure 3.11) can be proposed for the CdSSe alloy grown from the molecular cluster. At the core, a pure CdSe nuclei of ~1.5 nm exists with phenylthiolate bound to the QD surface. As the particle grows, the reaction temperature, surface area and phenylthiolate decomposition rate increase, likewise the level of S²⁻ alloying increases. At the largest sizes, loss of phenylthiolate, verified from the CP-MAS, but continued incorporation of S²⁻ is observed supporting the

increased decomposition rate and implying that a constant S^{2-} rate should be observed reflecting anion availability and the thermodynamics of the reaction. The rate of incorporation approaches the stoichiometric value by XRF, and exhibits an increasing alloy composition by EMA. The slow increase in EMA reflects the slow rate of alloying formation in the core of the QD relative to the outer most shells.

The data supports a model where the Se^{2-} is not restricted to the core and the S^{2-} to the surface, as expected for a core-shell, but rather represents a solid solution whose composition is controlled by thermodynamic parameters, namely S^{2-} concentration, energetics of S^{2-} versus Se^{2-} addition to a growing QD, and the conversion from a kinetically controlled reaction to a thermodynamically equilibrated process. It is not surprising that the compositional distribution of the S^{2-} in the CdSSe QDs approaches the stoichiometric value of 60% but the mechanism is quite complex if one considers the implications of nucleation theory and the influence of the precursor concentrations on the kinetics as the reaction progresses since the available reactant concentrations (S^{2-} vs. Se^{2-} vs. Cd^{2+}) are in constant flux.

CHAPTER FOUR

SIZE AND SITE DEPENDENT RECONSTRUCTION IN CDSE QDS EVIDENCED BY $^{77}\text{SE}\{^1\text{H}\}$ CP-MAS NMR SPECTROSCOPY

*Reproduced with permission from Journal of the American Chemical Society.
Copyright 2010 American Chemical Society.*

4.1 Introduction

Semiconductor quantum dots (QDs), which are widely studied by optical spectroscopy, exhibit unique size-dependent properties that can be strongly influenced by reconstruction at the surface or in the core of the QD.^{42,101-104} The exact nature of the reconstruction and the impact of surface ligation on reconstruction in a QD as a function of size are still controversial. Theoretical studies^{105,106} on CdSe QDs have suggested reconstruction should occur in these materials due to surface strain. Analysis of the average QD structural environment by X-ray diffraction,¹⁰⁷ EXAFS/XANES,¹⁰⁸ and Rutherford back scattering^{109,110} imply that overall QDs only experience minimal reconstruction that anneals out as the QD grows. More advanced studies have suggested a better model may require the inclusion of discrete sites (surface vs. core) and a size dependent behavior to fully interpret the impact of reconstruction in a QD.^{106,111-119} A series of advanced studies on CdSe QDs using pair-distribution function analysis of X-ray data has probed the question of reconstruction to a greater degree and suggests reconstruction is localized at the nanocrystal surface, while the core of the nanocrystal is largely unperturbed.^{111,112,114} Recent studies of the size dependent elastic properties¹¹³ have confirmed these findings but indicate CdSe below 3 nm exhibits a strongly perturbed structure potentially due to a change in the nature of reconstruction in the QD. Size dependent analysis of CdSe QDs by pressure dependent Raman measurements has also observed a change in the Grüneisen parameter for CdSe QDs below 3 nm.^{77,120} While these techniques have provided insight into the overall changes in the structure as a function of size, the use of an analytical technique that is selective for select elements within the lattice and specific to

the location of these elemental sites would be ideal to address the nature of bonding and reconstruction experienced by a QD.

Due to the element specificity inherent to nuclear magnetic resonance (NMR) methods, ease of synthesis and well studied properties for CdSe,^{121,122} this study analyzes the size dependent reconstruction on ⁷⁷Se enriched CdSe QDs (Cd⁷⁷Se) using NMR methods to structurally depth profile specific ⁷⁷Se atoms in local chemical environments. Solid-state NMR studies of Cd⁷⁷Se QDs, ranging in size from 2 – 7 nm, with a 5 - 6% size dispersity are analyzed allowing discrete assignment of the core, surface and passivant ⁷⁷Se sites within the QD, as well as evidence of size dependent QD reconstruction. Of the NMR active species in a CdSe QD (¹¹³Cd, ⁷⁷Se, ¹³C, ³¹P, and ¹H),^{40,41,43,102,104,123-127} the ⁷⁷Se atom (spin = 1/2) is convenient to study because of the environmental sensitivity of its chemical shift⁴⁰ and the ability to isotopically enrich the element. For the Cd⁷⁷Se QD samples, the NMR chemical shifts as functions of size reveal that the ligation layer is unique and apparently uncoupled to QD size effects, while the surface (outer most shells) and core (inner most shells) environments exhibit different magnitudes of reconstruction depending on the size of the QD. As the QD grows, reconstruction appears to be more localized to surface layers while the core appears to be largely unperturbed. Since semiconductor QDs and more importantly CdSe are being applied in a diverse range of technologies, understanding the structural attributes of reconstruction and the impact on the outermost planes relative to the core of the QD is crucial.

NMR methods can allow the differentiation of discrete chemical environments within a QD by analyzing the chemical shift of the elemental sites and discriminating the elemental signal associated with a surface versus a core of a QD.^{40-43,101,102,104,126-139} Cross-polarization magic angle spinning (CP-MAS) can allow the surface versus core signals to be delineated, since CP enhancement is a heteronuclear short range process^{40,41,43,133} dependent on numbers of nuclei, relative geometries, and the Hartmann-Hahn matching condition.^{40,42,129,140,141} Spin-echo measurements allow a more global analysis of the lattice properties and by coupling spin-echo and CP experiments, it is possible to delineate the NMR contributions from the surface and sub-layers in the QD. Although there could be multiple ¹H populations influencing the CP

signals (which are face, site, and passivant density specific), the passivant ^1H nuclei nearest the surface layer will dominate the polarization transfer process. Carr Purcell Meiboom Gill (CPMG) NMR acquisitions increase NMR sensitivity for these samples without significant distortion of the ^{77}Se line shape, allowing ^{77}Se T_1 (spin-lattice) and T_2 (spin-spin) relaxation measurements for the QD. Interpretation of the NMR data is a powerful analytical tool for structural analysis in QDs but is limited by the broadening of NMR features due to disorder and spin-spin interactions in nanoscale materials with high surface-to-core ratios.^{40,139}

Isotopic enrichment of the Se sites enhances spin diffusivities, facilitating assignment of ^{77}Se signals to different layers within the QD through analysis of the variable CP contact times. NMR chemical shifts as functions of size reveal that the ligation layer is unique and apparently uncoupled to QD size effects, while the surface (outer most shells) and core (inner most shells) environments exhibit different magnitudes of reconstruction depending on the size of the QD. Based on chemical shift analysis as a function of CP times, global reconstruction is observed for QDs below 3 nm while the reconstruction appears to be self-limited for QDs greater than 3 nm. As the QD change size, reconstruction appears to be more localized to surface layers while the core appears to be largely unperturbed. Surface reconstruction appears to influence the effectiveness of spin diffusion between QD surface and core regions, which could have implications to NMR studies across semiconductor nanostructure interfaces.^{142,143} The T_1 and T_2 results show a discontinuity around 4 nm which may imply the largest change in reconstruction occurs in this size regime. Analysis of the chemical shifts using the Ramsey expression coupled to valence bond theory provides insight into the changes in local bonding that occur with size and indicates the surface sites have greater s-character for the Cd - Se bonds due to compressive strain. The change in bonding is consistent with the expectation for passivant chelation and surface dangling bonds in a QD. The NMR based model for Cd^{77}Se reconstruction supports the findings of Billinge, *et. al.*¹¹⁴ and Scholes, *et. al.*,¹¹³ who postulate size dependent reconstruction.

4.2 Experimental

4.2.1 Chemicals. Cadmium stearate (CdSA) (90%, Strem Chemical), 1-Octadecene (ODE) (90%, Sigma Aldrich), Selenium powder, (99.66% enriched ^{77}Se , Isoflex USA), and Tri-n-octylphosphine (TOP) (90%, Alfa Aesar) were used without further purification.

4.2.2 Synthesis of Cd^{77}Se QDs from Cadmium Stearate (CdSA). Cd^{77}Se QDs were grown by lyothermal methods using a modified literature reaction involving CdSA and TOP- ^{77}Se .²³ CdSA was added to 1-octadecene in a 3-neck round bottom flask under N_2 and degassed according to the literature procedures. The reaction mixture was heated, TOP- ^{77}Se was injected, and allowed to stir until the target QD size was obtained; size was monitored by UV-Vis absorption of aliquots. The reaction temperatures used were 180, (3.1 nm) 280, (4.32 nm) and 300 °C (6.1 and 6.9 nm) for each targeted QD size. The reaction was allowed to cool to room temperature and the QD isolated by centrifugation through standard selective precipitation methods via the addition of n-butanol to the reaction mixture followed by toluene/methanol dissolution/precipitation steps. The samples were dried under vacuum at room temperature and the solid powdered samples packed into 2.5 mm zirconia Varian NMR rotors.

4.2.3 Synthesis of Cd^{77}Se QD from $\text{Li}_4[\text{Cd}_{10}^{77}\text{Se}_4(\text{SePh})_{16}]$. For comparison a Cd^{77}Se QD lacking an ^{77}Se enriched passivant layer was prepared as the smallest QD (2.9 nm) via a single source precursor route¹⁴⁴ using $\text{Li}_4[\text{Cd}_{10}^{77}\text{Se}_4(\text{SePh})_{16}]$ grown in the presence of hexadecylamine at 230°C. The actual enrichment level of the core and surface of the 2.9 nm QD will be less than 100%, as it is known that selenophenol (SePh) will decompose during the reaction and act as a Se donor atom during QD growth.^{38,144} Thus, the passivant layer will consist of a SePh (un-enriched Se) and TOP/TOPO following ligand exchange. Once the reaction was at the desired size, the reaction was allowed to cool to room temperature and the QD isolated by centrifugation through standard selective precipitation methods using toluene/methanol dissolution/precipitation steps. The sample was dried under vacuum at room temperature and the solid powdered sample packed into 2.5 mm zirconia Varian NMR rotors.

4.2.4 Solid State Nuclear Magnetic Resonance. All solid state NMR experiments were performed on a Varian Unity / Inova 11.75 T spectrometer with a Chemagnetics triple-resonance 2.5-mm broadband Magic Angle Spinning (MAS) probe using zirconia rotors. The probe was tuned to: 500.1 MHz for ^1H and 95.36 MHz for ^{77}Se ; the third channel was not used in this study. An MAS speed of 12 kHz was used in all experiments, (except some ^1H $T_{1\rho\text{H}}$ experiments conducted at 24 kHz MAS). The ^{77}Se chemical shifts were determined relative to an external reference standard of dimethyl selenide, $\text{Se}(\text{CH}_3)_2$, at 0 ppm. Multiple ^{77}Se experiments were run on the samples including $^{77}\text{Se}\{^1\text{H}\}$ CP-MAS, ^{77}Se spin-echo, and ^{77}Se saturation recovery – CPMG.

4.2.4a CP-MAS: $^{77}\text{Se}\{^1\text{H}\}$ CP-MAS spectra were acquired using ^1H decoupling, ramped cross-polarization (CP), an acquisition time of 5 ms, a recycling delay of 3 s, and a 90° pulse length of 5 μs . The contact time was varied (1 – 40 ms) allowing different polarization transfer times between the ^1H and ^{77}Se nuclei. Least squared fits of CP-MAS NMR spectra to multiple Gaussian line shape components were accomplished in Mathematica. During the initial fitting the amplitude, FWHM, and chemical shift position were allowed to float on the 12 or 15 ms contact time point. This time point was chosen because contributions for the core and surface were readily observable. Once the fundamental resonances were identified the other time points were fit keeping the FWHM and chemical shift position constant and allowing only the amplitude to be varied. CP-MAS buildup data were constructed from integrated area verses contact time and fit to the following equation,

$$M(\tau) = \frac{M_0 \left[\exp\left(\frac{-\tau}{T_{1\rho\text{H}}^*}\right) - \exp\left(\frac{-\tau}{T_{\text{HSe}}^*}\right) \right]}{1 - \frac{T_{\text{HSe}}^*}{T_{1\rho\text{H}}^*}} \quad (1)$$

The validity of assumptions underlining the derivation of Eq. 1 are discussed later in the text.

4.2.4b Spin-echo: ^{77}Se spin-echo spectra were performed with an acquisition time of 1.5 ms, a recycling delay of 180 s, and a 90° and 180° pulse length of 3.25 and 6.50 μs , respectively. Least squared fits for the spin echo NMR spectra were accomplished in Mathematica with total number of peaks for each spectrum kept to a minimum. Spin

echo pulse methods were chosen to measure the overall Se environments in the QDs in order to avoid loss of signal to noise due to ring-down.

4.2.4c Saturation Recovery – CPMG: ^{77}Se spin lattice relaxation (T_1) times and spin-spin relaxation (T_2) times were determined by using a saturation recovery – CPMG pulse sequence. The parameters used for these experiments include a recycle delay of 1 s, a 90° and 180° pulse length of 3.25 and 6.5 μs , 20 saturation 90° pulses (N_{Sat}) separated by 50 μs , 1000 echo pulses (N_{Echo}) separated by 1 ms. Delay between saturation and acquisition was varied from 0.1 ms - 4320 s depending on the sample. Saturation recovery – CPMG pulse sequence used to measure spin relaxation times is as follows (Figure 4.1).

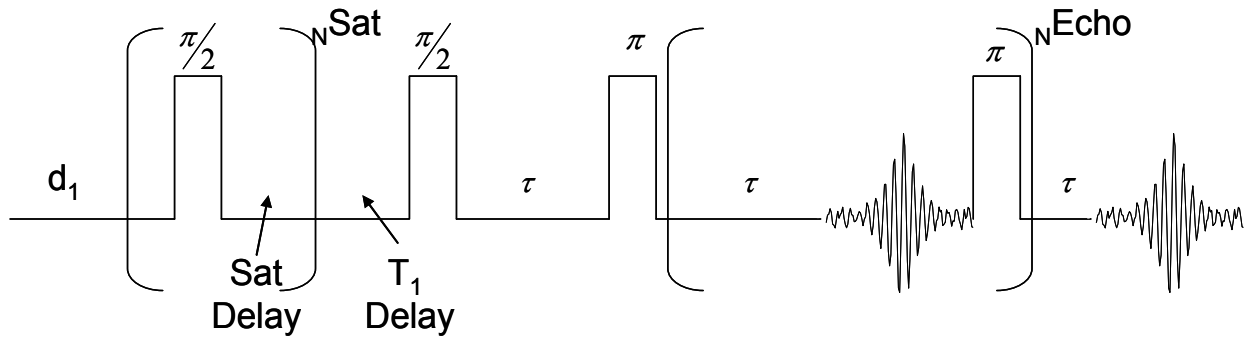


Figure 4.1: Pulse sequence used for saturation recovery – CPMG experiments.

Comparison of the total integrated signal area vs. relaxation delay allows for T_1 of the overall QD to be calculated. Analysis of the FID decay of each echo train, allows for the T_2 of the overall QD to be determined. T_1 and T_2 were calculated for the Cd^{77}Se samples using the following expressions

$$y(\tau) = A \times \left[1 - \exp\left(\frac{-\tau}{T_1}\right) \right] \quad (2)$$

$$y(\tau) = A_1 \times \left[1 - \exp\left(\frac{-\tau}{T_{2,1}}\right) \right] + A_2 \times \left[1 - \exp\left(\frac{-\tau}{T_{2,2}}\right) \right], \quad (3)$$

where $T_{2,1}$ and $T_{2,2}$ represent bi-exponential time constants for T_2 decay.^{128,131,133,134,136,145} Figure 4.2 shows ^{77}Se spin echo and ^{77}Se CPMG spectra for the 3.1 and 6.9 nm Cd ^{77}Se overlaid on top of each. Figure 4.2 shows the consistency between the experiments and that ^1H was not needed during the measurements.

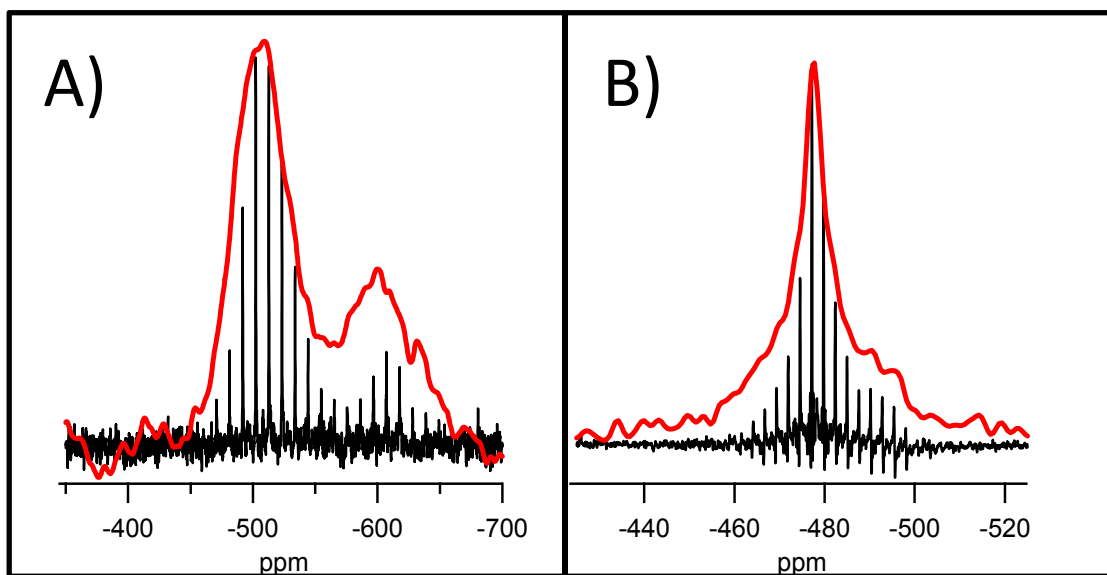


Figure 4.2: Overlay of ^{77}Se CPMG (black) and spin echo (red) showing consistency between two experiments. A) 3.1 nm CdSe, B) 6.9 nm CdSe.

4.2.4d ^1H Spin Lock: ^1H $T_{1\rho\text{H}}$ relaxations were measured using a spin lock pulse sequence with an acquisition time of 5 ms, recycle delay of 3 s, 90° pulse length of 5 μs and a spinning speed of 12 and 24 kHz. The spin lock time was varied from 5 to 145 ms.

4.2.5 Instrumentation

4.2.5a UV-Vis. Optical absorption was analyzed in a 1 - cm cell in toluene ($\sim 1 \times 10^6$ mol) using a Cary 50 UV-Vis spectrophotometer. The absorption maxima for the first exciton was used to estimate the QD size during the reaction to form the QD.¹²¹

4.2.5b Powder X-ray diffraction. Powder X-ray diffraction (pXRD) was carried out on a Rigaku DMAX 300 Ultima 3 diffractometer using Cu K_α ($\lambda = 1.5418 \text{ \AA}$) with the d -spacing calibrated to a Si_0 standard to verify crystal motif. Using the Debye-Scherrer¹⁴⁴

formula the QD diameter was calculated using the $\langle 110 \rangle$ peak which helps eliminate complications from overlapping reflections.

4.2.5c Transmission Electron Microscopy (TEM). QD size, dispersity, and morphology were analyzed by TEM using a JEOL-2010 microscope operated at 200 kV. The QDs were dispersed on holey carbon (400 mesh) from a toluene solution. Size dispersities were measured by averaging ~ 100 individual dots from the TEM.

4.2.5d X-Ray Fluorescence. Elemental composition analysis for Cd^{2+} and Se^{2-} were carried out in an Oxford Instruments ED₂₀₀₀ X-ray fluorescence spectrometer with a Cu K_α source. The Cd^{2+} to Se^{2-} mole ratio was determined for each sample by running four repeat analyses to minimize statistical error. For a standard XRF measurement, the powdered samples were completely dissolved in 90% HNO_3 , heated to remove excess NO_x , and then diluted to ~ 3 mL with a 2% HNO_3 solution (to allow compatibility with the XRF sample holder). All measurements were carried using the K_α line for Cd^{2+} (23.1 keV) and Se^{2-} (11.2 keV). Calibration curves were generated using commercially prepared 1000 ppm elemental standards in 2% HNO_3 , which results in accuracies of 3 ppm for Cd^{2+} and 4 ppm for Se^{2-} .

4.3 Results / Discussion

From a simplistic viewpoint, a QD can be envisioned as a fragment of a larger bulk crystalline lattice consisting of a series of shells in which the outermost layer is truncated along high energy lattice planes. The presence of surface passivants in the surface ligation layer can alter the bonding interactions in the QD potentially causing both the surface and the core to relax to minimize strain. Surface reconstruction in bulk materials is a common phenomenon that lowers the potential energy of dangling bonds and can result in strong perturbation of the chemical potential over multiple layers.¹⁴⁶ In Figure 4.3A, a simplified representation of the different potential environments experienced by a Se atom in CdSe can be defined, such that one can visualize a passivation layer dominated by the surface-to-ligand interaction (dark blue); a surface layer that is perturbed by the chemical potential of the ligation layer (light blue); and a core (white) that resembles the bulk chemical environment. If we consider the QD surface ligation layer (Figure 4.3B), dangling bonds due to unpassivated sites and ligation of the Cd (or Se) sites by a passivating ligand such as trioctylphosphine will

lower the local symmetry as well as change the chemical environment of those sites. Whether these local changes in chemical potential are represented as a gradient with complete global reconstruction (Figure 4.3C) or rapidly damped resulting in *only* the outermost layers being reconstructed (Figure 4.3D); will be strongly dependent on the material type, QD size, and nature of the passivant. Literature reports suggest either model may be applicable depending on the QD.¹¹²⁻¹¹⁴

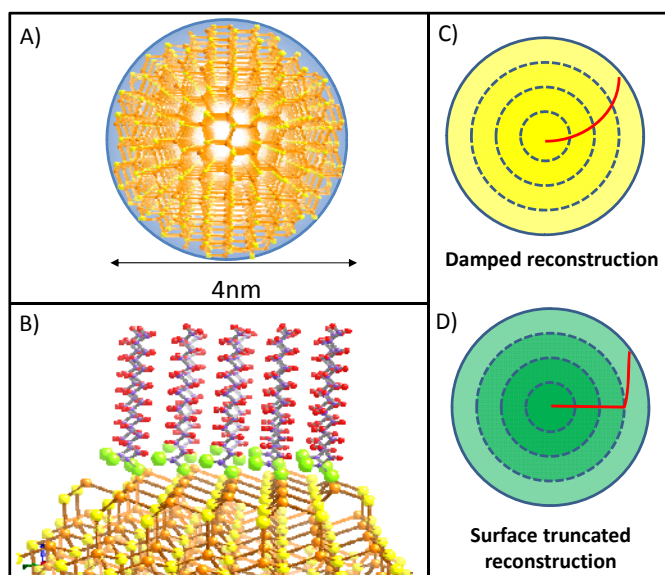


Figure 4.3: A) Drawing of a 4 nm, truncated wurtzite CdSe QD highlighting the distinctive regions within the QD representing the surface ligation layer (dark blue), near surface layers (light blue) and core layers (white). B) Ligand passivation layer on the <101> plane of a CdSe QD. C and D) Possible reconstruction models where lattice reconstruction induced by surface ligation is C) weakly or D) strongly damped by the within the lattice planes.

4.3.1 Analysis of passivating layer, surface, and core. Spherical Cd⁷⁷Se QDs passivated by stearic acid and TOP-⁷⁷Se in the size range 3.1 nm to 6.9 nm exhibiting a wurtzite morphology with 5-6% size dispersity were prepared by standard lyothermal growth methods using cadmium stearate and TOP-⁷⁷Se, and for comparison a 2.9 nm QD was grown without TOP-⁷⁷Se, via a single source precursor route¹⁴⁴ using Li₄[Cd₁₀⁷⁷Se₄(SePh)₁₆]. Characterization data (absorption, TEM, and pXRD) for the

individual QD samples are available in Figure 4.4. The results of $^{77}\text{Se}\{^1\text{H}\}$ CP-MAS and spin-echo NMR measurements on wurtzite Cd^{77}Se QDs are summarized in Table 4.1, which report chemical shifts of lineshape components observed in the NMR spectra. Peak intensities are not tabulated in Table 4.1 because they are not necessarily indicative to number of spins in the different reservoirs.

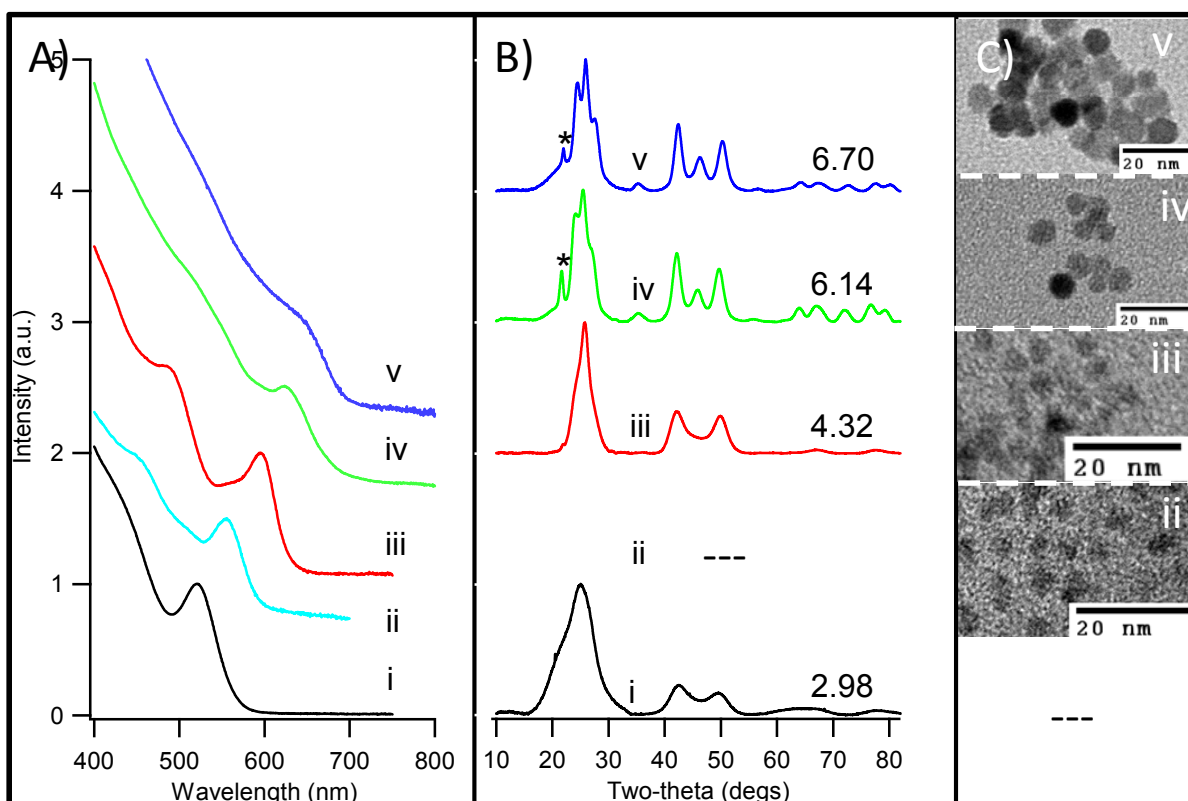


Figure 4.4: Characterization data for CdSe QDs I) 2.95 nm, II) 3.1 nm, III) 4.5 nm, IV) 6.1 nm, and V) 6.9 nm. A) UV-Vis, B) pXRD, and C) TEM.

The size dependent $^{77}\text{Se}\{^1\text{H}\}$ CP-MAS NMR measurements of Cd^{77}Se at multiple polarization times are shown in Figure 4.5. The CP-MAS NMR profiles exhibit both size and CP contact time dependent changes between 0 to -1000 ppm. The changes in the CP-MAS NMR profiles with contact time will be complex due to potential contributions from ligation layer influences of cross polarization dynamics and changes in spin

Table I: Summary of data

	$\text{Li}_4[\text{Cd}_{10}^{77}\text{Se}_4(\text{SePh})_{16}]$	Sample 1	Sample 2	Sample 3	Sample 4	Sample 5	Bulk	TOP- ^{77}Se
Peak Abs	---	521.0	554.6	595.1	626.4	646.9	---	---
Size _{XRD} (nm)	---	2.95	---	4.32	6.14	6.70	---	---
Size _{TEM} (nm)	---	---	3.08 ± 0.17	4.36 ± 0.05	6.15 ± 0.46	6.90 ± 0.49	---	---
Total Atoms	---	483	540	1528	4350	6199	---	---
# lattice planes in a,b/c	---	4/7	4/8	6/11	8/16	10/18	---	---
XRF - Cd:Se	1 : 2.12	1 : 1.08	1 : 0.9	1 : 0.95	1 : 1.03	1 : 1.05	1 : 1.03	---
^{77}Se T ₁ (sec)	---	270.7 ± 24.0	238.0 ± 27.3	163.1 ± 5.6	286.2 ± 7.8	209.7 ± 7.0	1667 ± 181	0.73 ± 0.06
^{77}Se T _{2,1} (msec)	---	61.3 ± 4.2	52.4 ± 8.9	37.1 ± 4.5	17.3 ± 1.1	16.6 ± 0.6	410.6 ± 57.9	198.1 ± 16.1
^{77}Se T _{2,2} (msec)	---	3.1 ± 0.1	3.7 ± 1.1	11.1 ± 3.2	4.4 ± 0.7	2.5 ± 0.4	24.0 ± 2.0	---
^{77}Se Spin Echo								
Peak 1 (ppm)	-650.7	-499.1	-500.9	-493.0	-480.8	-478.1	-472.3	-389.0
Peak 2 (ppm)	-697.5	540.8	-524.5	-543.8	-483.9	-479.1	---	-396.6
TOP- $^{77}\text{Se}^*$ (ppm)	---	---	-600.3	---	---	---	---	---
^1H - ^{77}Se CP-MAS								
Peak 1 (ppm)	---	-512.6	-501.2	-494.3	-485.8	-479.5	---	---
Peak 2 (ppm)	---	-520.8	-589.3	-569.3	-551.7	-500.6	---	---
TOP- $^{77}\text{Se}^*$ (ppm)	---	---	-602.4	-600.7	-601.6	-613.4	---	---

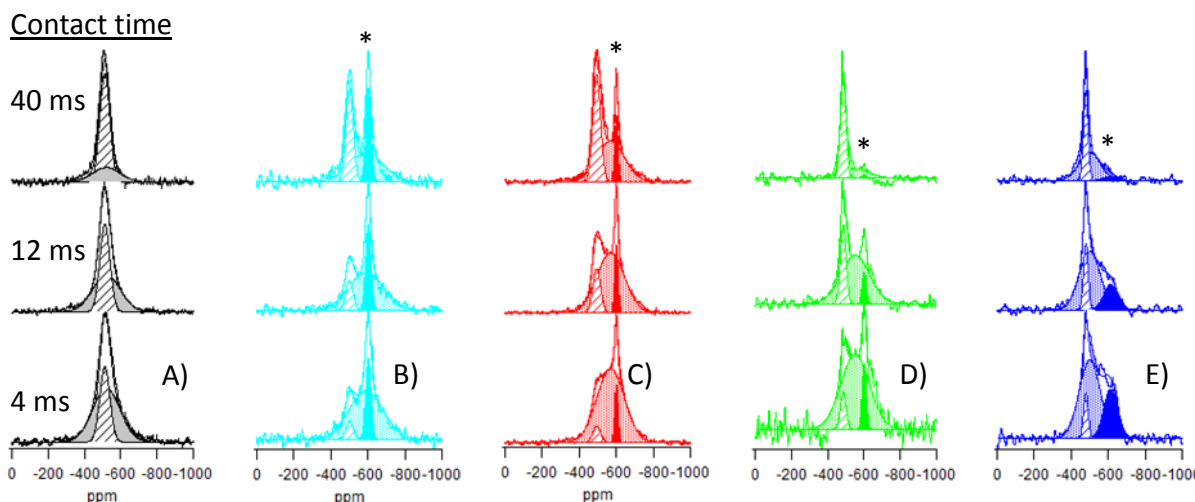


Figure 4.5: $^{77}\text{Se}\{^1\text{H}\}$ CP-MAS NMR at 4 ms, 12 ms, and 40 ms contact times for Cd^{77}Se QDs. A) 2.9nm (black), B) 3.1nm (light blue), C) 4.3nm (red), D) 6.1nm (green), and E) 6.9nm (dark blue). Fits are assigned as following: Peak 1 (slashed) core ^{77}Se sites; Peak 2 (dotted) near-surface and surface ^{77}Se sites; and Peak 3 (solid) surface ^{77}Se site bound to a TOP ligand. The peak labeled with * identifies the NMR resonance associated with a surface bound TOP through a ^{77}Se on the QD surface. The overall fit of the deconvoluted spectra has been added to each spectrum.

diffusion with size between the surface and core sublayers. Isotopic enrichment (99.7%) of ^{77}Se is expected to dramatically increase ^{77}Se spin diffusion rates in these samples. It is reasonable to expect that at short contact times (1-4 ms) the surface Se sites should be more efficiently polarized via direct ^1H - ^{77}Se dipolar couplings; at intermediate contact times (8-15 ms) a mixture of surface and core Se sites will polarize due to spin diffusion through the ^{77}Se lattice; and at longer contact times (>22ms) the core Se sites will be the dominant contributors through spin diffusion to the largest spin reservoir.

In Figure 4.5, the individual NMR features exhibit different spectral linewidth and contact time dependent intensities consisting of two reasonably sharp features and a broad feature (only one sharp feature and one broad feature were considered in lineshape fits for the 2.9 nm QD). Inspection of the ^{77}Se NMR features in Figure 4.5

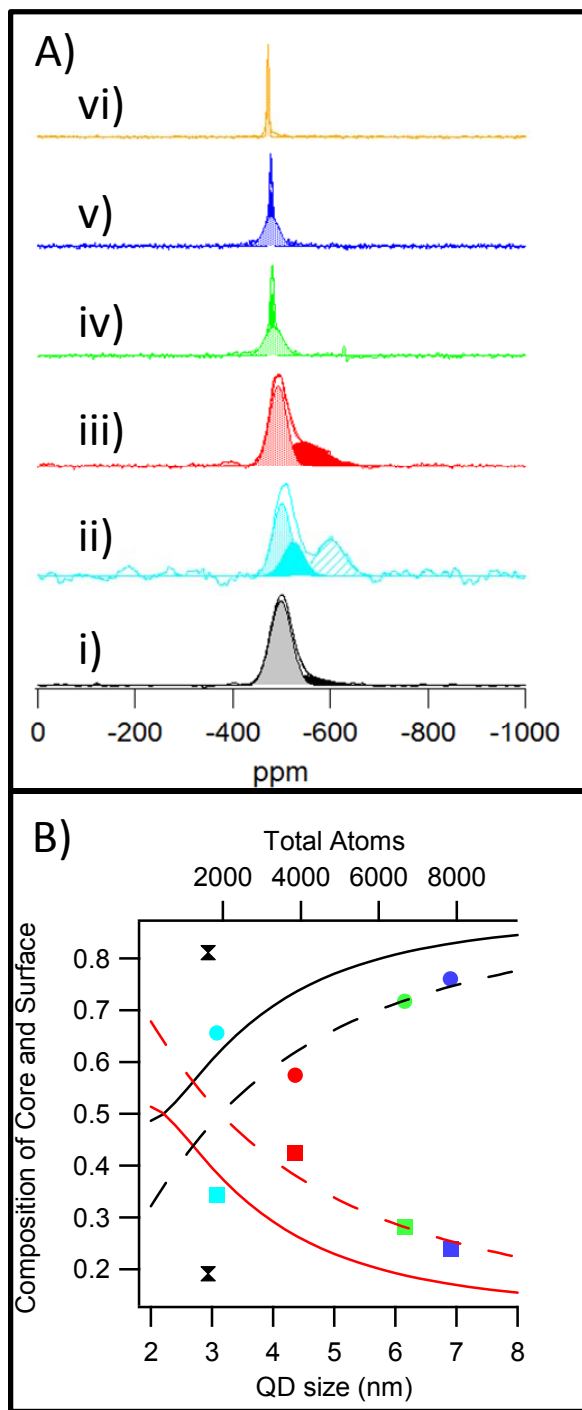


Figure 4.6: A) Spin echo (i-v) and direct pulse (vi) NMR of i) 2.9nm (black), ii) 3.1nm (light blue), iii) 4.3nm (red), iv) 6.1nm (green), v) 6.9nm (dark blue), and vi) Bulk CdSe (orange) B) Size dependent changes in the composition of surface and core assuming T_1 and T_2 are similar for the regions. Circles represent core signal and squares represent surface signals. The hour glass represents the smallest QD grown from cluster.

reveals all ^{77}Se signals have a more negative chemical shift in comparison to ^{77}Se in bulk CdSe. Since the efficiency of cross polarization drops rapidly with the distance, the CP-MAS NMR resonances between -479 to -512 ppm (Peak 1 in Table 4.1) observed to be most intense at the longest polarization times suggest these ^{77}Se NMR signature must arise furthest from the ligation layer and thus are assigned to core ^{77}Se sites (at least 2 to 3 lattice planes down). The broad feature (-500 to -590 ppm; Peak 2) and the sharpest feature (\sim -600 ppm; TOP- ^{77}Se peak, labeled with an asterisk in Figure 4.5) in the CP-MAS data are most intense at the shortest polarization times and thus likely reflect contributions from Se atoms at or near the passivation layer on the QD due to the short range efficiency of CP methods. The TOP- ^{77}Se feature (* in Figure 4.5) is assigned to the passivation of the QD due to the absence of the feature in the NMR for the 2.9 nm CdSe QD grown in the absence of TOP- ^{77}Se (Figure 4.5A). Furthermore, the assignment for TOP- ^{77}Se is consistent with the predicted NMR shift if one considers the relative electronegativities of selenium and phosphorus (2.55 and 2.19, respectively), which would result in increased shielding of ^{77}Se sites bound to TOP due to the increased electron density on the more electronegative Se atom. Finally, the assumption that the sharpest feature is TOP- ^{77}Se is also consistent with the greater rotational and translational freedom for the ligand.

The chemical shifts for Peaks 1 and 2 are QD size dependent and therefore it is reasonable to assume the ^{77}Se sites are assignable to lattice sites within the QD. The broader linewidth for Peak 2 with respect to Peak 1 may reflect a distribution in the chemical environments for these near-surface ^{77}Se sites. The chemical shift for the TOP- ^{77}Se peak (* in Figure 4.5) does not show a QD size dependence as expected for nuclei that have minimal interaction with the QD lattice. The validity of the assignments from CP-MAS are supported by the spin echo NMR for the bulk-like and surface like features (Figure 4.6A). The assignments of the core and surface sites for Se in Cd ^{77}Se are consistent with earlier reports.^{40,127}

Comparing CP-MAS data to spin-echo measurements provides further insight into the spectral features observed in NMR, since spin echo is a more quantitative representation of different ^{77}Se populations. For both CP-MAS and spin echo measurements, a decrease in the NMR intensity for the surface ^{77}Se (relative to the

core sites) is observed with increasing QD size (Figure 4.5 and 4.6A) as expected for the decreasing surface to volume ratio as the QD grows. The observation can thus be correlated with the number of atoms in the lattice planes of the QDs by plotting the percentage of the core and surface for a theoretical QD and for the integrated area for the NMR signals as a function of QD size (Figure 4.6). The contributions of the core and surface NMR signals from spin echo (Figure 4.6A) appear to follow a size dependent trend between 4.3 and 6.9 nm, while the ~3nm QDs do not follow the observed trend. The trend for QDs larger than 4 nm can be understood by considering the regions described in Figure 4.3A where a surface can be defined within 2 Å (~1 lattice plane, solid line) or within 3.25 Å (~2 lattice planes, dashed line). If we consider a projection along the <002> plane for a wurtzite CdSe QD, this observation would suggest that the assigned fits for surface contain surface and near surface Se atoms within the suggested 2 lattice planes, while the core Se resonances arise from the remaining $n-2$ lattice planes; n is the number of lattice planes.

Although the finding of significant changes occurring below 4 nm is in good agreement with experimental observations that QDs below 4 nm are structurally different,^{77,113,114} it is possible the failure to follow the surface to core trend lines in Figure 4.6B for QDs below 4 nm may reflect the low number of definable lattice planes for a QD of this size; lattice disorder arising from twinning or cubic inclusions in the wurtzite lattice;¹⁰⁷ or potentially a mixture of wurtzite and zinc-blende structures within the Cd⁷⁷Se QD sample.¹¹⁴ All these phenomena would result in local variations to atom density and the inability to follow a theoretical plot based on a pure wurtzite structure. Whether the assignment of definitive core and surface contributions reflect disorder or reconstruction is unclear; however, the observation of discrete core and surface NMR signatures that correlate with the number of lattice planes and the size of the QD, suggests significant reconstruction occurs over several layers, while the core sites experience a smaller degree of reconstruction for QDs bigger than 4 nm in diameter (Figure 4.3D).

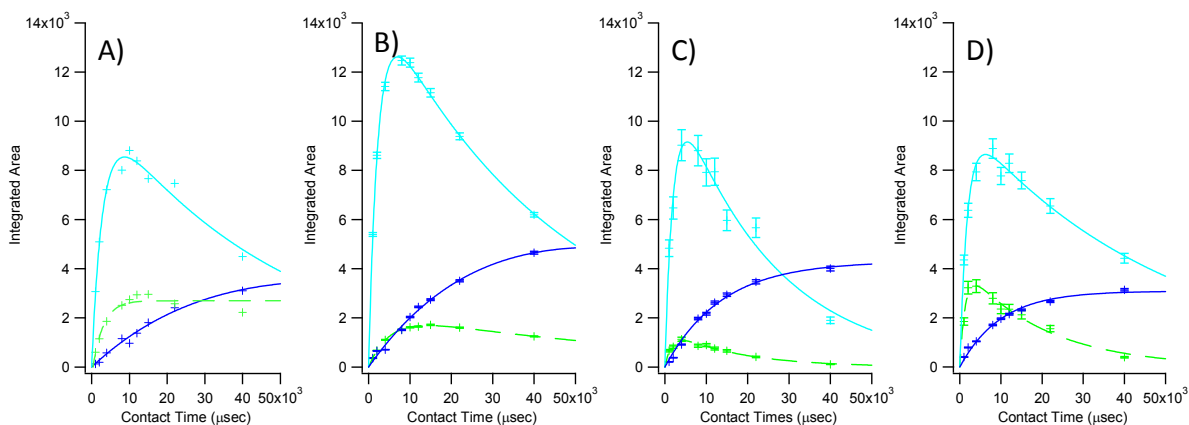


Figure 4.7: $^{77}\text{Se}\{^1\text{H}\}$ CP-MAS build up curves for A) 3.1nm , B) 4.3nm, C) 6.1nm, E) 6.9nm Cd ^{77}Se QDs. The dark blue line represents the intensity of the core (peak 1) ^{77}Se sites, the light blue line represents surface (peak 2) ^{77}Se sites, and the green line represents the ligation layer (peak 3) for ^{77}Se bound to TOP. Contact times used to generate build up curve are: 1, 2, 4, 8, 10, 12, 15, 22, and 40 ms.

4.3.2 Site dependent CP buildup curves. Although the data in Figure 4.7 fit well to the canonical CP buildup equation (Eq 1),¹⁴⁷ this equation was derived with limiting assumptions that are not appropriate to the present samples. For a 100% enriched sample the i) ^{77}Se is not low in abundance relative to ^1H because of its isotopic enrichment,¹⁴⁷ and ii) homonuclear dipolar coupling allows signal enhancement of ^{77}Se sub-layer atoms that are not directly coupled to ^1H . The breakdown of assumption (i) can result in an increase of the observed time constants relative to the values expected in the limit of low ^{77}Se abundance.^{135,147-150} To properly describe the CP data in Figure 4.7 and Table 4.2, ^{77}Se spin diffusion from the cross-polarized surface into the bulk of the QD must be considered and thus in the study we use the superscript * to emphasize that T^*_{HSe} , $T^*_{1\text{pH}}$ are phenomenological parameters that are affected by the non-negligible population of the ^{77}Se reservoir and by ^{77}Se spin diffusion.

The best-fit time constants, T^*_{HSe} and $T^*_{1\text{pH}}$, for core, surface and TOP bound ^{77}Se as a function of Cd ^{77}Se QD size are summarized in Table 2. For the two smallest QD samples (3.1 and 4.3nm), the TOP- ^{77}Se layer exhibits a longer T^*_{HSe} than the surface QD layer. This result suggests differential importance of ligand binding on different QD surfaces; in other words, the surface Cd ^{77}Se layer is most strongly coupled

to a subset of the overall TOP- ^{77}Se . Comparing the data for the TOP- ^{77}Se layers for different QD sizes, an apparent discontinuity is observed between the small samples (3.1 and 4.3nm) and the larger samples (6.1 and 6.9nm). This observation could suggest an abrupt size dependent change in the passivant layer as previously reported.¹²⁰ Repeated measurements confirm the values in Table 4.2 suggesting that the results are not experimental artifacts.

The origin of the anomalies observed for the surface T^*_{HSe} and $T^*_{1\rho\text{H}}$ in the 6.1 nm Cd^{77}Se and the $T_{1\rho\text{H}}$ observed in the 4.3 nm Cd^{77}Se is unclear. A possible explanation for the behavior at 6.1 nm could concern the formation of a stable crystalline facet which has been observed to change the apparent ligand packing for CdSe above 4.5 nm.¹²⁰ Although the frequency of the assigned ^{77}Se resonance for the TOP- ^{77}Se in the CP-MAS data shows no discernable shift with QD size, the 4.3 nm Cd^{77}Se QD data exhibit a directly detected $T_{1\rho\text{H}}$ that is smaller than the analogous value extracted by CP-MAS. This observation indicates ^{77}Se is likely only polarized by a small subpopulation of ^1H on the surface. Inspection of the direct pulse MAS measurement for the ^{31}P data for the QDs with size (Figure 4.8) confirms this assumption since two distinct ^{31}P species are observed

Table 4.2: Time Constants for Cd⁷⁷Se QDs
 (The --- indicate the $T_{1\rho H}^*$ for the core signals are too long to be measured in the experimental time frame)

⁷⁷ Se CP-MAS		Sample 2 (3.1nm)	Sample 3 (4.3nm)	Sample 4 (6.1nm)	Sample 5 (6.9nm)
Peak 1 (Core, Blue)	T_{HSe}^* (ms)	28.5 ± 5.7	22.6 ± 2.5	13.7 ± 1.2	9.9 ± 0.9
	$T_{1\rho H}^*$ (ms)	---	---	---	---
Peak 2 (Surface, Teal)	T_{HSe}^* (ms)	2.9 ± 0.3	2.2 ± 0.1	2.0 ± 0.3	1.7 ± 0.3
	$T_{1\rho H}^*$ (ms)	48.7 ± 7.1	43.6 ± 1.4	23.5 ± 3.4	49.3 ± 5.2
Peak 3 (TOP-⁷⁷Se, Green)	T_{HSe}^* (ms)	5.0 ± 0.5	5.1 ± 0.2	1.7 ± 0.3	1.3 ± 0.2
	$T_{1\rho H}^*$ (ms)	75.8 ± 14.5	67.9 ± 3.9	16.7 ± 2.3	19.6 ± 2.7
¹H Spin Lock	$T_{1\rho H}$ (ms)	83.1 ± 0.9	21.52 ± 0.7	28.36 ± 0.5	31.9 ± 0.6
	$T_{1\rho H}$ (ms)	19.3 ± 0.6	7.7 ± 0.2	9.06 ± 0.5	9.3 ± 0.3
Calculated by overall integration of ⁷⁷Se CP-MAS intensities	T_{HSe}^* (ms)	3.1 ± 0.2	2.1 ± 0.1	1.7 ± 0.2	1.3 ± 0.1

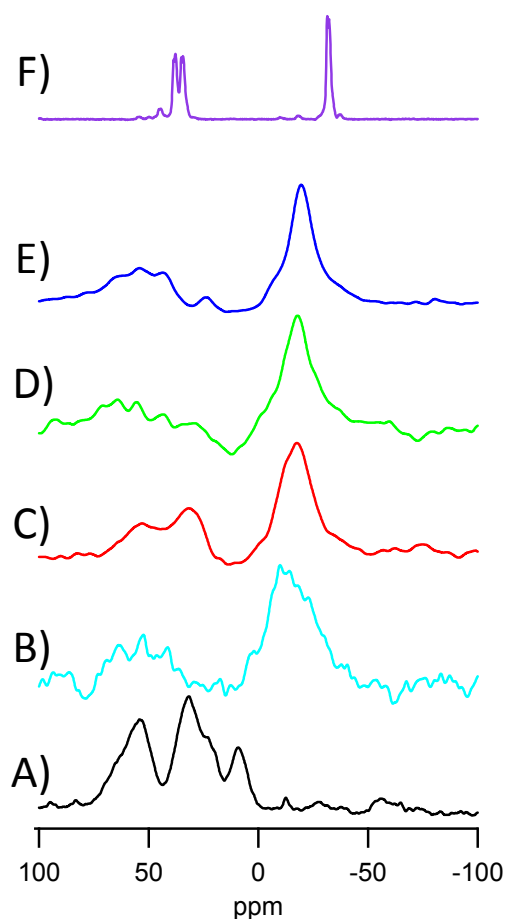


Figure 4.8: ^{31}P Direct pulse MAS NMR on A) 2.9 nm, B) 3.1 nm, C) 4.3 nm D) 6.1 nm, E) 6.9 nm, F) TOP-Se

TOP and TOPO. Analyzing the total integrated area between the two regions suggest that the percentage of TOP bound to Se, TOP to Cd, and TOPO in the samples are unfortunately not uniform across the QD samples and require further investigation into the reaction conditions (temperature, time, reactants) and size dependent changes to the observed surface passivation. This is also apparent in the ^1H NMR under high spinning speed (24 kHz) showing that multiple sites are present. Although this does not eliminate the possibility of changes in the ligand packing modulating the degree of reconstruction, it is also possible that as the QD grows changes to specific features⁴⁰ (edge, vertex) on the surface of the QD may result in the observed discontinuity in TOP- ^{77}Se T^*_{HSe} and $T^*_{1\text{pH}}$ with QD size. The change in ligand packing at the QD surface

could potentially impact the cross-polarization behavior for this size domain; however, it is not possible to definitively support this observation based on the NMR results alone.

To ensure the values for T_{HSe}^* (build-up time constant) and $T_{1\rho\text{H}}^*$ (decay time constant) are not misinterpreted in CP-MAS experiments, the value of $T_{1\rho\text{H}}$ must be independently measured using a ^1H detected spin lock experiment to validate the assignments from CP-MAS.¹⁵¹ In Figure 4.9 the ^1H spin-lock experiment on the Cd^{77}Se QDs exhibits multiple ^1H contributions attributable to different ^1H sub-populations with mobility differences. While ^1H spectra lack the resolution necessary for making assignments, different ^1H sites include positions along the alkane chain or TOP passivants on potentially different QD faces.

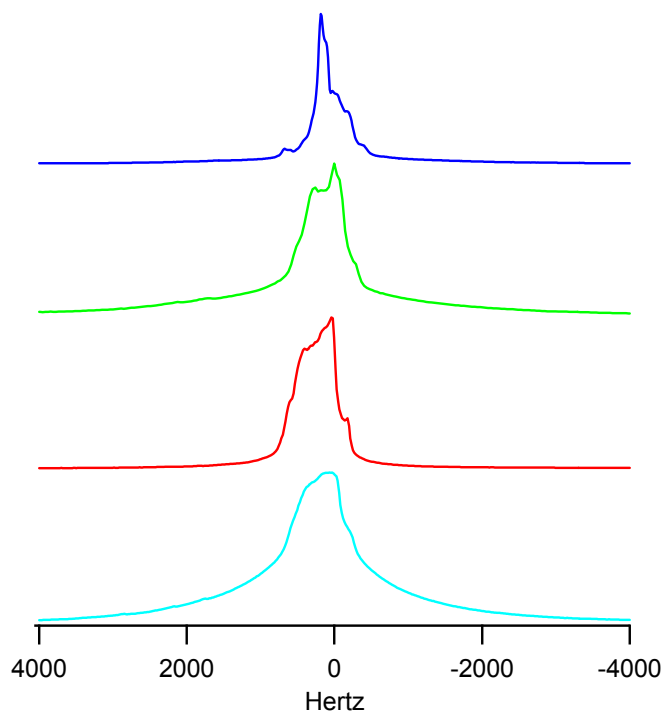


Figure 4.9: ^1H Spin Lock Experiment at a spinning speed of 24kHz. The higher spinning speeds allows for the multiple ^1H features to be observed.

The measured $T_{1\rho\text{H}}$ and $T^*_{1\rho\text{H}}$ correlate best for $^{77}\text{Se}\{^1\text{H}\}$ CP-MAS signal from TOP- ^{77}Se ; we consider this result reasonable because these ^{77}Se atoms are most strongly coupled to ^1H . These values are much longer than the values assigned to T^*_{HSe} , confirming the validity of the assignments. We were not able to obtain a good fits to the TOP- ^{77}Se CPMAS buildup data using the directly measured ^1H $T_{1\rho\text{H}}$ values, indicating that different ^1H sites transfer polarizations to ^{77}Se with different degrees of efficiency. Since surface and core regions correspond to ^{77}Se that is not directly coupled to ^1H , we believe the larger observed $T^*_{1\rho\text{H}}$ are subject to spin diffusion effects.

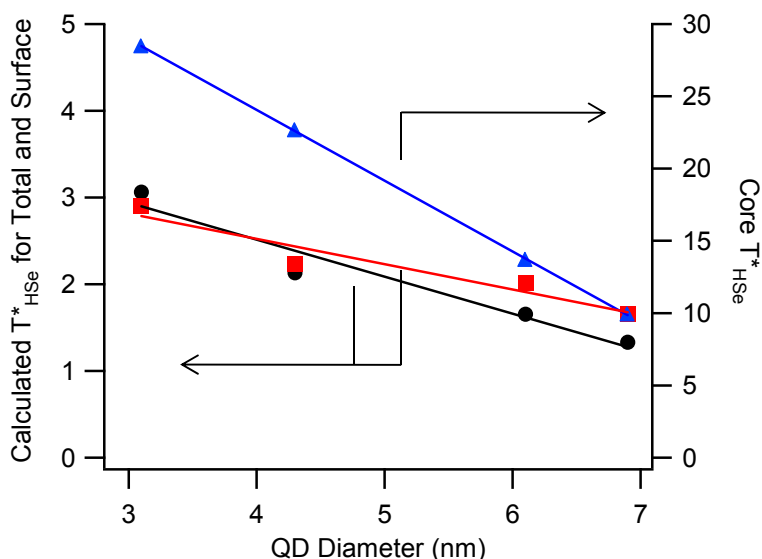


Figure 4.10: T^*_{HSe} for surface (red), core (blue), and total (black) ^{77}Se vs. QD diameter. Solid curves are best fit lines.

4.3.3 Spin Diffusion and Anticipated Size Effects from Spin Diffusion. The measured T^*_{HSe} values in Table 4.2 are observed to depend both on depths within a QD and overall QD size. A plot of the T^*_{HSe} data versus size for the surface, core, and total integrated NMR intensity exhibits a linear decrease with increasing size (Figure 4.10). It should be noted that the total T^*_{HSe} was determined by fitting the rise of total

integrated ^{77}Se intensity from Figure 4.5 for CP contact times up to the peak intensity in each build-up curve. Since CP-MAS measurements are dominated by short range contacts, the value for T_{HSe}^* most likely reflects spin diffusion from the surface layers into the core of the QD. The observed linear decrease with size is suggestive of a diffusion problem within the QD; which would be expected to be important given the QD size dependent surface curvature and surface-to-volume ratio. Unfortunately, a purely geometric approach to describing the T_{HSe}^* data in terms of spin diffusion as a function of QD size as described by a Fick's Law diffusion analysis in which the QD core is assumed to be represented by spherical symmetry and uniform spin diffusivity is not capable of explaining the QD size trends in Figure 4.10. Fick's model predicts an *increase* rather than the observed *decrease* in T_{HSe}^* for the total integrated signal as the QD increases in size. Possible explanations of the observed behavior can be described in terms of a breakdown of assumptions underlying the spin transport model, which assumes the spin diffusion is not influenced by the interfaces that arise in a QD, and more importantly will be size dependent. Chemical shift differences between surface and core ^{77}Se signal suggest that the surface layer has a different structure from the core and that spin diffusivity should vary between sub-layers. The surface layer could be a diffusional barrier with decreasing thickness as QDs grow indicative of a size dependent reconstruction in the outer layers of a Cd^{77}Se QD. Size dependent surface properties may also play a role since shorter T_{HSe}^* for larger QD samples could be explained in terms of increased ligand coverage, ligand packing differences on the QD facets, and decreased ligand dynamics.¹²⁰ Although spin diffusion appears to be critical for the CP-MAS build up behavior, the observed size dependence of T_{HSe}^* for the TOP- ^{77}Se does not explain the QD size dependence of the T_{HSe}^* in the deeper layer under the simplified spin diffusion model.

Figure 4.10 shows a clear dependence of T_{HSe}^* on depth and overall QD size. A possible explanation for QD size effects could be geometric effects on spin diffusion. If we make simplifying assumptions of spherical symmetry, uniform ^{77}Se spin diffusivity, and constant passivation layer properties (e.g., ^1H density and molecular dynamics), analysis of Fick's law spin diffusion could be used to predict a QD size dependence of T_{HSe}^* . In addition, we neglect any loss of ^{77}Se or ^1H magnetization by assuming that T_1

or $T_{1\rho}$ are infinite for both nuclei. The governing spin polarization transport equation for this model would be,

$$\frac{\partial I_z}{\partial t} = \frac{D}{r^2} \frac{\partial}{\partial r} \left(r^2 \frac{\partial I_z}{\partial r} \right) \quad (4)$$

where I_z is the ^{77}Se nuclear spin polarization, D is the ^{77}Se spin diffusivity, r is a radial coordinate centered at the center of the QD, and t is CP contact time. At the surface of the QD, we model CP build-up using the boundary condition at $r = a$,

$$-\frac{D}{a} \frac{\partial I_z}{\partial r} = \frac{1}{T_{HSe}} (I_z - I_{z,CP}) \quad (5)$$

where a , is the QD radius, T_{HSe} is a time constant for $^{77}\text{Se}\{^1\text{H}\}$ CP via direct dipolar coupling, and $I_{z,CP}$ is the “infinite time” ^{77}Se spin polarization in thermal equilibrium with spin-locked ^1H . This mathematical problem is equivalent to a problem described by Crank¹⁵² involving surface evaporation of solute from an initially uniform spherical particle. The solution for the time dependence of overall cross polarized ^{77}Se signal

$\propto \left(\int_0^a I_z dr \right)$ is,

$$\frac{T}{T_\infty} = 1 - \sum_{n=1}^{\infty} \frac{6L^2 \exp(-\beta_n^2 D t/a^2)}{\beta_n^2 (\beta_n^2 + L(L-1))} \quad (6)$$

where T is the total integrated ^{77}Se NMR intensity and T_∞ is its infinite-time asymptotic

value. The parameter L is defined as $L \equiv \frac{a^2}{T_{HSe} D}$, and β_n is the n^{th} root of

$\beta_n \cot \beta_n + L - 1 = 0$. With conservative estimates for a , T_{HSe} , and D ($a^2 \geq 9.6 \text{ nm}^2$, $T_{HSe} < 10^{-2} \text{ s}$, $D < 10 \text{ nm}^2/\text{s}$), it is reasonable to expect $L \gg 1$ and $\beta_n \approx n\pi$. In this regime, β_n would depend weakly on a and T_{HSe} . Considering only the most significant term ($n = 1$) of the infinite series in Equation 6, this model predicts $T_{HSe}^* \sim a^2/(\pi^2 D)$. Thus, this

simple spin transport model would predict a roughly quadratic increase in the observed T_{HSe}^* with increasing QD radius.

The black curve in Figure 4.10 (T_{HSe}^* measured by integrating the whole ^{77}Se lineshape in variable CP contact experiments) clearly shows that observed build-up of ^{77}Se CP-MAS NMR signal is not consistent with the presented transport model. T_{HSe}^* decreased with increasing QD diameter instead of exhibiting an increase proportional to a^2 . Although the data in Table 4.2 show a decrease in observed T_{HSe}^* in the TOP- ^{77}Se with increasing QD radius, under this model such a variation is also unlikely to explain the observed size dependence of T_{HSe}^* for the overall ^{77}Se integrated intensity.

4.3.4 T_2 Spin-Relaxation Dynamics. The measurement of transverse spin relaxation rates in the Cd^{77}Se QD are complicated by the presence of dipole-dipole coupling, structural interfaces, and the near unity isotopic enrichment of the ^{77}Se sites, although homonuclear coupling effects are attenuated by MAS. Dipole-dipole coupling in semiconductors has recently attracted much attention due to the differences in reported T_2 values when measured by CPMG (Carr Purcell Meiboom Gill) and Hahn-echo approaches.^{133,134,138,145,153} The recent studies on semiconductors have indicated complex spin relaxation pathways in semiconductors, including Si, Ge, and Y_2O_3 , may give rise to a bi-exponential decay for CPMG measured process in which the long T_2 relaxation has been attributed to dipole-dipole coupling. The exact nature of the bi-exponential relaxation in the CPMG results is still under discussion.¹⁴⁵

The T_1 and T_2 spin-relaxation data were measured for the total sample without attempting to deconvolute the contributions of specific sites. Although the measurement of T_1 and T_2 for individual components would be ideal, unfortunately these experiments are cost preventative and difficult to assess due to overlapping signals. The ensemble averaged T_1 and T_2 signals were measured by saturation recovery - CPMG techniques^{154,155} (Figure 4.11 and summarized in Table 4.1). In all cases the T_1 is fit to a single exponential decay, while the T_2 is fit to a bi-exponential decay. The experimental results for the CdSe QDs indicate that only a small size dependence in T_1 values (160 to 286 s) is observed; however, larger changes in long time component of T_2 decay occur with size. The fast T_2 component does not follow any obvious size

dependence 4.3nm sample seems to be an outlier. It is worth noting the size range is reminiscent of the discontinuity that occurs for ligand packing on CdSe,¹²⁰ elastic modulus changes,¹¹³ and the measured $T_{1\rho H}$ data. We speculate this may suggest this QD size may be structurally and electronically unique, further studies are underway. The slower T_2 decay component decreases from $T_{2,1} = 61$ (2.9 nm) to $T_{2,2} = 16$ ms (6.9 nm).

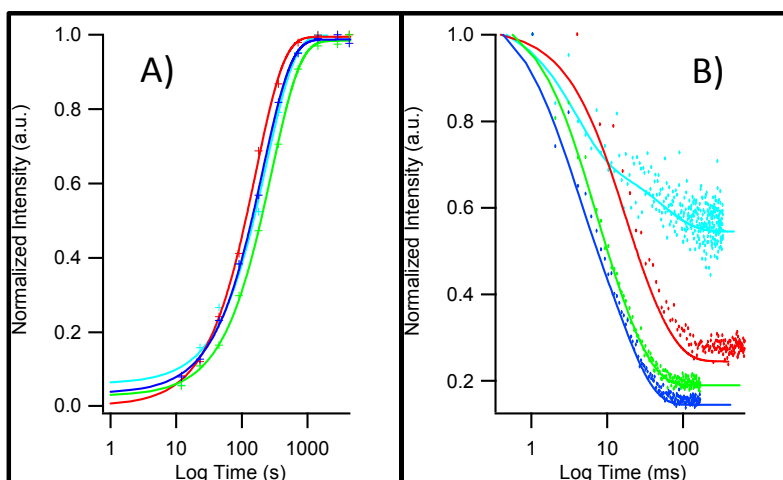


Figure 4.11: Size dependent A) T_1 and B) T_2 data for Cd⁷⁷Se: 3.1nm = light blue, 4.3nm = red, 6.1nm = green, 6.9nm = dark blue. The data is fit to a single exponential function for T_1 and bi-exponential function for T_2 .

4.3.5 Changes in bonding. Changes in the structural and associated electronic environments in QDs will impact the chemical bonding.^{41,43,139} X-ray diffraction has shown the Se atoms in the core of the CdSe QD exist largely in chemically similar tetrahedral environments, while the surface sites exist in distorted sites due to surface ligation and dangling bonds. Recent experimental results on core and core-shell QDs indicate the structural changes may be more complex with depth dependent localized changes in the lattice.^{114,116,119} Interrogation of the NMR spectra provide direct insight into the size dependent changes in atomic disorder and local chemical potential changes occurring around the Se atoms as a function of size by analysis of the chemical shift anisotropy.

The expected change in the chemical shift for the Se sites as a function of size can be rationalized by considering the implication of changes in bonding around the Se atom through the use of the Ramsey expression.^{42,127,156} The Ramsey expression relates σ_p^{iso} to the probability of an electron being in the excited state which can lead to less shielding and a more positive chemical shift. The paramagnetic term is defined as

$$\sigma_p^{iso} = -\frac{\mu_0 e^2 \hbar^2}{8m_e^2 \pi} \sum_{n \neq 0} \frac{1}{\Delta E_n} \left[\left\langle 0 \left| \sum_l \frac{\delta}{\delta \phi_l} \right| n \right\rangle \times \left\langle n \left| \sum_l \frac{\delta}{\delta \phi_l} \frac{1}{q_l^3} \right| 0 \right\rangle + \left\langle 0 \left| \sum_l \frac{\delta}{\delta \phi_l} \frac{1}{q_l^3} \right| n \right\rangle \times \left\langle n \left| \sum_l \frac{\delta}{\delta \phi_l} \right| 0 \right\rangle \right], \quad (7)$$

where μ_0 is the permittivity of vacuum, e is the charge of an electron, \hbar is Planck's constant divided by 2π , m is the mass of an electron, ϕ_l is the angular momentum operator which is the change in l with respect to the magnetic field, and q_l is the distance between two dipoles. ΔE_n in the equation is the energy separation between the ground state, $|0\rangle$, and n^{th} excited state, $|n\rangle$, which scales with the bandgap (E_g) in a semiconductor.^{42,127,156}

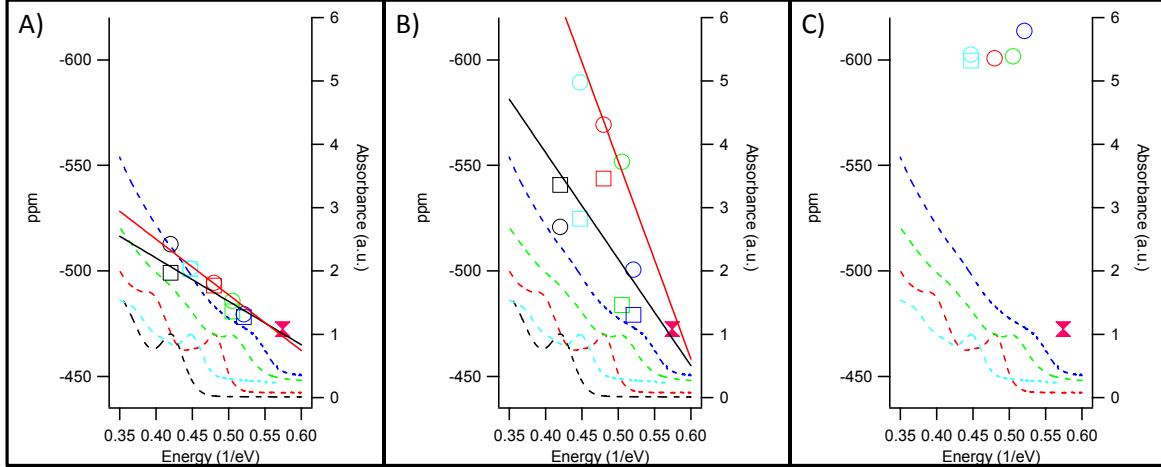


Figure 4.12: Ramsey plot of chemical shift (ppm) and absorbance with respect to inverse band gap energy (1/eV) for Cd⁷⁷Se QD samples (2.9nm (black), 3.1nm (light blue), 4.3nm (red), 6.1nm (green), 6.9nm (dark blue)). Pink hour glass represents bulk CdSe within all three plots. A) Represents core ⁷⁷Se sites B) Represents near-surface and surface ⁷⁷Se sites C) Represent surface ⁷⁷Se sites bound to TOP. Open circles correlate to CP-MAS assignments and open squares correlate to spin echo assignments.

A plot of the chemical shift for the core (Figure 4.12A), surface (Figure 4.12B) and TOP-⁷⁷Se (Figure 4.12C) resonances versus the inverse bandgap energy are in agreement with the Ramsey expression but the differences between the specific sites are informative. The spin-echo and CP-MAS exhibit different slopes for the data but the same trend for the core and surface resonances. The NMR resonances for the core and surface terms exhibit a shift to a more positive value with increasing size (decreasing bandgap) with the core component exhibiting a shallower slope than the surface term. The observed linear shift in the core and surface with size suggests that the ⁷⁷Se sites are more shielded as the QD size decreases, particularly at the surface sites. The TOP-Se signal exhibits no significant change in chemical shift. The lack of an observed shift for TOP-Se is not surprising, as the ligation of the surface is expected to be largely insensitive to changes in the QD structure as the bonding interaction between Se and phosphorous is dominated by *d*-back bonding interactions. The shift in frequency with size for the core component is consistent with the early reports correlating the Ramsey equation predicted shift with bandgap energy in QDs.^{42,127}

The strongest evidence of the observed “Ramsey-like” behavior for the NMR chemical shift and the QD size can be generated by plotting the chemical shift change with respect to the effective mass approximation commonly referred to as the “Brus” equation. It can be shown that the chemical shift, $\Delta\nu(\nu_{\text{bulk}} - \nu_{\text{QD}})$ is inversely proportional to $\Delta E_g(E_g(\text{bulk}) - E_g(\text{QD}))$ based on the Ramsey expression.¹⁵⁷ Thus one may write an expression linking $\Delta\nu$ to the size dependent effective mass approximation, such that

$$\frac{1}{\Delta\nu} = \frac{ad^2 + bd + c}{d^2} \quad (8)$$

where *d* is the radius of the QD, *c* is an empirical constant for the confinement term, *b* is a constant for the coulomb term, and *a* is a correction term.⁷⁰ The fit of Eq 8 is shown in Figure 4.13 indicating good agreement between the observed chemical shift and the observed optical transition for the first exciton ($1S_{3/2} \rightarrow 1S_e$) in the CdSe QD. The ratio of the confinement to Coulomb term is consistent for the spin-echo and CP-MAS experimental fits (~1.2 (core) and ~ 1.1 (surface)), and more importantly are similar to

the ratio extracted from the optical experiment (1.5), implying the observed correlation of NMR and EMA is meaningful.

The results confirm the NMR measured core and surface signatures represent independent sites that are uniquely coupled to changes in the internal electronic properties of the QD and thus the size dependent correlation of the NMR shifts to the Ramsey expression and the effective mass approximation has implications with respect to the orbital hybridization for the Se atoms within the QD. To rationalize the slope difference in Figure 4.12 between the core and surface, a model to explain the observed chemical shift difference based on changes in the electron orbital hybridization for a Se atom in a tetrahedral site is useful.

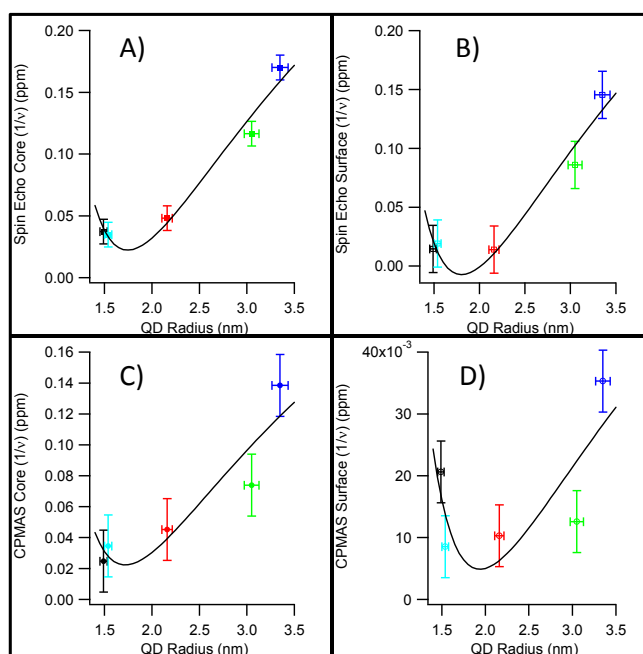


Figure 4.13: Spin Echo and CP-MAS (contact time = 12 ms) ⁷⁷Se NMR data illustrating the change in chemical shift vs. QD size. A) Spin Echo core, B) Spin Echo surface, C) CP-MAS core, and D) CP-MAS surface sites. Cd⁷⁷Se QD samples: (2.9nm (black), 3.1nm (light blue), 4.3nm (red), 6.1nm (green), 6.9nm (dark blue)).

The bonding for the Se atom is dominated by a mixture of *s*, *p* and to a partial extent *d*-orbital overlap with Cd. Of these the valence band for CdSe is largely dominated by the Se *p*-orbital character. Using a simple hybridization model to assess the bonding for a Se atom in tetrahedral symmetry, the sigma bonding interaction can be approximated as 0.25 *s*-orbital character and 0.75 *p*-orbital character per bond. As the tetrahedral symmetry is reduced by trigonal or tetragonal distortion, the bonding will exhibit an increase in the *s*-character. An increase in *s*-character would result in increase in electron density at the nuclei and thus a resonance with a more negative chemical shift. X-ray absorption spectroscopy analysis¹⁵⁸ of CdSe QDs support the conclusion of increasing *s*-character is with decreasing QD size. While the XAS methods cannot distinguish between core and surface atoms, it is reasonable to believe the logic is transferrable and an increasing *s*-character in the conduction band (Cd based orbital) is consistent with the increased surface to core contribution to decreasing size. The results are consistent with the NMR results from Chmelka, *et. al.* on ZnSe postulated electronic changes in the QD based on density functional theory predictions.¹³⁹

A more quantitative analysis of this simple model is provided by further interpreting the Ramsey expression in terms of the orbital overlap model since σ_p is dominated by the 4_p electrons on Se,

$$\sigma_p \sim \langle r^{-3} \rangle_{4p} \cdot \Delta E^{-1} \cdot \sum Q \quad (9)$$

where $\langle r^{-3} \rangle_{4p}$ is the inverse cube of the radius of the 4_p electrons (orbital extension); ΔE^{-1} is the mean excitation energy which is correlated to the bandgap energy in semiconductors; and $\sum Q$ is the charge-density-bond order matrix.^{156,159} While it is difficult to independently interpret the three factors since $\langle r^{-3} \rangle_{4p}$ and $\sum Q$ are closely connected, the trend in the data can be interpreted for the core versus surface by invoking changes in the respective orbital character. For a given size if the symmetry is reduced from a pure T_d site at the surface; the *s*-character in the bond increases, while the *p*-character decreases, in effect reducing the bonding interaction ($\sum Q$) between the *p*-orbital on the Se and the Cd resulting in a smaller value for σ_p and thus a more negative chemical shift for the surface resonances. The oversimplified angular orbital

overlap model correlates well with the observations from the Ramsey plot (Figure 4.12). Thus the QD can be envisioned as consisting of core layers with undistorted tetrahedral symmetry sites and a self-terminated outer shell that experiences reconstruction (Figure 4.3). The differences in chemical environment lead to the experimental observation that the core ^{77}Se resonances are shifted to a more positive chemical shift relative to the surface (outer shell layers) Se atoms. Physically the results most likely reflect a combination of changes in the lattice strain arising from broken symmetry due to ligation of the surface, reconstruction of un-ligated sites (dangling bonds), and the contributions from ligand induced compression. Interpreting the observed chemical shift with size implies a decrease in the orbital overlap for both core and surface occurs as the QD grows. From a bonding perspective this could be interpreted as a decrease in the covalent character of the bond as the QD increases in size. Such a change is reasonable as bulk CdSe is better described as an ionic semiconductor, while a cluster of CdSe atoms is better describe as a coordination type complex with greater covalent character.

4.4 Conclusions

The NMR results strongly support a model in which Cd ^{77}Se QDs contain core and surface regions. For QDs with diameters less than 4 nm, reconstruction seems to be more global (Figure 4.3C), effecting both surface and core signals. Cd ^{77}Se QDs greater than 4 nm in diameter are better modeled by a strongly localized, surface truncated model (Figure 4.3D) in which reconstruction is limited to the surface region. Trends measured by NMR support the interpretation that reconstruction is more extreme for small QDs supporting previous claims that QDs undergo surface reconstruction to relieve the stress created due to truncation of the high energy surface planes. Analysis of direct polarization and ^{77}Se CP-MAS NMR indicates that surface layer thickness and ligand surface coverage depend on QD size due to surface reconstruction. Sub-layer ^{77}Se is polarized in a CP-MAS experiment by ^{77}Se spin diffusion through isotopically enriched lattices, though polarization transport in spherical geometry alone is not enough to explain observed size dependences of observed relaxation and polarization transfer rates.

The precise ^{77}Se NMR peak shifts can be correlated with size dependent core and surface site contributions. The different observed slopes for the core and surface chemical shifts from the Ramsey equation suggest unique depth-dependent bonding character exists in the QD. Valence bond theory arguments coupled to the Ramsey expression and EMA imply the highly distorted surface leads to greater s-character than the core, implying the bonding is distorted from T_d to a trigonal or tetragonal symmetry in the outer shell of the QD. The increase in s-character for these distorted surface sites result in further shielding of the nuclei and thus the observed chemical shift is a more negative value.

REFERENCES

- (1) Alivisatos, A. P. *Journal of Physical Chemistry* **1996**, *100*, 13226-13239.
- (2) Karlin, K. D. *Progress in Inorganic Chemistry*; John Wiley & Sons, Inc, 2005; Vol. 54.
- (3) Barick, K. C.; Bahadur, D. *Journal of Nanoscience and Nanotechnology*, *10*, 668-689.
- (4) Bawendi, M. G.; Steigerwald, M. L.; Brus, L. E. *Annual Review of Physical Chemistry* **1990**, *41*, 477-496.
- (5) Tsakalakos, L. *Materials Science & Engineering R-Reports* **2008**, *62*, 175-189.
- (6) Li, J. H.; Zhang, J. Z. *Coordination Chemistry Reviews* **2009**, *253*, 3015-3041.
- (7) Mora-Sero, I.; Gimenez, S.; Fabregat-Santiago, F.; Gomez, R.; Shen, Q.; Toyoda, T.; Bisquert, J. *Accounts of Chemical Research* **2009**, *42*, 1848-1857.
- (8) Kamat, P. V. *Journal of Physical Chemistry C* **2008**, *112*, 18737-18753.
- (9) Hillhouse, H. W.; Beard, M. C. *Current Opinion in Colloid & Interface Science* **2009**, *14*, 245-259.
- (10) Guenes, S.; Sariciftci, N. S. *Inorganica Chimica Acta* **2008**, *361*, 581-588.
- (11) Feng, J. M.; Han, J. J.; Zhao, X. J. *Progress in Organic Coatings* **2009**, *64*, 268-273.
- (12) Liu, J. H.; Liu, J. Y.; Yang, L. B.; Chen, X.; Zhang, M. Y.; Meng, F. L.; Luo, T.; Li, M. Q. *Sensors* **2009**, *9*, 7343-7364.
- (13) Liu, S. Q.; Tang, Z. Y. *Journal of Materials Chemistry*, *20*, 24-35.
- (14) Yong, K. T.; Roy, I.; Swihart, M. T.; Prasad, P. N. *Journal of Materials Chemistry* **2009**, *19*, 4655-4672.

- (15) Gao, J. H.; Gu, H. W.; Xu, B. *Accounts of Chemical Research* **2009**, *42*, 1097-1107.
- (16) Martin-Palma, R. J.; Manso, M.; Torres-Costa, V. *Sensors* **2009**, *9*, 5149-5172.
- (17) Wu, Y. R.; Lin, Y. Y.; Huang, H. H.; Singh, J. *Journal of Applied Physics* **2009**, *105*, 7.
- (18) Nizamoglu, S.; Demir, H. V. *Applied Physics Letters* **2009**, *95*, 3.
- (19) Bowers, M. J.; McBride, J. R.; Rosenthal, S. J. *Journal of the American Chemical Society* **2005**, *127*, 15378-15379.
- (20) Lovingood, D. D.; Strouse, G. F. *Nano Letters* **2008**, *8*, 3394-3397.
- (21) Washington, A. L.; Strouse, G. F. *Chemistry of Materials* **2009**, *21*, 3586-3592.
- (22) Washington, A. L.; Strouse, G. F. *Chemistry of Materials* **2009**, *21*, 2770-2776.
- (23) Washington, A. L.; Strouse, G. F. *Journal of the American Chemical Society* **2008**, *130*, 8916-8922.
- (24) Gerbec, J. A.; Magana, D.; Washington, A.; Strouse, G. F. *Journal of the American Chemical Society* **2005**, *127*, 15791-15800.
- (25) Gedye, R. N.; Wei, J. B. *Canadian Journal of Chemistry-Revue Canadienne De Chimie* **1998**, *76*, 525-532.
- (26) Talapin, D. V.; Gaponik, N.; Borchert, H.; Rogach, A. L.; Haase, M.; Weller, H. *Journal of Physical Chemistry B* **2002**, *106*, 12659-12663.
- (27) Haubold, S.; Haase, M.; Kornowski, A.; Weller, H. *Chemphyschem* **2001**, *2*, 331-334.
- (28) Borchert, H.; Haubold, S.; Haase, M.; Weller, H. *Nano Letters* **2002**, *2*, 151-154.
- (29) Adam, S.; Talapin, D. V.; Borchert, H.; Lobo, A.; McGinley, C.; de Castro, A. R. B.; Haase, M.; Weller, H.; Moller, T. *Journal of Chemical Physics* **2005**, *123*, 10.
- (30) Chiappe, C.; Pieraccini, D. *Journal of Physical Organic Chemistry* **2005**, *18*, 275-297.

- (31) Qu, L. H.; Peng, X. G. *Journal of the American Chemical Society* **2002**, *124*, 2049-2055.
- (32) Peng, Z. A.; Peng, X. G. *Journal of the American Chemical Society* **2001**, *123*, 1389-1395.
- (33) Peng, Z. A.; Peng, X. G. *Journal of the American Chemical Society* **2001**, *123*, 183-184.
- (34) Peng, X. G.; Manna, L.; Yang, W. D.; Wickham, J.; Scher, E.; Kadavanich, A.; Alivisatos, A. P. *Nature* **2000**, *404*, 59-61.
- (35) Nair, P. S.; Scholes, G. D. *Journal of Materials Chemistry* **2006**, *16*, 467-473.
- (36) Trindade, T.; O'Brien, P.; Zhang, X. M. *Chemistry of Materials* **1997**, *9*, 523-530.
- (37) Cumberland, S. L.; Hanif, K. M.; Javier, A.; Khitrov, G. A.; Strouse, G. F.; Woessner, S. M.; Yun, C. S. *Chemistry of Materials* **2002**, *14*, 1576-1584.
- (38) Archer, P. I.; Santangelo, S. A.; Gamelin, D. R. *Journal of the American Chemical Society* **2007**, *129*, 9808-9818.
- (39) Archer, P. I.; Santangelo, S. A.; Gamelin, D. R. *Nano Letters* **2007**, *7*, 1037-1043.
- (40) Berrettini, M. G.; Braun, G.; Hu, J. G.; Strouse, G. F. *Journal of the American Chemical Society* **2004**, *126*, 7063-7070.
- (41) Wang, R.; Calvignanello, O.; Ratcliffe, C. I.; Wu, X.; Leek, D. M.; Zaman, M. B.; Kingston, D.; Ripmeester, J. A.; Yu, K. *Journal of Physical Chemistry C* **2009**, *113*, 3402-3408.
- (42) Tomaselli, M.; Yarger, J. L.; Bruchez, M.; Havlin, R. H.; deGraw, D.; Pines, A.; Alivisatos, A. P. *Journal of Chemical Physics* **1999**, *110*, 8861-8864.
- (43) Ratcliffe, C. I.; Yu, K.; Ripmeester, J. A.; Zaman, M. B.; Badarau, C.; Singh, S. *Physical Chemistry Chemical Physics* **2006**, *8*, 3510-3519.
- (44) Chan, W. C. W.; Nie, S. M. *Science* **1998**, *281*, 2016-2018.
- (45) Bruchez, M.; Moronne, M.; Gin, P.; Weiss, S.; Alivisatos, A. P. *Science* **1998**, *281*, 2013-2016.

- (46) Bharali, D. J.; Lucey, D. W.; Jayakumar, H.; Pudavar, H. E.; Prasad, P. N. *Journal of the American Chemical Society* **2005**, *127*, 11364-11371.
- (47) Jaiswal, J. K.; Mattoussi, H.; Mauro, J. M.; Simon, S. M. *Nature Biotechnology* **2003**, *21*, 47-51.
- (48) Huynh, W. U.; Dittmer, J. J.; Alivisatos, A. P. *Science* **2002**, *295*, 2425-2427.
- (49) Sun, B. Q.; Marx, E.; Greenham, N. C. *Nano Letters* **2003**, *3*, 961-963.
- (50) Gur, I.; Fromer, N. A.; Chen, C. P.; Kanaras, A. G.; Alivisatos, A. P. *Nano Letters* **2007**, *7*, 409-414.
- (51) Park, J.; Joo, J.; Kwon, S. G.; Jang, Y.; Hyeon, T. *Angewandte Chemie-International Edition* **2007**, *46*, 4630-4660.
- (52) van Embden, J.; Jasieniak, J.; Gomez, D. E.; Mulvaney, P.; Giersig, M. *Australian Journal of Chemistry* **2007**, *60*, 457-471.
- (53) Xie, R.; Battaglia, D.; Peng, X. *Journal of the American Chemical Society* **2007**, *129*, 15432-+.
- (54) Oda, K. *Industrial Health* **1997**, *35*, 61-68.
- (55) Zheng, W.; Winter, S. M.; Kattnig, M. J.; Carter, D. E.; Sines, I. G. *Journal of Toxicology and Environmental Health* **1994**, *43*, 483-494.
- (56) Kabe, I.; Kazuyuki, O.; Hiroshi, N.; Nomiya, T.; Uemura, T.; Hosoda, K.; Ishizuka, C.; Yamazaki, K.; Sakurai, H. *Journal of Occupational Health* **1996**, *38*, 6-12.
- (57) Yamazaki, I.; Tanaka, A.; Hirata, M.; Omura, M.; Makita, Y.; Inoue, N.; Sugio, K.; Sugimachi, K. *Journal of Occupational Health* **2000**, *42*, 169-178.
- (58) Micic, O. I.; Sprague, J.; Lu, Z. H.; Nozik, A. J. *Applied Physics Letters* **1996**, *68*, 3150-3152.
- (59) Antonietti, M.; Kuang, D. B.; Smarsly, B.; Yong, Z. *Angewandte Chemie-International Edition* **2004**, *43*, 4988-4992.
- (60) Kappe, C. O. *Angewandte Chemie-International Edition* **2004**, *43*, 6250-6284.
- (61) Redel, E.; Thomann, R.; Janiak, C. *Chemical Communications* **2008**, 1789-1791.

- (62) Laali, K. K.; Gettwert, V. J. *Journal of Fluorine Chemistry* **2001**, *107*, 31-34.
- (63) Koval'chuk, E. P.; Reshetnyak, O. V.; Kozlovs'ka, Z. Y.; Blazejowski, J.; Gladyshevs'kyj, R. Y.; Obushak, M. D. *Thermochimica Acta* **2006**, *444*, 1-5.
- (64) Heredia-Moya, J.; Kirk, K. L. *Journal of Fluorine Chemistry* **2007**, *128*, 674-678.
- (65) Fox, D. M.; Gilman, J. W.; De Long, H. C.; Trulove, P. C. *Journal of Chemical Thermodynamics* **2005**, *37*, 900-905.
- (66) Aki, S.; Brennecke, J. F.; Samanta, A. *Chemical Communications* **2001**, 413-414.
- (67) Lide, D. *CRC Handbook of Chemistry and Physics*; 88th Ed. ed., 2007-2008.
- (68) Pi, X. D.; Mangolini, L.; Campbell, S. A.; Kortshagen, U. *Physical Review B* **2007**, *75*, 5.
- (69) Murray, C. B.; Norris, D. J.; Bawendi, M. G. *Journal of the American Chemical Society* **1993**, *115*, 8706-8715.
- (70) Swafford, L. A.; Weigand, L. A.; Bowers, M. J.; McBride, J. R.; Rapaport, J. L.; Watt, T. L.; Dixit, S. K.; Feldman, L. C.; Rosenthal, S. J. *Journal of the American Chemical Society* **2006**, *128*, 12299-12306.
- (71) Ludolph, B.; Malik, M. A.; O'Brien, P.; Revaprasadu, N. *Chemical Communications* **1998**, 1849-1850.
- (72) Magana, D.; Wei, X.; Strouse, G. F. *Physical Review B* **2008**, *77*, 6.
- (73) Aslam, F.; Stevenson-Hill, J.; Binks, D. J.; Daniels, S.; Pickett, N. L.; O'Brien, P. *Chemical Physics* **2007**, *334*, 45-52.
- (74) Li, Y.; Feng, J. H.; Daniels, S.; Pickett, N. L.; O'Brien, P. *Journal of Nanoscience and Nanotechnology* **2007**, *7*, 2301-2308.
- (75) Magana, D.; Perera, S. C.; Harter, A. G.; Dalal, N. S.; Strouse, G. F. *Journal of the American Chemical Society* **2006**, *128*, 2931-2939.
- (76) Javier, A.; Meulenber, R. W.; Yun, C. S.; Strouse, G. F. *Journal of Physical Chemistry B* **2005**, *109*, 6999-7006.
- (77) Meulenber, R. W.; Jennings, T.; Strouse, G. F. *Physical Review B* **2004**, *70*, 5.

- (78) Meulenberg, R. W.; van Buuren, T.; Hanif, K. M.; Willey, T. M.; Strouse, G. F.; Terminello, L. J. *Nano Letters* **2004**, *4*, 2277-2285.
- (79) Javier, A.; Strouse, G. F. *Chemical Physics Letters* **2004**, *391*, 60-63.
- (80) Aslam, F.; Binks, D. J.; Rahn, M. D.; West, D. P.; O'Brien, P.; Pickett, N.; Daniels, S. *Journal of Chemical Physics* **2005**, *122*, 6.
- (81) Aslam, F.; Binks, D. J.; Rahn, M. D.; West, D. P.; O'Brien, P.; Pickett, N. *Journal of Modern Optics* **2005**, *52*, 945-953.
- (82) Aslam, F.; Binks, D. J.; Daniels, S.; Pickett, N.; O'Brien, P. *Chemical Physics* **2005**, *316*, 171-177.
- (83) Raola, O. E.; Strouse, G. F. *Nano Letters* **2002**, *2*, 1443-1447.
- (84) Hanif, K. M.; Meulenberg, R. W.; Strouse, G. F. *Journal of the American Chemical Society* **2002**, *124*, 11495-11502.
- (85) Meulenberg, R. W.; Strouse, G. F. *Physical Review B* **2002**, *66*, 6.
- (86) Meulenberg, R. W.; Bryan, S.; Yun, C. S.; Strouse, G. F. *Journal of Physical Chemistry B* **2002**, *106*, 7774-7780.
- (87) Farneth, W. E.; Herron, N.; Wang, Y. *Chemistry of Materials* **1992**, *4*, 916-922.
- (88) Dance, I. G.; Choy, A.; Scudder, M. L. *Journal of the American Chemical Society* **1984**, *106*, 6285-6295.
- (89) Choy, A.; Craig, D.; Dance, I.; Scudder, M. *Journal of the Chemical Society-Chemical Communications* **1982**, 1246-1247.
- (90) Wosten, W. J. *Journal of Applied Physics* **1962**, *33*, 246-&.
- (91) Javier, A.; Magana, D.; Jennings, T.; Strouse, G. F. *Applied Physics Letters* **2003**, *83*, 1423-1425.
- (92) Herron, N.; Wang, Y.; Eckert, H. *Journal of the American Chemical Society* **1990**, *112*, 1322-1326.
- (93) Nose, A.; Kudo, T. *Chemical & Pharmaceutical Bulletin* **1987**, *35*, 1770-1776.

- (94) Takagi, K. *Chemistry Letters* **1987**, 2221-2224.
- (95) Quarez, E.; Hsu, K. F.; Pcionek, R.; Frangis, N.; Polychroniadis, E. K.; Kanatzidis, M. G. *Journal of the American Chemical Society* **2005**, *127*, 9177-9190.
- (96) Peng, X. G.; Schlamp, M. C.; Kadavanich, A. V.; Alivisatos, A. P. *Journal of the American Chemical Society* **1997**, *119*, 7019-7029.
- (97) Katari, J. E. B.; Colvin, V. L.; Alivisatos, A. P. *Journal of Physical Chemistry* **1994**, *98*, 4109-4117.
- (98) Bae, W. K.; Char, K.; Hur, H.; Lee, S. *Chemistry of Materials* **2008**, *20*, 531-539.
- (99) Khitrov, G. A., University of California Santa Barbara, 2003.
- (100) Yu, W. W.; Qu, L. H.; Guo, W. Z.; Peng, X. G. *Chemistry of Materials* **2003**, *15*, 2854-2860.
- (101) Sachleben, J. R.; Wooten, E. W.; Emsley, L.; Pines, A.; Colvin, V. L.; Alivisatos, A. P. *Chemical Physics Letters* **1992**, *198*, 431-436.
- (102) Becerra, L. R.; Murray, C. B.; Griffin, R. G.; Bawendi, M. G. *Journal of Chemical Physics* **1994**, *100*, 3297-3300.
- (103) Jasieniak, J.; Mulvaney, P. *Journal of the American Chemical Society* **2007**, *129*, 2841-2848.
- (104) Sachleben, J.; Colvin, V.; Emsley, L.; Wooten, E. W.; Alivisatos, A. P. *Journal of Physical Chemistry B* **1998**, *102*, 10117-10128.
- (105) Puzder, A.; Williamson, A. J.; Gygi, F.; Galli, G. *Physical Review Letters* **2004**, *92*, 4.
- (106) Cherian, R.; Mahadevan, P. *Applied Physics Letters* **2008**, *92*, 3.
- (107) Bawendi, M. G.; Kortan, A. R.; Steigerwald, M. L.; Brus, L. E. *Journal of Chemical Physics* **1989**, *91*, 7282-7290.
- (108) Hamad, K. S.; Roth, R.; Rockenberger, J.; van Buuren, T.; Alivisatos, A. P. *Physical Review Letters* **1999**, *83*, 3474-3477.

- (109) Schreuder, M. A.; McBride, J. R.; Dukes, A. D.; Sammons, J. A.; Rosenthal, S. J. *Journal of Physical Chemistry C* **2009**, *113*, 8169-8176.
- (110) Kippeny, T. C.; Bowers, M. J.; Dukes, A. D.; McBride, J. R.; Orndorff, R. L.; Garrett, M. D.; Rosenthal, S. J. *Journal of Chemical Physics* **2008**, *128*, 7.
- (111) Neder, R. B.; Korsunskiy, V. I. *J. Phys.: Condens. Matter* **2005**, *17*, S125-S134.
- (112) Gilbert, B.; Huang, F.; Zhang, H. Z.; Waychunas, G. A.; Banfield, J. F. *Science* **2004**, *305*, 651-654.
- (113) Huxter, V. M.; Lee, A.; Lo, S. S.; Scholes, G. D. *Nano Letters* **2009**, *9*, 405-409.
- (114) Masadeh, A. S.; Bozin, E. S.; Farrow, C. L.; Paglia, G.; Juhas, P.; Billinge, S. J. L.; Karkamkar, A.; Kanatzidis, M. G. *Physical Review B* **2007**, *76*, 11.
- (115) Clark, S. M.; Prilliman, S. G.; Erdonmez, C. K.; Alivisatos, A. P. *Nanotechnology* **2005**, *16*, 2813-2818.
- (116) Gilbert, B.; Zhang, H.; Chen, B.; Kunz, M.; Huang, F.; Banfield, J. F. *Physical Review B* **2006**, *74*, 7.
- (117) Chen, B.; Penwell, D.; Benedetti, L. R.; Jeanloz, R.; Kruger, M. B. *Physical Review B* **2002**, *66*, 4.
- (118) Cerullo, G.; De Silvestri, S.; Banin, U. *Physical Review B* **1999**, *60*, 1928-1932.
- (119) Ithurria, S.; Guyot-Sionnest, P.; Mahler, B.; Dubertret, B. *Physical Review Letters* **2007**, *99*, 4.
- (120) Meulenberg, R. W.; Strouse, G. F. *Journal of Physical Chemistry B* **2001**, *105*, 7438-7445.
- (121) Murray, C. B.; Kagan, C. R.; Bawendi, M. G. *Science* **1995**, *270*, 1335-1338.
- (122) Colvin, V. L.; Schlamp, M. C.; Alivisatos, A. P. *Nature* **1994**, *370*, 354-357.
- (123) M. Kuno, J. K. L., B. O. Dabbousi, F. V. Mikulec, and M. G. Bawendi *Journal of Chemical Physics* **1997**, *106*, 9869-9882.
- (124) Liu, H.; Owen, J. S.; Alivisatos, A. P. *Journal of American Chemical Society* **2007**, *129*, 305-312.

- (125) Kopping, J. T.; Patten, T. E. *Journal of American Chemical Society* **2008**, *130*, 5689-5698.
- (126) Mikulec, F. V.; Kuno, M.; Bennati, M.; Hall, D. A.; Griffin, R. G.; Bawendi, M. G. *Journal of the American Chemical Society* **2000**, *122*, 2532-2540.
- (127) Thayer, A. M.; Steigerwald, M. L.; Duncan, T. M.; Douglass, D. C. *Physical Review Letters* **1988**, *60*, 2673-2676.
- (128) Watanabe, S.; Sasaki, S. *Japanese Journal of Applied Physics Part 2-Letters* **2003**, *42*, L1350-L1352.
- (129) V. Ladizhansky, G. H., and S. Vega *Journal of Physical Chemistry B* **1998**, *102*, 8505-8509.
- (130) Pines, A.; Gibby, M. G.; Waugh, J. S. *Journal of Chemical Physics* **1973**, *59*, 569-590.
- (131) Panich, A. M.; Sergeev, N. A.; Shlimak, I. *Physical Review B* **2007**, *76*, 8.
- (132) M. Gavish, S. V., and D. Zamir *Physical Review B* **1993**, *48*, 2191-2199.
- (133) Lo, A. Y. H.; Sudarsan, V.; Sivakumar, S.; van Veggel, F.; Schurko, R. W. *Journal of the American Chemical Society* **2007**, *129*, 4687-4700.
- (134) Ladd, T. D.; Maryenko, D.; Yamamoto, Y.; Abe, E.; Itoh, K. M. *Physical Review B* **2005**, *71*, 12.
- (135) Huang, Y. N.; Yan, Z. M. *Journal of the American Chemical Society* **2005**, *127*, 2731-2740.
- (136) Franzoni, M. B.; Levstein, P. R. *Physical Review B* **2008**, *78*, 5.
- (137) Franzoni, M. B.; Levstein, P. R. *Physical Review B* **2005**, *72*, 5.
- (138) Dementyev, A. E.; Li, D.; MacLean, K.; Barrett, S. E. *Physical Review B* **2003**, *68*, 4.
- (139) Cadars, S.; Smith, B. J.; Epping, J. D.; Acharya, S.; Belman, N.; Golan, Y.; Chmelka, B. F. *Phys Rev Lett* **2009**, *103*, 136802.
- (140) Hartmann, S. R.; Hahn, E. L. *Physical Review* **1962**, *128*, 2042-&.

- (141) R. Elbaum, S. V., G. Hodes *Chem. Mater.* **2001**, *13*, 2272-2280.
- (142) Tycko, R.; Barrett, S. E.; Dabbagh, G.; Pfeiffer, L. N.; West, K. W. *Science* **1995**, *268*, 1460-1463.
- (143) Goehring, L.; Michal, C. A. *Journal of Chemical Physics* **2003**, *119*, 10325-10329.
- (144) Lovingood, D. D.; Oyler, R. E.; Strouse, G. F. *Journal of the American Chemical Society* **2008**, *130*, 17004-17011.
- (145) Li, D.; Dong, Y. Q.; Ramos, R. G.; Murray, J. D.; MacLean, K.; Dementyev, A. E.; Barrett, S. E. *Physical Review B* **2008**, *77*, 26.
- (146) Duke, C. B. *Chemical Reviews* **1996**, *96*, 1237-1259.
- (147) Kolodziejcki, W.; Klinowski, J. *Chemical Reviews* **2002**, *102*, 613-628.
- (148) Ando, S.; Harris, R. K.; Reinsberg, S. A. *Journal of Magnetic Resonance* **1999**, *141*, 91-103.
- (149) Ando, S.; Harris, R. K.; Holstein, P.; Reinsberg, S. A.; Yamauchi, K. *Polymer* **2001**, *42*, 8137-8151.
- (150) Ando, S.; Harris, R. K.; Reinsberg, S. A. *Magnetic Resonance in Chemistry* **2002**, *40*, 97-106.
- (151) Klur, I.; Jacquinet, J. F.; Brunet, F.; Charpentier, T.; Virlet, J.; Schneider, C.; Tekely, P. *Journal of Physical Chemistry B* **2000**, *104*, 10162-10167.
- (152) Crank, J. *The Mathematics of Diffusion*; 2nd ed.; Oxford Science Publications, 1975.
- (153) Li, D.; Dementyev, A. E.; Dong, Y.; Ramos, R. G.; Barrett, S. E. *Phys Rev Lett* **2007**, *98*, 190401.
- (154) Carr, H. Y.; Purcell, E. M. *Physical Review* **1954**, *94*, 630-638.
- (155) Meiboom, S.; Gill, D. *Review of Scientific Instruments* **1958**, *29*, 688-691.
- (156) Ramsey, N. F. *Physical Review* **1950**, *78*, 699-703.

(157) Brus, L. E. *Journal of Chemical Physics* **1984**, *80*, 4403-4409.

(158) Lee, J. R. I.; Meulenberg, R. W.; Hanif, K. M.; Mattoussi, H.; Klepeis, J. E.; Terminello, L. J.; van Buuren, T. *Physical Review Letters* **2007**, *98*, 4.

(159) Duddeck, H. *Prog. Nucl. Magn. Reson. Spectrosc.* **1995**, *27*, 1-323.

BIOGRAPHICAL SKETCH

CURRICULUM VITAE

EDUCATION

Florida State University, Tallahassee, Florida, Ph. D. in Chemistry, Spring 2010.

Dissertation Title: *Synthesis and analysis of the quantum dot core and surface structures probed by solid state nuclear magnetic resonance*

Valdosta State University, Valdosta, Georgia, B.S. in Chemistry, August 2002.

EMPLOYMENT

Valdosta State University, Valdosta, Georgia

Instructor, August 2009 – May 2010

Courses Taught:

- 1151K, Survey of Chemistry I
- 1152K, Survey of Chemistry II
- 1151KL, Survey of Chemistry I Laboratory
- 1152KL, Survey of Chemistry II Laboratory
- 1211L, Principles of Chemistry I Laboratory
- 1212L, Principles of Chemistry II Laboratory

Duties include:

- Writing quizzes and test
- Grading quizzes, tests and lab reports
- Encouraging and holding office hours for one-on-one student consultations
- Providing lab lecture
- Demonstrating proper lab techniques and safety

AWARDS

Hoffman Merit Award

- \$3,000 award to first year Teaching Assistants for previous academic achievements

MARTECH Research Fellowship, Florida State University (2008 - present)

- \$35,000 Fellowship as a Research Assistant for leading-edge research in materials science and associated technologies

Exxon Mobil Research and Engineering Company/National High Magnetic Field Laboratory Travel Award

- \$300 travel award to represent FSU's Chemistry and Biochemistry department at the Rocky Mountain Conference for NMR in Colorado

EXPERIENCE

Teaching Assistant - Florida State University, 2004 - 2008

Courses Taught:

- General Chemistry I, CHM 1045 (majors)
- General Chemistry II, CHM 1046 (majors)
- Organic Chemistry Lab, CHM 2211 (majors)
- General Chemistry Lab, CHM 1020 (non majors)

Duties included:

- Guest lecturing for General and Analytical Chemistry courses
- Preparing lectures and quizzes
- Grading tests, quizzes and lab reports
- Encouraging and holding office hours for one-on-one student consultations
- Providing lab lecture
- Demonstrating proper lab techniques and safety

Research Assistant - Florida State University, Strouse Group 2004 - present

Research included:

- Microwave synthesis of InP nanomaterials with in-situ ion etching from ionic liquids decomposition. These materials generated the highest reported quantum efficiency for these materials.
- The use of Solid State NMR to selectively probe site occupancy to observe size dependent reconstruction in CdSe quantum dots.
- Other analytical techniques used include: UV-Vis, FT-IR, Photoluminescence, powder X-ray Diffractometry, X-ray Fluorescence.

Undergraduate Research -Valdosta State University, July 2000 - August 2002

Advisor: Prof. Thomas J. Manning

Research involved the scanning of humic acid from soil samples for natural products, herbicides and pesticides. Samples were taken along the Suwannee River from Fargo, Georgia to the Gulf of Mexico. Characterization of humic acid samples was accomplished by using the following instruments:

- Carbon, Hydrogen, Nitrogen, and Sulfur Detector
- Inductively Coupled Plasma - Atomic Emission Spectrometer
- High Performance Liquid Chromatograph
- MALDI-MS

GRADUATE PUBLICATIONS

Microwave Induced In-Situ Active Ion Etching of Growing InP Nanocrystals. D. D. Lovingood, G.F. Strouse. *Nano Letters*, 8, 3394-3397, 2008.

Composition Control and Localization of S²⁻ in CdSSe Quantum Dots Grown from Li₄[Cd₁₀Se₄(SPh)₁₆]. D. D. Lovingood, R. E. Oyler, G. F. Strouse. *Journal of the American Chemical Society*, 130, 17004-17011, 2008.

Size and Site Dependent Reconstruction in CdSe QDs Evidenced by $^{77}\text{Se}\{^1\text{H}\}$ CP-MAS NMR. D. D. Lovingood, R. Achey, A. K. Paravastu, G. F. Strouse. *Journal of the American Chemical Society*, Accepted 2010.

Bimodal Intracellular Nanoparticles Based on Quantum Dot Technology for High Field MR Microscopy at 21.1 T. J.T. Rosenberg, J.M. Kogot, D.D. Lovingood, G.F. Strouse, and S.C. Grant. *Magnetic Resonance in Medicine*, Accepted 2010.

Analysis of structural differences in Cd^{77}Se with cubic, wurtzite and stacking faults via Solid State Nuclear Magnetic Resonance. D. D. Lovingood, R. Achey, G. F. Strouse (Manuscript in preparation)

PATENTS

Ion Etching of Growing InP Nanocrystals Using Microwaves. D. D. Lovingood, G.F. Strouse. *Patent 12/201,589 Pending*. 2008.

UNDERGRADUATE PUBLICATIONS

Infrared studies of Suwannee River humic substances: evidence of chlorination of humics in salt water. T. J. Manning, S. Strickland, A. Feldman, T. Umberger, D. D. Lovingood, M. Coulibay, J. Elder, L. Noble, *Florida Scientist*, 66(4), 253-266, 2003.

Naturally occurring organic matter as a chemical trap to scan an ecosystem for natural products. T. J. Manning, T. Umberger, S. Strickland, D. D. Lovingood, R. Borchelt, M. Land, D. Phillips, J. C. Manning, *International Journal of Environmental Analytical Chemistry*, 83(10), 861-866, 2003.

Miller-Urey revisited: when lightning strikes the Earth. W. Paneral, B. Leslie, D. D. Lovingood, R. Stapleton, M. Anderson, A. McRae, L. Atwater, Leri; T. J. Manning, D. Phillips. *Chemical Educator*, 7(3), 149-154, 2002.

Nanostructures in physical materials chemistry: an exploratory laboratory. T. J. Manning, A. Feldman, M. Anderson, L. Atwater, B. Lesile, D. D. Lovingood, A. McRae, R. Stapleton, K. Riddle, J. Lui, T. Vickers, N. Dalal, L. Van de Burg, *Chemical Educator*, 6(4), 238-246 2001.

PRESENTATIONS

D.D. Lovingood. Chemistry, Nanomaterials, & Research. Valdosta State University, September 2009.

D. D. Lovingood, G.F. Strouse. In Situ Active Ion Etching of Growing Indium Phosphide Nanocrystals: Microwave Induced Thermal Decomposition of Ionic Liquids. ACS 236th National Meeting. Philadelphia, Pennsylvania, August 2008

D. D. Lovingood, R. Achey, G.F. Strouse. Inspection of Nanocrystalline Cadmium Selenide by Solid State NMR: Probing Reconstruction Driven by Surface Ligation. 50th Rocky Mountain Conference on Analytical Chemistry. Breckenridge, Colorado, July 2008.

D. D. Lovingood, G.F. Strouse. Microwave Synthesis of III-V Nanomaterial. Florida Annual Meeting and Exposition. Orlando, Florida, May 2006.